Microscopic Properties of the Fractional Quantum Hall Effect

Professor Bertrand I. Halperin **Angela Kou**
Professor Charles M. Marcus

Microscopic Properties of the Fractional Quantum Hall Effect

Abstract

The fractional quantum Hall effect occurs when an extremely clean 2-dimensional fermion gas is subject to a magnetic field. This simple set of circumstances creates phenomena, such as edge reconstruction and fractional statistics, that remain subjects of experimental study 30 years after the discovery of the fractional quantum Hall effect. This thesis investigates the properties of excitations of the fractional quantum Hall effect.

The first set of experiments studies the interaction between fractional quantum Hall quasiparticles and nuclei in a quantum point contact (QPC). Following the application of a DC bias, fractional plateaus in the QPC shift symmetrically about half filling of the lowest Landau level, $\nu = 1/3$, suggesting an interpretation in terms of composite fermions. Mapping the effects from the integer to fractional regimes extends the composite fermion picture to include hyperfine coupling.

The second set of experiments studies the tunneling of quasiparticles through an antidot in the integer and fractional quantum Hall effect. In the integer regime, we conclude that oscillations are of the Coulomb type from the scaling of magnetic field period with the number of edges bound to the antidot. Generalizing this picture to the fractional regime, we find (based on magnetic field and gate-voltage periods) at $\nu = 2/3$ a tunneling charge of (2/3)e and a single charged edge. Further unpublished data related to this experiment as well as alternative theoretical explanations are also

presented.

The third set of experiments investigates the properties of the fractional quantum Hall effect in the lowest Landau level of bilayer graphene using a scanning single-electron transistor. We observe a sequence of states which breaks particle-hole symmetry and instead obeys a $\nu \rightarrow \nu + 2$ symmetry. This asymmetry highlights the importance of the orbital degeneracy for many-body states in bilayer graphene.

The fourth set of experiments investigates the coupling between microwaves and the fractional quantum Hall effect. Reflectometry is used to investigate bulk properties of samples with different electron densities. We observe large changes in the amplitude of the reflected signal at each integer filling factor as well as changes in the capacitance of the system.

Contents

List of Figures

List of Tables

Acknowledgments

I had the chance to work with some of the most amazing people on the planet and this section can only go a small way toward expressing my gratitude for their support during my PhD. Also, since I got to work with 5/2 as many people as a standard PhD student does, this section will be at least 5/2 as long as a standard acknowledgements section is.

First, I would like to thank my advisor Charlie Marcus for all of the training and support he has provided me with over the past few years. Charlie's insistence that every member of the lab understand every aspect of their experiment from the Ithaco knobs to the dilution refrigerators to the effects of nuclei on fractional quasiparticles has meant that I have learned more than I thought possible during the course of my PhD. Charlie has also taught me the art of giving a good physics presentation. He turned a shy, quiet, prone to mumbling first-year into a lean, mean, physics-presenting machine. Just kidding, but I speak much louder and make much clearer slides now. Charlie created an excellent environment for experimenting in his lab. In addition to keeping the lab extremely organized and providing us with any and all of the equipment necessary to performing our experiments, he maintained a level of excitement about experiments that I did not think was sustainable at all hours of the day. This may explain why Marcus lab members could be found in lab at basically any time of day.

Next, I would like to thank Amir Yacoby for the guidance he has given me during my PhD. Amir's emphasis on understanding the basics of physics as well as the complicated concepts has made me a deeper thinker and led me to a much better understanding of different aspects of condensed matter systems. Amir also very gen-

erously welcomed me into his lab to work on the scanning SET setup despite the fact that I had no previous experience with scanning setups and was a fifth-year. It has been a joy to work with Amir in an experimental setting; his creativity and deep understanding of all things physics-related were evident in every conversation. I have hugely benefited from and enjoyed our discussions about everything from device fabrication to gapless modes to science education.

I would like to thank Bert Halperin for illuminating many theoretical aspects of my experiments and for serving as my advisor for the last year of my PhD (I think I am Bert's only experimental PhD student). Bert was always able to point out an aspect of our experiments that led to an important insight into the physics behind the phenomena that we were observing. I also thank Bert for patiently answering the questions of an impatient experimentalist.

I would like to thank all of the Marcus lab members who were with me through late nights, early mornings, late nights into early mornings, and everything in between. Doug McClure was one of the best senior graduate mentors a first year graduate student could hope for. He taught me all aspects of fabrication, dilution refrigeration, and physics experimentation. Doug always lent a helping hand even when we were no longer working on the same experiment or even in the same institution. Patrick Gallagher was one of the best first-year graduate students a senior graduate student could hope for. Patrick's hard work greatly increased the speed at which electrons got cold in our new cryogen-free fridge and his sense of humor greatly decreased the tedium of waiting 30 hours to check if our latest scheme had helped the electron temperature at all.

Willy Chang provided me with many entertaining moments in lab including but not limited to a "pimp my fridge" area for fridge repairs, Top Gear videos, and boxing matches in the hall. Andrew Higginbotham could always be counted on for an interesting physics discussion or a "go on girl, do ya thang" when I needed some encouragement. Hugh Churchill taught me everything I know about reflectometry measurements and charge sensing as well as served as a calming presence during the final packing of the Marcus lab at Harvard. Jim Medford was extremely helpful whenever I needed a helping hand with a part of my fridge dewar or wanted to understand random aspects of spin qubits. Even on no sleep and little food, Patrick Herring taught me a great deal about sample fabrication and metallurgy. Maja Cassidy hosted many fun gatherings for lab orphans and made sure that the lab was always in ship shape. Morten Kjaergaard gave the Marcus lab its first Majorana fermion and also introduced me to the concept of beer croquet. Christian Barthel and Jimmy Williams provided the necessary jokes to truly welcome me into the Marcus Lab.

I learned many interesting facts about bees, helium leak detectors, solex bicycles, and carbon nanotubes from Ferdinand Kuemmeth. I also really appreciated the many offbeat physics questions that Ferdinand would ask to test my understanding of pressure, capacitance, and special relativity. Vlad Manucharyan taught me everything I know about superconductors, including the most important one: superconductors HATE magnetic fields. I also thank Vlad for encouraging me to join the Devoret lab at Yale for my postdoc. Javad Shabani was always available to share some of his extensive knowledge of GaAs 2DEGs. I am also really grateful to have been able to work with Yiming Zhang, Teesa Christian, Brandon Armstrong, Johannes Beil, Peter

Nissen, Susan Watson, Edward Laird, Yongjie Hu, Ruby Lai, Menyoung Lee, Alex Hristov, Anna Schneidman, Merritt Moore, Paden Roder, Mattias Fitzpatrick, and Jason Wien.

I would also like to thank the members of Yacoby Lab for welcoming me into the lab this past year. Ben Feldman is one of the most patient and careful experimentalists I have ever met. I thank Ben for explaining scanning single-electron transistors as well as serving as a great discussion partner when we were trying to understand our experiment. Andrei Levin was very creative in finding solutions to problems we encountered and could always be counted on to code something in Matlab to make experimenting a little easier. DiDi Wei worked extremely hard to learn all aspects of graphene and also provided entertaining stories about chickens, rabbits, and fire corals. Mikey Shulman had an extensive knowledge of all things computer- and snack-related and graciously allowed us to use his new fridge to test our samples. Sean Hart used his superior height to our benefit during testing of microscope lines and asked very thoughtful physics questions. Vivek Venkatchalam provided insights into cooling electrons, compressibility in the fractional quantum Hall effect, and the secret lives of worms. I also thank Shannon Harvey, Marc Warner, Hechen Ren, Michael Grinolds, Suzanne Muller, Kristiaan De Greve, Lan Luan, Monica Allen, Gilad Ben-Shach, and Lucas Thiel for making the Yacoby lab a great place to be.

I would like to thank Pablo Jarillo-Herrero for allowing me to use the transfer setup in his lab. Javier Sanchez-Yamagishi taught me all aspects of the transfer process from substrate to contacts. I thank Ben Hunt, Hadar Steinberg, Valla Fatemi, Joel Wang, Britt Baugher, Qiong Ma, Andrea Young, and Jason Luo for letting me into

the lab.

I thank Loren Pfeiffer for providing us with extremely high quality GaAs wafers and even tailoring wafers for our specific experiments. I also thank Loren for explaining to me different aspects of GaAs growth during my first year of graduate school. I thank Ken West and Kirk Baldwin for showing me around the MBE lab during my visit to Princeton. I am also grateful to Michael Manfra for providing us with GaAs wafers and working with us to create new structures. I thank Station Q for providing the funding to keep my experiment going and assembling a conference with great theorists and experimentalists every six months.

I thank Ady Stern for providing many insights into antidots and for introducing me to the best cafe in Tel Aviv. I also thank Bernd Rosenow and Izhar Neder for illuminating many aspects of the fractional quantum Hall effect. I thank Dima Abanin for teaching me about various theoretical aspects of graphene as well as for introducing me to Bulgakov and Lyubov.

I would not have been able to make any devices without the Harvard cleanroom. I thank JD Deng, Yuan Lu, Jason Tresback, Mac Hathaway, Ed Macomber, Ling Xie, John Tsakirgis, and Steve Paolini for their help in solving cleanroom problems and providing training for each instrument. I thank Nick Dent from Oxford Instruments for saving my fridge (and my experiment) on quite a few occasions. I thank Gustav Teleberg and Chris Wilkinson at Oxford for being very responsive during my first few months of operating the fridge and for providing me with every single technical drawing I asked them for within a few hours of asking. I thank Louis Defeo and the guys at the machine shop for making everything I needed for a working experiment

and always doing it in a rush. I also thank Jess Martin, Rita Filipowicz, and Carolyn Moore for keeping the labs up and running.

I have also had a great deal of support outside of lab. I thank the members of **crayjee* who have known me since high school and encouraged me in everything that I do; I especially thank Jooyoung Yeu for making sure that I had delicious dinners multiple times a month. I thank Mark Morales for his encouragement during my first few years of graduate school. I thank Mitchell Oh for providing me with a place to stay in Cambridge at the end of my PhD and introducing me to all kinds of excellent pop culture. I thank Stacey Shi, Kardelen Pekcan, Carlene Liriano, Beatriz Herrera, and Grace Yang for infinite hours of entertaining conversation.

Finally, I would like to thank my family for all of the love and support they have given me throughout the years. I thank my little sister, Anne, for being able to explain details about my research despite never having taken a physics class in college. I thank my mom for encouraging me in my work despite its consequences on my wardrobe and my sleep schedule. I thank my dad for figuring out early on that I should do physics but having the wisdom to let me find my path to physics on my own.

Chapter 1

Introduction

Electron-electron interactions often produce interesting phenomena. In high-temperature superconductors, for example, electrons in a normally insulating material at room temperature interact to produce a material that transmits current without dissipation at low temperatures. In heavy fermion solids, electrons residing in the f-orbital of atoms interact with free conduction electrons to make particles with large effective masses. But, in my opinion, the most interesting phenomena produced by electron interactions are fractionally charged quasiparticles. At high magnetic fields and in clean samples, electrons conspire with each other and the magnetic field to minimize the Coulomb repulsion between themselves. In doing so, they produce what is known as the fractional quantum Hall effect.

This thesis will present several experiments that I have performed during my PhD at Harvard, which explore properties of the fractional quantum Hall effect in two material systems using various tools. For the rest of this introductory chapter, I will give some background information about 2-dimensional systems and how to imple-

ment them. I will then detail the physics of the integer and fractional quantum Hall effects. The background necessary to understand each of the individual experiments is presented in the introduction of each chapter. Chapter 2 details an investigation of dynamic nuclear polarization and its effects on the integer and fractional quantum Hall effects in GaAs. We find that the nuclei and composite fermions interact with each other and that the effects of the polarized nuclei can be observed in transport. In Chapter 3, we investigate the edge structure and quasiparticle charge of $\nu = 2/3$ using resistance oscillations through an antidot fabricated on GaAs. The epilogue of Chapter 3 details antidot experiments performed at other fractional filling factors and introduces an alternative interpretation of our data. Chapter 4 details the discovery of an interesting sequence of fractional quantum Hall states found in bilayer graphene using a single-electron transistor. Chapter 5 presents an unfinished experiment using RF reflectometry to study the fractional quantum Hall effect.

Appendix A presents lessons learned while wiring a dilution refrigerator and the ingredients necessary to achieve electron temperatures less than 20 mK. I also present considerations for designing sampleholders for both traditional and cryogen-free refrigerators. Appendix B details the fabrication procedures for devices made on GaAs. Appendix C details the fabrication procedures for making graphene on hexagonal-boron nitride on graphite samples including some tricks specific to fabrication in the Harvard University cleanroom. And now, onto the physics!

1.1 Why should we work in two dimensions?

Working in two dimensions is interesting for a few reasons. Losing the third dimension makes it feasible for us to change the density of the sample using a top gate. In particular, this is very useful because one can then imagine creating structures such as quantum dots and quantum point contacts by completely depleting the area under a top gate. Working in two dimensions also allows for the possibility of particles with exchange statistics different from bosonic or fermionic statistics. Finally, working in two dimensions allows us to see the quantum Hall effect, in which the quantized Hall conductance is equal to the Hall conductivity, regardless of the dimension of the sample. The fractional quantum Hall effect and all of its associated phenomena are also only possible in 2-dimensions, and its study will form the bulk of this thesis.

1.2 How do we create 2-dimensional systems?

1.2.1 GaAs Quantum Wells

One way to create a 2-dimensional system is to create a potential well by layering semiconductors. Since different semiconductors have different gaps, one can put different semiconductors next to each other to create potential wells. The most commonly used semiconductors to build high quality 2-dimensional systems are gallium arsenide (GaAs) and aluminum gallium arsenide (AlGaAs). These two materials are chosen because GaAs and AlGaAs have very similar lattice constants, which results in very little strain between the layers. Gallium arsenide/aluminum gallium arsenide quantum well structures are grown using molecular beam epitaxy under ultrahigh vac-

uum. A quantum well is a potential well whose width is small enough such that the allowed energies inside the well are quantized. A typical material starts with a GaAs substrate on which a superlattice consisting of alternating layers of AlGaAs/GaAs is grown. The purpose of a superlattice is to trap any defects within the many wells created by repeatedly sandwiching GaAs inside AlGaAs. The wells keep the defects from migrating upward and becoming scattering sites for the electrons in the 2-dimensional electron gas [3]. A spacer layer of AlGaAs is next grown. Then Silicon (Si) donors are introduced into the system via δ-doping. The thickness of the doping region will be only about a few angstroms, which is much smaller than any other scale in the structure so the distribution can be represented by a δ function, hence the name δ-doping. The donors can either be doped straight into the AlGaAs or into mini quantum wells made from aluminum arsenide (AlAs)/GaAs/AlAs sandwiches.

Each of these schemes has its advantages and disadvantages. Doping straight into AlGaAs results in the creation of DX centers. DX centers are formed when the crystal lattice deforms around the Si donor atom, which causes the electron to be tightly bound rather than free to fall into the 2DEG [3]. This results in lower electron densities (which could be what one wants) and mobilities (which is usually not what one wants). But, because the DX centers have basically frozen into place by about 150 Kelvin, these materials are often easily controlled by gates at dilution refrigerator temperatures. Doping into mini quantum wells results in the donors being bound with energies determined by the depth of the well, which are usually much less than 150 K. This results in high densities and mobilities (up to 37.8 million $cm^2/V{\cdot}s$ [4]!) but sometimes results in 2DEGs which cannot be well controlled by

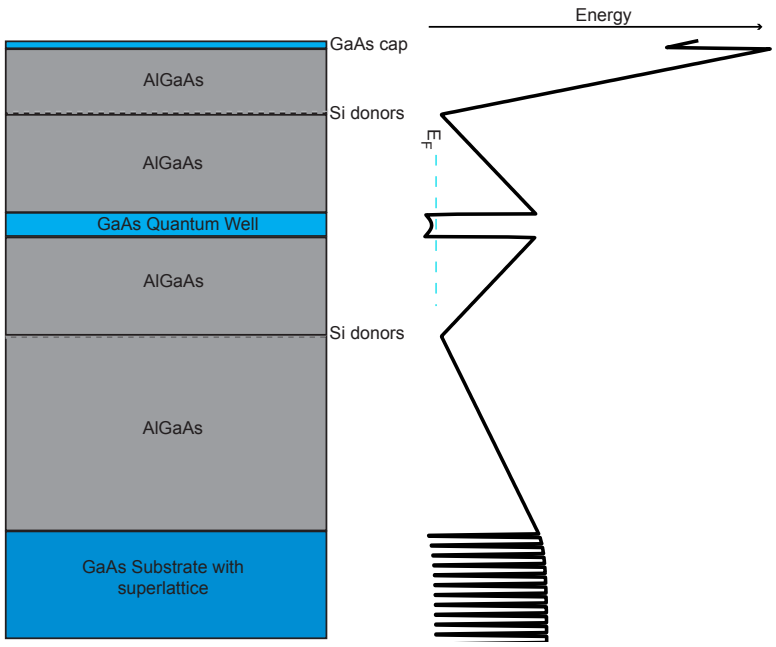

Figure 1.1: AlGaAs/GaAs Quantum Well Structure with Corresponding Energy Structure. Blue dashed line shows the Fermi energy in the system. Band structure was calculated using the AQUILA package for MATLAB.

gates because the donors are less tightly bound and can move around even at dilution refrigerator temperatures, resulting in drifts of the gate potential seen by the 2DEG over time.

The main quantum well where the 2DEG will be formed is next grown using an AlGaAs/GaAs/AlGaAs sandwich. Then another layer of dopants is introduced in order to compensate for surface states, which can form from oxidation in the GaAs cap layer or can develop during the fabrication process. Finally a GaAs cap layer is grown on top. A typical quantum well structure with corresponding energy diagram is shown in Fig. 1.1.

We can easily see from the potential shown in Fig. 1.1 how a 2DEG is generated in this structure. A quantum well is formed at both GaAs/AlGaAs interfaces because

of the difference in band gaps between GaAs and AlGaAs. As electrons fall into the well, an electric field builds up between the positive donor atoms outside of the well and the electrons inside the well, which causes bending of the bands at the interface between the GaAs and AlGaAs [5]. This quantum well only allows certain discrete energies. If the density of electrons in the well is low enough that the Fermi energy is in between the ground state and the first excited state, then the electrons cannot move in Z, but only in X and Y. And so we have our 2-dimensional electron gas.[1]

1.2.2 Graphene

Another way to create a 2-dimensional system is by isolating a single layer of atoms. In graphene, fairly simply processes allow us to create 2-dimensional fermion gases. The most commonly used way to create graphene is exfoliation using tape. One first sticks a piece of tape onto a bulk piece of graphite and removes a film of graphite just by peeling the tape off. This piece of tape is then stuck onto a clean SiO_2 substrate and peeled off. Several pieces of single-layer graphene, which are a few microns in size, will be found. This will result in graphene with mobilities of 15,000 $cm^2/V{\cdot}s$ [7]. Various refinements can be made to improve its quality such as suspending the graphene or putting it on a cleaner substrate. The charge carriers of graphene are actually Dirac fermions, which can be derived from a tight-binding calculation

[1]Quantum wells often have a nonzero size of about 20 to 30 nm, which can result in the electron wavefunction having a finite thickness. This finite thickness can result in changes in the behavior of fractional quantum Hall states [6].

Dirac Fermions

The lattice of monolayer graphene can be parametrized by considering an A and B sub-lattice with lattice vectors:

$$\mathbf{x_1} = \frac{a}{2}(3, \sqrt{3}),\ \mathbf{x_2} = \frac{a}{2}(3, -\sqrt{3}) \tag{1.1}$$

where a is the lattice constant of graphene [8]. The nearest neighbor vectors are:

$$\delta_\mathbf{1} = \frac{a}{2}(1, \sqrt{3}),\ \delta_\mathbf{2} = \frac{a}{2}(1, -\sqrt{3}), \delta_\mathbf{3} = (-a, 0) \tag{1.2}$$

The graphene lattice and the vectors mentioned above are shown in Fig. 1.2(a). The reciprocal lattice is also a hexagonal lattice but with lattice vectors rotated from $\mathbf{x_1}$ and $\mathbf{x_2}$ by 90 degrees. We can use the tight-binding model to find the band structure of graphene:

$$H = -t \sum_{<ij>} (a_i^\dagger b_j + h.c.), \tag{1.3}$$

where the sum is over nearest neighbors and t is the hopping energy between nearest neighbors $< ij >$. Working in $\mathbf{k}$-space, we get the Hamiltonian:

$$H_\mathbf{k} = \begin{pmatrix} 0 & \Delta_\mathbf{k} \\ \Delta_\mathbf{k}^* & 0 \end{pmatrix}, \Delta_k \equiv -t \sum_{i=0}^{3} e^{-i\mathbf{k}\cdot\delta_\mathbf{i}}$$

We diagonalize this Hamiltonian to find:

$$E_\mathbf{k} = \pm t \sqrt{3 + 2cos(\sqrt{3}k_y a) + 4cos(\frac{\sqrt{3}}{2}k_y a)cos(\frac{3}{2}k_x a)}, \tag{1.4}$$

where k_y is the y-component of the wavevector, and k_x is the x-component of the wavevector. We note that the energy is zero at two different points:

$$\mathbf{K} = (\frac{2\pi}{3a}, \frac{2\pi}{3\sqrt{3}a}), \mathbf{K'} = (\frac{2\pi}{3a}, -\frac{2\pi}{3\sqrt{3}a}). \tag{1.5}$$

These are known as the valleys of graphene. If we expand around these points, we find that $E \approx \pm v_F \mid \mathbf{q} \mid$, where v_F is the Fermi velocity and $\mathbf{q} \equiv \mathbf{K} - \mathbf{k}$. The electrons behave as massless fermions!

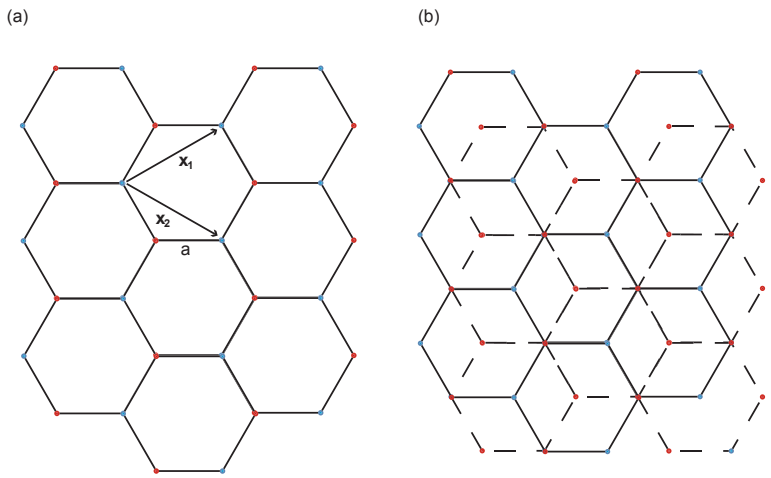

Figure 1.2: (a) Lattice of monolayer graphene. A (B) atoms are indicated in red (blue). Lattice vectors $\mathbf{x_1}$ and $\mathbf{x_2}$ are shown. Lattice constant is a=2.46 $\mathring{A}$. (b) Bernal stacking of bilayer graphene. The top (bottom) layer is represented with solid (dashed) lines.

For bilayer graphene, the Hamiltonian gets a bit more complicated since we have to include 4 sites in the unit cell along with their various couplings to each other. We will consider Bernal stacking, where an A atom in the top layer is above a B atom in the bottom layer, as shown in Fig. 1.2(b). We will keep the intralayer hopping terms that we had in the monolayer case and add an interlayer hopping between an A atom on the top layer and a B atom on the bottom layer. Expanding around **K** or

K' gives us :

$$H_{\mathbf{q}} = \begin{pmatrix} 0 & v_F(q_x + iq_y) & 0 & 0 \\ v_F(q_x - iq_y) & 0 & \gamma_1 & 0 \\ 0 & \gamma_1 & 0 & v_F(q_x + iq_y) \\ 0 & 0 & v_F(q_x - iq_y) & 0 \end{pmatrix},$$

where q_x and q_y are the x- and y- components of the q-vector defined above, and γ_1 is the interlayer hopping energy. Near the Dirac point, this Hamiltonian gives us four energies: $E = -\gamma_1, 0, 0, \gamma_1$, where we assume γ_1 is much bigger than $v_F \mid q \mid$ since we are close to the Dirac point. We know, then, that the $-\gamma_1$ subband is filled and the γ_1 subband is not filled but we need to work out the Hamiltonian in the subspace of the A atom on the bottom layer and the B atom on the top layer to find the shape of the low-energy bands near the Dirac point. The effective Hamiltonian in this new subspace is [9]:

$$H_{\mathbf{q}} = \frac{v_F^2}{\gamma_1} \begin{pmatrix} 0 & (q_x + iq_y)^2 \\ (q_x - iq_y)^2 & 0 \end{pmatrix}$$

The charge carriers of bilayer graphene are massive Dirac fermions with mass $m = \gamma_1/v_F^2$.

1.3 Quantum Hall Effects

1.3.1 Hall Effect

Let's first understand the Hall effect, which occurs in 3-dimensions. If we apply a current to a slab of metal in the x-direction in a constant magnetic field B in the z-direction, what do we expect to measure for the resistance in the y-direction (see Fig.

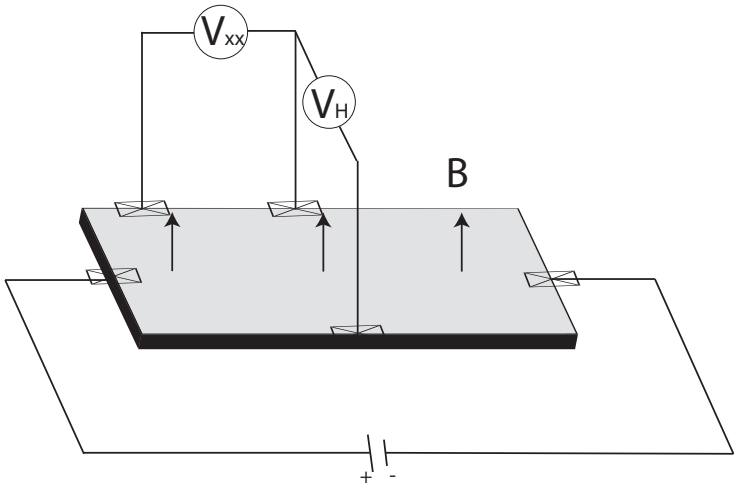

Figure 1.3: A typical transport measurement where the Hall voltage, V_H, and longitudinal voltage, V_{xx}, of a sample in a perpendicular magnetic field are measured.

1.3(a))? Well, in steady state, there can't be any current flowing in the y-direction so the electric field in y-direction (E_y) must exactly cancel the Lorentz force felt by the charge carriers in B. This condition gives us the simple equation:

$$\rho_{xy} = \frac{E_y}{j_x} = \frac{B}{ne}, \tag{1.6}$$

where j_x is the current density in the x-direction, n is the density, and e is the charge. In three dimensions, the Hall resistance[2], R_H is equal to $\frac{B}{new}$, where w is the width of the slab. In two dimensions, R_H is equal to ρ_{xy}. This is known as the Hall effect and is often used to find the density and sign of charge carriers in a system.

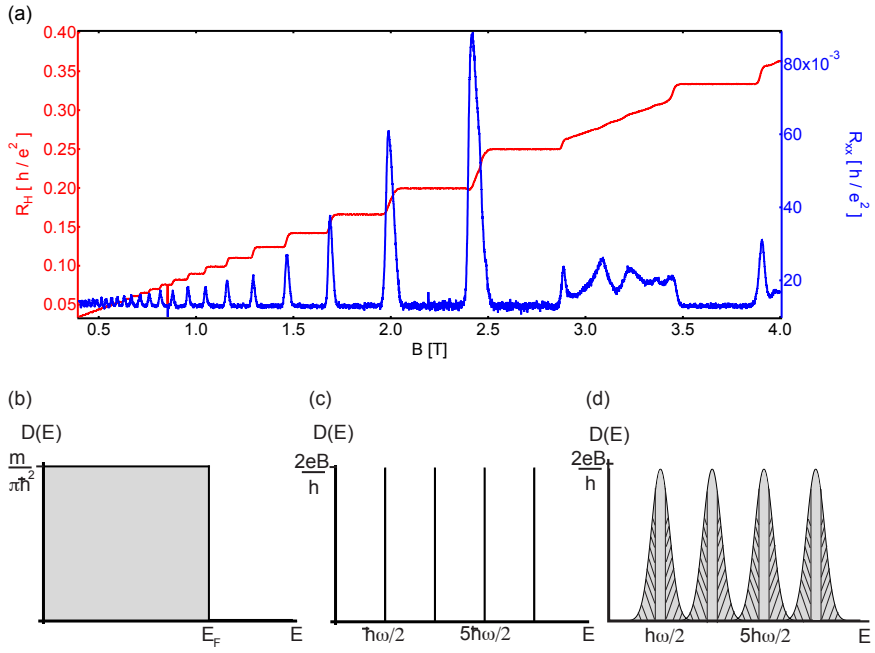

Figure 1.4: (a) Hall resistance (red), R_H, and longitudinal resistance (blue), R_{xx}, of a 2-dimensional system at cold temperatures as a function of magnetic field. (b) Density of states as a function of energy of a 2-dimensional electron gas at zero magnetic field (c) Density of states as a function of energy of a 2-dimensional electron gas in perpendicular magnetic field (d) Density of states as a function of energy of a 2-dimensional electron gas in perpendicular magnetic field with disorder

1.3.2 Integer Quantum Hall Effect

Now if we go to 2-dimensions and fairly cold temperatures[3], something interesting happens, as shown in Fig. 1.4(a). We don't see simply a linear relationship between R_H and B but plateaus at certain $\frac{1}{\nu}$ multiples of $\frac{h}{e^2}$. This comes about because the energy spectrum of the 2-dimensional fermion gas is no longer continuous but becomes discretely quantized into what are known as Landau levels. We start with a Fermi

[2]Sometimes R_{xy} is used to denote the Hall resistance but for the entirety of this thesis we will use R_H.

[3]The quantum Hall effect has actually been seen at room temperatures in monolayer graphene by Novosolev and coworkers [10].

sea at zero magnetic field with a constant density of states up to the Fermi energy as shown in Fig. 1.4(b). Now we apply a magnetic field and Landau levels start to form. To find the energies of these Landau levels, we remember that when an electron is subject to a magnetic field, the kinetic energy contribution to the Hamiltonian, $\frac{\mathbf{p}^2}{2m}$, becomes $\frac{(\mathbf{p}-e\mathbf{A})^2}{2m}$, where A is the vector potential associated with the magnetic field, p is the momentum and m is the mass of the fermion. We work in the Landau gauge and so our vector potential is $\mathbf{A} = Bx\hat{y}$. Our Hamiltonian then looks like:

$$H = \frac{p_x^2}{2m} + \frac{1}{2}m\omega^2(x + k_y l_b^2)^2, \tag{1.7}$$

where $\omega = \frac{eB}{m}$, k_y is the wavevector in the y-direction, and $l_b = \sqrt{h/eB}$ is the magnetic length. This is exactly the form of a harmonic oscillator with frequency ω and energy $E_n = \hbar\omega(n + \frac{1}{2})$, where n is an integer[4]. We can find the density of states in a magnetic field by remembering that magnetic field cannot change the density of states over a large energy range [12]. We can then divide the zero magnetic field density of states ($m/2\pi\hbar^2$) by the new single-particle density of states ($1/\hbar\omega$) to find the degeneracy of each state. Each Landau level is massively degenerate; the number of states per unit area is $g\frac{eB}{h}$, where g is determined by the symmetries in the system. The density of states as a function of energy now looks like Fig. 1.4(c). This degeneracy is equal to the number of flux quanta, $\phi_0 = h/e$ at a given magnetic field B. The filling factor $\nu = \frac{nh}{eB}$, where n is the density of the system, is the number of flux quanta per electron.

[4]For graphene, we make the substitution $\mathbf{q} \rightarrow \mathbf{q} - e\mathbf{A}$, which results in $E_n = \pm\sqrt{2e\hbar v_F^2 nB}$ for monolayer graphene and $E_n = \pm\hbar\omega\sqrt{n(n-1)}$ for bilayer graphene. Graphene and GaAs have different symmetries, which will turn out to be very interesting experimentally, but the rest of the phenomenology proceeds similarly between graphene and GaAs.

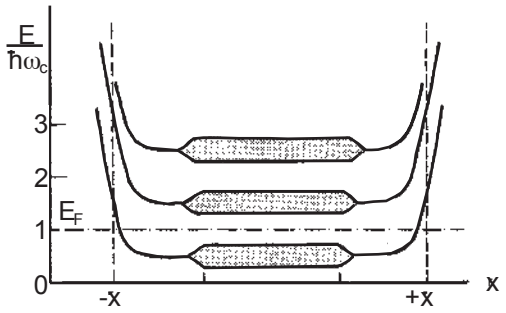

Figure 1.5: Sketch of energy versus position for a particle in a magnetic field confined in an infinite wall potential. A random disorder potential is present in the hashed region. Adapted from Ref. [11]

In a real sample, we have to add disorder into the system, which broadens out our delta functions and creates localized and extended states. The disorder potential $U(r)$ will create a landscape of hills and valleys in our sample. Now imagine that this landscape is completely unfilled but we start to increase our Fermi energy. At first, there will be isolated valleys which are filled by electrons but the valleys will not be connected to each other; these are localized states. As we increase the Fermi energy though, eventually we will reach a point where the edges of these valleys will be connected to each other resulting in a path across the entire sample, which are the extended states. As we keep going, however, we will reach a point where there are only isolated hilltops so we go back to being in localized states. The energy diagram shown in Fig. 1.4(d) indicates the localized states with slashes and the extended states in gray.

We also have to add a confining potential, which changes the energy levels as shown in Fig. 1.5. Note from Fig. 1.5 that the Fermi energy always meets each

Landau levels at 2 points at the edge of the sample, these are known as edge states. Semiclassically, these can be thought of the skipping orbits of electrons at the edges of the sample. The current in each edge state at zero temperature is equal to:

$$I = -\frac{e}{L_y}\int_{-\infty}^{\infty} dk \frac{L_y}{2\pi}\frac{1}{\hbar}\frac{\partial E}{\partial k} n_k = \frac{e}{h}\int_{\mu_L}^{\mu_R} dE = \frac{e^2}{h} V_H, \tag{1.8}$$

where L_y is the length of the sample in the y-direction, n_k is the probability that a state with wavevector k is occupied, μ_L and μ_R are the chemical potentials at the left and right edges of the sample [2]. Since we have one edge state for each Landau level, the total current is equal to $\nu\frac{e^2}{h}V_H$.

When the Fermi energy is filling an extended state, there are empty states that connect across the entire sample for electrons to occupy so R_H is increasing and R_{xx} (the resistance along the direction of the current), is nonzero. When the Fermi energy is outside of an extended state, current can only be carried along by the edge states since there are only localized states available in the bulk of the sample, which cannot contribute to transport. In this case, R_H stays constant while $R_{xx} = 0$ since there are no states for the electrons in edge states to backscatter into.

Now let's move on to something even more exciting.

1.3.3 Fractional Quantum Hall Effect

If we look at Fig. 1.6, we note that there are actually plateaus at fractions of a filling factor. These plateaus within partially filled Landau levels cannot be explained within our simple single-particle picture. We have to take into account interactions between electrons. The natural interaction to consider is the Coulomb interaction. The fractional quantum Hall effect arises because electrons desire to minimize the

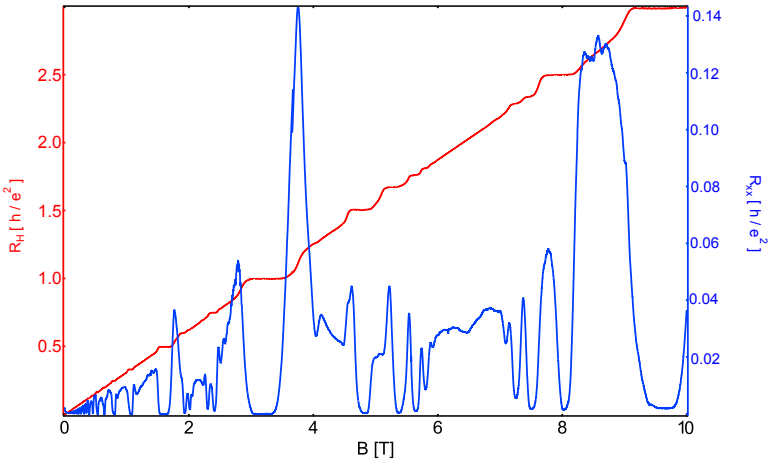

Figure 1.6: (a) Hall resistance (red), R_H, and longitudinal resistance (blue), R_{xx} of a high-mobility 2-dimensional system at cold temperatures as a function of magnetic field.

Coulomb repulsion between themselves.

In very clean samples the electrons interact to form a strongly correlated state, which minimizes the Coulomb repulsion between each electron. We can describe this state as electrons in a fictitious Chern-Simons gauge field. It turns out that the configuration that best describes this state is one where multiple flux quanta from the fictitious gauge field[5] group around an electron, which creates a large pocket where there are no electrons near each electron. You can think of this as the flux quanta screening around each electron, though this screening is much more rigid than the screening we usually consider [13].

At $\nu = 1/3$, the minimal energy state occurs when three flux quanta attach to each electron. The flux attachment builds into the many-body ground state wavefunction three zeros at the positions of the other electrons from the viewpoint of the electron we are concerned with [2]. It costs energy to move away from this filling and that is

[5]Flux quanta from the real applied magnetic field are distributed uniformly throughout the sample and do NOT form pockets around each electron

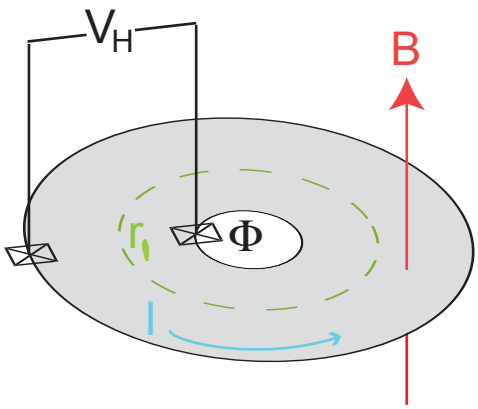

Figure 1.7: The Corbino disk geometry discussed in the text.

the origin of the gap at $\nu = 1/3$. The ground state wavefunction for $\nu = 1/m$ is:

$$\Psi = \prod_{i<j}^{N} (z_i - z_j)^m e^{-\frac{1}{4}\sum_{j=1}^{N}|z_j|^2}, \tag{1.9}$$

where z_i, z_j are the positions of the ith and jth particles, m is an odd integer, and N is the number of particles in the system [1]. M must be an odd integer to conform to the Pauli exclusion principle. Note that in the case of $m = 1$, this is just the ground state wavefunction at $\nu = 1$. This wavefunction also minimizes the Coulomb energy because the wavefunction gets very small as the particles get closer to each other.

To find why the quantization occurs at fractional plateaus, it is useful to think of a Corbino disk picture first used to explain the quantum Hall effect. This argument was given by Laughlin and Halperin in the early 1990's [11, 14]. For this argument, it is easiest if we work in the symmetric gauge where $\mathbf{A} = \frac{1}{2}Br\hat{\theta}$. We imagine a Corbino disk with leads on the inner ring and on the outer ring. The magnetic field B points out of the plane. We also imagine that there is some flux $\phi(t)$ through the center ring that we can change but changing this flux does not affect B. The arrangement is

shown in Fig. 1.7. The vector potential is then $\mathbf{A} = (\frac{1}{2}Br + \frac{\phi}{2\pi r})\hat{\theta}$. Our wavefunctions are $\Psi \sim e^{il\theta} f_\nu(r - r_l)$, where l and ν are integers, f_ν is the νth Hermite polynomial, and $r_l = (2(l\phi_0/B - \phi/B))^{1/2}$. Now we slowly increase the flux, which creates a voltage $V = \frac{-\delta\phi(t)}{\delta t}$. If we increase the flux by ϕ_0 then each r_l will replace r_{l+1}. The outermost state will move off of the outer edge and one inner state will appear on the inner edge, so we will move one electron from the inner edge to the outer edge. Each Landau level contributes one electron to each state. So if the νth Landau level is full then the current $I = \frac{\delta q}{\delta t} = \frac{\nu e}{t} = \frac{\nu e^2 V}{h}$. So we get that the quantized Hall resistance $R_H = \frac{1}{\nu}\frac{h}{e^2}$.

To add disorder to this geometry, we imagine that the disorder is confined to a finite region of the sample. Everything outside of the finite region proceeds as before but how do we cross the disordered region? Well, if the electron is in a localized state, its wavefunction does not extend beyond a small region and so does not encompass the flux. Changing the flux can not affect the localized state at all but there will always be extended states with lower energy than the localized state, which are affected by the changing flux. The electron we send in will be carried across the disordered region by extended states below it so sending one electron in will result in one electron coming out. So we again recover the quantized resistance, $R_H = \frac{1}{\nu}\frac{h}{e^2}$.

For the fractional quantum Hall plateaus, we add $1/\nu$ number of flux quanta, which will result in one electron being moved from the outer edge to the inner edge. By the same argument used above, $I = \frac{\delta q}{\delta t} = \frac{e}{t} = \frac{\nu e^2 V}{h}$, so we recover our fractionally quantized plateaus. Now what happens when we add only one flux quantum to the system? This is clearly not the same state as before since we have introduced a state

with no electron into the system, also known as a hole, so we must be in an excited state. But what is the charge of this hole? Remember that by moving $1/\nu$ flux quanta into the system we moved an electron from the inner to the outer edge so then our one hole must have charge νe [15]! So we don't need a particle accelerator to see fractional charges but just a dilution refrigerator, a magnet, and some very clean 2-dimensional material.

The fractionally charged particles also imply that these particles have fractional statistics. In quantum mechanics, we learn that when we interchange bosons they gain a phase of $e^{i2\pi}$ while fermions gain a phase of $e^{i\pi}$. And no other type of particle exists in 3 dimensions. To see why this is true, first imagine two indistinguishable particles. Now take one and encircle it around the other. The loop that the particle just followed can be smoothly deformed back into a point by using the third dimension. Mathematically, this imposes the constraint that $P^2 = 1$, where P is the operator that exchanges 2 particles [16]. The only two phases that satisfy this constraint are $e^{i2\pi}$ and $e^{-i\pi}$. In two dimensions, however, if we again make a loop around a particle, there is no way to smoothly deform the path into a point if the two particles cannot exist at the same point at any given time. Hence, we have no constraint on exchanging the particles and so the phase is e^{ir}, where r is any real number. Fractionally charged quasiparticles gain a phase of $\pi\nu$ when they exchange positions. To derive this requires a fair amount of calculation involving Berry's phase and the excited state wavefunction, so I direct the interested reader to notes written by Daniel P. Arovas [17], which has all of the relevant details. In some special fractional quantum Hall states, quasiparticle exchanges are theorized to lead not just to the accumulation

of a fractional phase but even to a change in the ground state of the particle! This turns out to be useful for a type of quantum computation which relies on topology and so is theoretically robust against local decoherence mechanisms [18].

Chapter 2

Dynamic Nuclear Polarization in the Integer and Fractional Quantum Hall Effect

A. Kou, D. T. McClure, C. M. Marcus

Department of Physics, Harvard University, Cambridge, Massachusetts 02138, USA

L. N. Pfeiffer and K. W. West[1]

Department of Electrical Engineering, Princeton University, Princeton, New Jersey 08544, USA

[1]This chapter is adapted with permission from Phys. Rev. Lett **105**, 056804 (2010).

2.1 Introduction

We investigate DNP in a gate-defined QPC and identify surprising correspondences between the IQH and FQH regimes, which we interpret within a composite fermion picture. In contrast to the situation in bulk FQH systems, where DNP may change the spin configuration at a given filling factor, we find that DNP in the vicinity of a QPC can evidently induce changes in density (hence local filling factor) within the constriction. Resistance plateaus as a function of B in both IQH and FQH regimes shift and change in length following application of a nonzero dc bias. Using resistively detected nuclear magnetic resonance (NMR), we demonstrate that the applied bias induces nuclear polarization. Interestingly, the pattern of shifting plateaus is symmetric about the the half-filled first Landau level, $\nu = 1/2$. Comparable shifts are also found in the IQH regime. We determine the sign of the induced Overhauser field to be opposed to the applied field in all cases, and estimate the magnitude of the Overhauser field by observing its effects at large filling factors, where the Overhauser field can exceed the applied field and effectively reverse the sign of the Zeeman field. Finally, we interpret related DNP effects in the IQH and FQH regimes in terms of simple Zeeman-split CF edge states.

2.1.1 Composite Fermions

An appealing physical picture of the fractional quantum Hall (FQH) effect is the composite fermion model [19–21], in which an even number, $2m$, of flux quanta ($\phi_0 = h/e$) bind to each electron, creating a composite fermion (CF) that feels an effective field, $B^* = B - 2mn\phi_0$, where B is the applied field perpendicular to the plane

of the electron gas and n is the electron density. The effective field quantizes the CF energy spectrum into the analogue of electronic Landau levels; the FQH effect becomes the integer quantum Hall (IQH) effect of CFs. At filling factor $\nu = 1/2$, corresponding to $B^*= 0$ for CFs with two attached flux quanta ($m = 1$), the CFs form a Fermi sea that can have ground states with different degrees of spin polarization [22, 23]. Composite fermions at other filling factors also have non-trivial spin-polarized ground states. For example, $\nu = 2/3$ ($\nu_{CF} = -2$) and $\nu = 2/5$ ($\nu_{CF} = 2$) have been observed to have both spin-polarized and spin-unpolarized ground states [24, 25].

2.1.2 Dynamic Nuclear Polarization

Electrons and nuclei interact through the hyperfine interaction, given by the Hamiltonian:

$$H_{\text{hyperfine}} \;=\; A\mathbf{I}\cdot\mathbf{S} \;=\; \frac{1}{2}A[I_+S_- + I_-S_+] + AI_zS_z, \tag{2.1}$$

where A is the hyperfine constant ($A < 0$ for GaAs), $\mathbf{I}$ is the total nuclear spin, and $\mathbf{S}$ is the total electron spin. A finite nuclear polarization generates a hyperfine field B_{N} that changes the Zeeman energy felt by the electrons, a change which can be detected in transport measurements [26]. Polarized electrons can also change the Zeeman energy felt by the nuclei, resulting in a Knight shift of the NMR frequency of the nuclei, allowing the detection of electron spin polarization [27].

2.1.3 Previous Work

Dynamic nuclear polarization (DNP) has been used to investigate both the IQH and the FQH regime using transport measurements [23, 28–43]. In both regimes,

electron spin flips are accompanied by opposite nuclear spin flops. In gate-confined GaAs microstructures in the IQH regime, Wald *et al.* [28] showed that scattering from the lowest (spin-up) Landau level to the second (spin-down) Landau level flops a nuclear spin from down to up, which in turn increments the Overhauser field, B_{N}, opposite to the applied field, B. The resulting reduction in total effective Zeeman field was then detected in transport [28]. DNP in a quantum point contact (QPC) with only Zeeman splitting has also been observed [44]. In bulk two-dimensional (2D) geometries, breakdown of the IQH and FQH effects at high bias can also induce DNP [34,35,38,40,42,43]. In this case, the direction of the resulting Overhauser field depends on experimental details. In the FQH regime, much of the work—in bulk and in microstructures—has focused on $\nu = 2/3$ [31–33,37], where DNP is attributed to spin-flip tunneling between spin-unpolarized and spin-polarized domains. Bulk 2D studies using DNP and nuclear relaxation at $\nu = 1/2$ were used to investigate the degree of spin polarization of the metallic CF state as a function of applied field [23, 39, 41]. Despite the extensive literature on this topic, on both bulk and confined devices, no explicit connection between DNP in the IQH and FQH regimes—creation or detection—has been drawn to our knowledge.

2.2 Devices

Measurements were carried out on four devices [Figs. 2.1(b-e)], showing similar behavior. Data presented are from devices in Figs. 2.1(b,c). The devices were fabricated on a two-dimensional electron gas (2DEG) in a symmetrically Si-doped GaAs/AlGaAs 48 nm quantum well structure located 400 nm below the wafer sur-

face with density $n = 7.8 \times 10^{14}$ m^{-2} and mobility $\mu = 13$ million cm^2/V·s measured in the dark. Similar behavior was observed on a different wafer with roughly twice the density. Square mesas were wet-etched [Fig. 2.1(a)], and Ti/Au (5 nm/15 nm) surface gates were patterned using electron-beam lithography. Depleted gates except V_{L2} were set to ~ -1.5 V. Gate V_{L2}, when used, was set to ~ -0.8 V. Other gates were grounded.

2.3 Methods

Measurements were made using a current bias, I, with dc component, I_{DC}, up to 100 nA and an ac component of 0.4 nA at 153 Hz. The electron temperature was ∼50 mK. We typically measure the diagonal voltage, V_{D}, which is the voltage

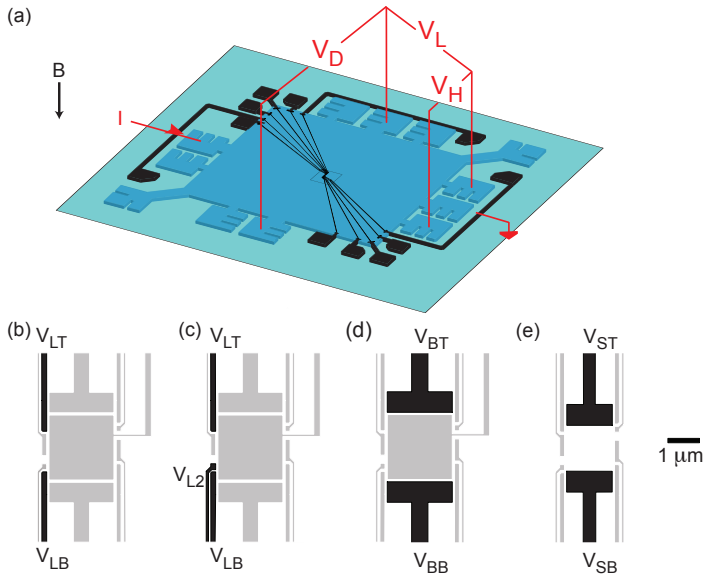

Figure 2.1: (a) Schematic of device layout on square mesa, with current bias, indicating positions of ohmic contacts where diagonal voltage, V_{D}, across the device, as well as bulk Hall voltage, V_H and longitudinal voltage, V_L, are measured. Gate layouts of (b) 1 μm, (c) 750 nm, (d) 2 μm, and (e) 1.4 μm constrictions are shown, with 1 μm scale bar. Depleted gates shown in black, grounded gates shown gray.

difference between incoming edge states on opposite sides of the QPC. Lock-in measurements of the diagonal resistance, $R_{\mathrm{D}} \equiv dV_{\mathrm{D}}/dI$, were used to determine the local filling factor within the QPC, $\nu_{\mathrm{D}} \equiv h/R_{\mathrm{D}}e^2$. Two procedures were used to apply I_{DC} to the QPC. In the first procedure ("holding"), I_{DC} was set to a value I_{hold} for a time t_{hold} before being set back to 0. Unlike in less symmetric geometries [34], results did not depend on the sign of I_{hold}. In the second procedure ("sweeping"), I_{DC} was swept from a positive value (I_{max}) to a negative value ($-I_{\mathrm{max}}$) and then swept back to 0; sweep direction made no difference. The two procedures lead to similar overall behavior, as well.

2.4 Effects of Polarized Nuclei

Figure 2.2(a) shows R_{D} as a function of B and I_{DC} in the 750 nm constriction [Fig. 2.1(c)], acquired using the sweeping procedure at each field then stepping the field downward. Comparing zero-bias data taken prior to sweeping (red) with the zero-bias cut through data (black) shows that sweeping causes the $\nu_{\mathrm{D}} = 1/3$ plateau to extend to lower field, just past the high-field edge of the $\nu_{\mathrm{D}} = 2/5$ plateau in (red) data taken prior to sweeping I_{DC} (red). The transition region between $\nu_{\mathrm{D}} = 1/3$ and $\nu_{\mathrm{D}} = 2/5$ becomes abrupt after sweeping dc bias; in the prior data, the transition is seen to be gradual. Figure 2.2(b) shows similar extensions of plateaus for ν_{D} between 2/5 and 2/3 in the 1 μm constriction [Fig. 2.1(b)]. Here, the bias was applied using the holding procedure applied at each field, then the field stepped downward. The black trace shows R_{D} after the return to zero dc bias at each field while the red trace was measured with no dc bias applied.

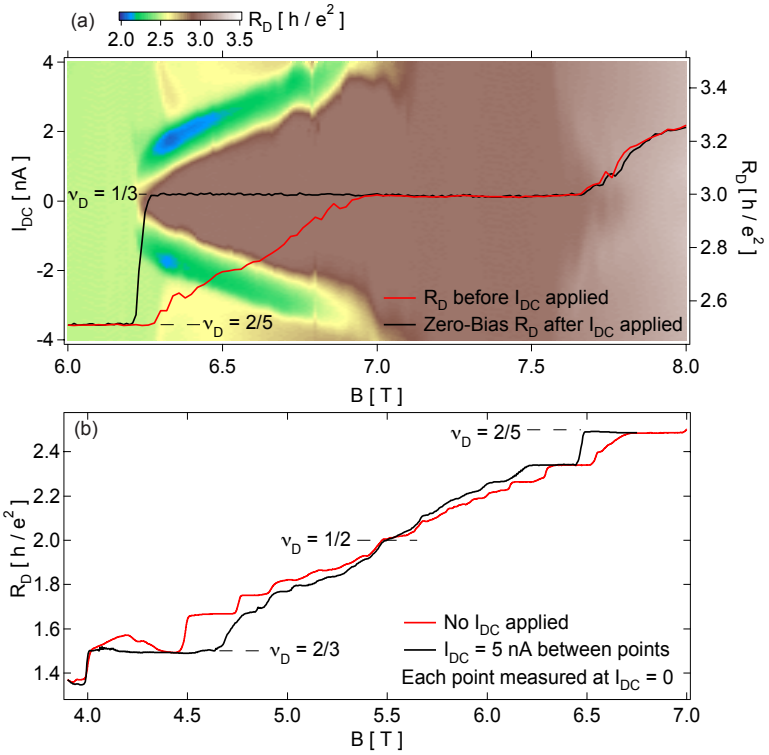

Figure 2.2: (a) R_{D} as a function of B and I_{DC} in the 750 nm constriction. Red trace indicates R_{D} as a function of B before I_{DC} has been applied to the constriction. Black trace indicates R_{D} as a function of B at $I_{\mathrm{DC}} = 0$ after applying a nonzero I_{DC} to the constriction. (b) R_{D} as a function of B in the 1 μm constriction. Red trace indicates R_{D} before I_{DC} has been applied to the constriction. Black trace indicates R_{D} measured at $I_{\mathrm{DC}} = 0$ after $I_{\mathrm{DC}} = 5$ nA has been applied to the constriction.

The pattern of shifts and extensions of plateaus of R_{D} [Fig. 2.2(b)] exhibits a striking symmetry about $\nu_{\mathrm{D}} = 1/2$: applying then removing dc bias at each field causes all plateaus to shift toward $\nu_{\mathrm{D}} = 1/2$, which, as a symmetry point, does not change position [1] Bulk Hall and longitudinal resistances do not exhibit any change in behavior after applying I_{DC}.

Similar shifts and extensions of plateaus occur when the bias is applied at a

[1] On the high-field side of the symmetry point ($\nu_{\mathrm{D}} < 1/2$) shifts and extensions of plateaus require that the bias is applied between plateaus, while on the low-field side ($1/2 < \nu_{\mathrm{D}} < 2/3$) shifting occurs regardless of where I_{DC} is applied.

different filling factor from where its effects are observed. Changes in filling factor can be accomplished by either changing field or QPC gate voltage. This is illustrated in Figs. 2.3(a-c), which show R_{D} as a function of time, measured at the same field and gate settings, following application of I_{DC} at three different filling factors. Field and gate voltages were first set to give a well-quantized $\nu_{\mathrm{D}} = 3/5$ plateau in the 1 μm constriction prior to application of I_{DC}. Then, either field or gate voltage was used to change ν_{D}, where dc bias sweeping procedure was applied. Field or gate voltage values were then returned to the settings where $\nu_{\mathrm{D}} = 3/5$ was originally observed. In all cases—regardless of where I_{DC} is applied—after a transient (due to residual heating from I_{DC}) R_{D} settles at a value indicating $\nu_{\mathrm{D}} = 2/3$ for tens of minutes before suddenly returning to its original $\nu_{\mathrm{D}} = 3/5$ value.

Plateau shifting with characteristic symmetry about $\nu = 1/2$ is also observed when I_{DC} is applied at a single filling factor rather than at each value of B. In Fig. 2.3(d), the I_{DC} sweeping procedure applied once, just below $\nu = 1/3$ ($B = 7.50$ T), before sweeping field downward to $\nu = 2/3$ ($B = 4.00$ T) with I_{DC} at zero. Symmetry about $\nu = 1/2$ is evident despite the asymmetry of where the dc bias was applied. Similar behavior is seen when I_{DC} is applied once at $\nu = 3/5$ ($B = 4.50$ T) before sweeping the magnetic field upward toward $\nu = 1/3$ ($B = 7.80$ T) with $I_{\mathrm{DC}} = 0$ [Fig. 2.3(d)]. From these data, we conclude that the observed symmetry $\nu = 1/2$ reflects the *response* of the system to a common, roughly field-independent, physical mechanism.

The slow relaxation seen in Figs. 2.3(a-c) suggests DNP as the origin of the effects of applied bias. This is confirmed using resistively detected NMR. Following sweeping

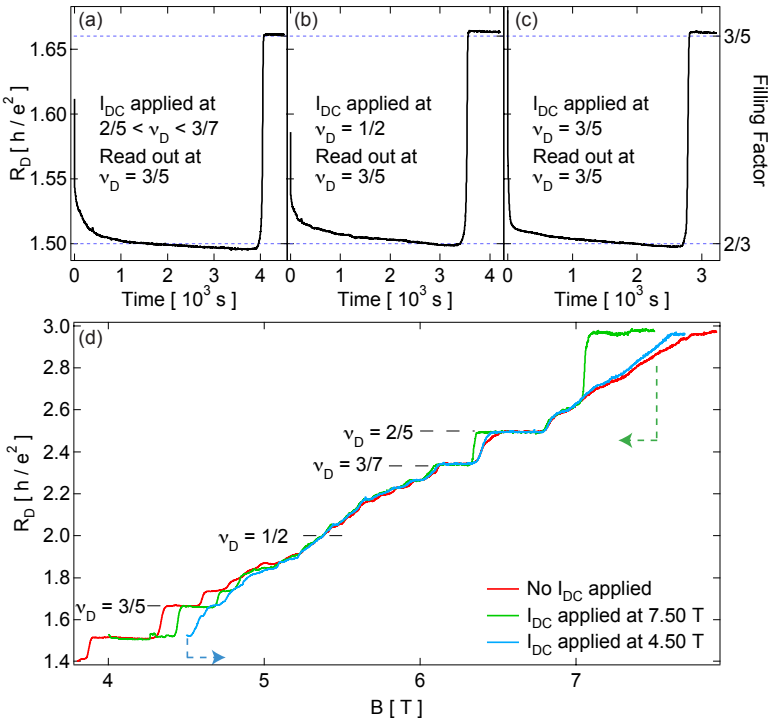

Figure 2.3: (a-c) R_D as a function of time measured in the 1 μm constriction at $\nu_D = 3/5$ after $I_{DC} = 10$ nA was applied at $2/5 < \nu_D < 3/7$, $\nu = 1/2$, and $\nu_D = 3/5$. (d) R_D as a function of B in the 1 μm constriction. Red trace indicates R_D before I_{DC} has been applied. Green trace indicates R_D after $I_{DC} = 20$ nA has been applied at $B = 7.50$ T. Blue trace indicates R_D after $I_{DC} = 34$ nA has been applied at $B = 4.50$ T.

application of I_{DC}, an ac magnetic field pulse at frequency f_{NMR} is applied using a six-turn coil that orients the ac field predominantly in the plane of the electron gas. When f_{NMR} matches one of the expected NMR frequencies, R_D returns to the value measured before applying I_{DC}. Figures 2.4(a,b) show depolarization signatures in R_D for ^{75}As NMR at $\nu_D = 1/3$ and $\nu_D = 3/5$. Similar signatures are also observed for ^{69}Ga and ^{71}Ga NMR frequencies (not shown).

Following DNP at $\nu_D = 3/5$, ramping the field to the edge of the $\nu_D = 1$ plateau causes all plateaus to return to their unpolarized positions. This rapid depolarization can be understood by the presence of skyrmions near $\nu = 1$, which are known to

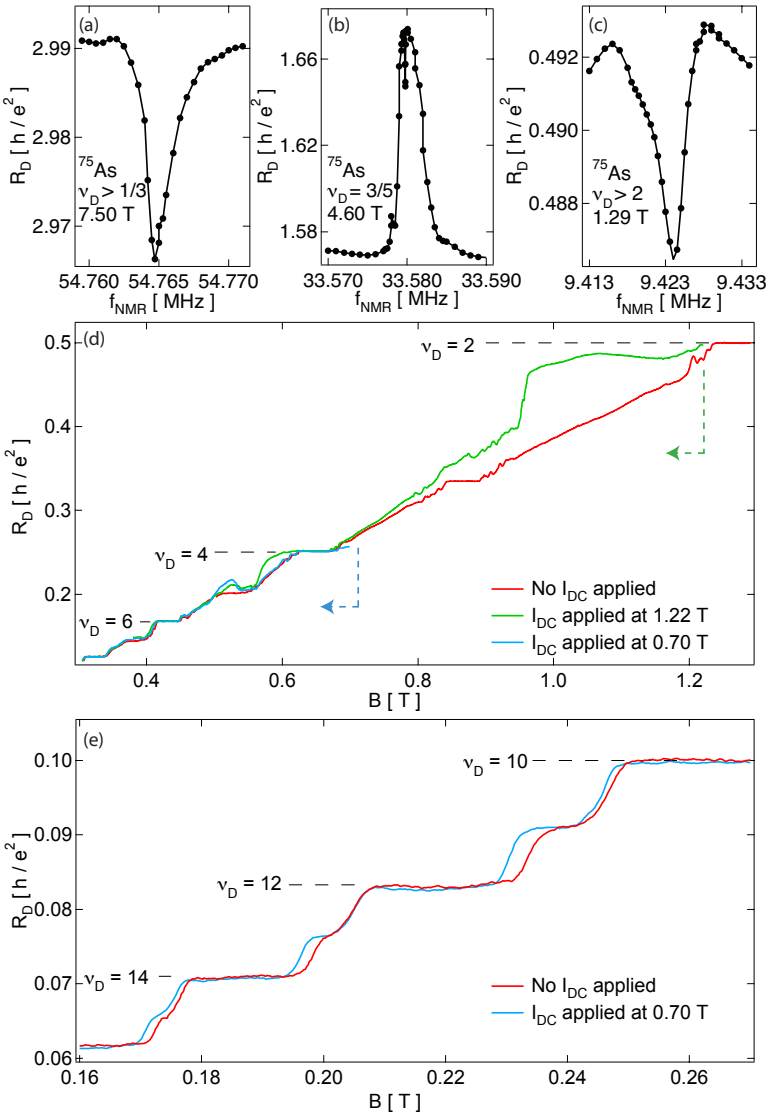

Figure 2.4: (a-c) R_D as a function of f_{NMR} in the 1 μm constriction at B = 7.50 T, 4.60 T, and 1.29 T. [2] (d,e) R_D as a function of B in the 1 μm constriction. Red trace indicates R_D before I_{DC} has been applied. Green trace indicates R_D after I_{DC} = 54 nA has been applied at B = 1.22 T. Blue trace indicates R_D after I_{DC} = 95 nA has been applied at B = 0.70 T.

cause relaxation of nuclear polarization [45–47].

At lower fields, plateau shifts and extensions in the IQH regime are seen following DNP from I_{DC} applied between (not directly on) IQH plateaus. Following DNP, spin-split plateaus at $\nu_D = 3$ and $\nu_D = 5$ disappear for several minutes [Fig. 2.4(d)].

NMR confirms the DNP interpretation [Fig. 2.4(c)]. The sign and magnitude of the Overhauser field can also be deduced in the IQH regime. For B_N along B, ($B_N > 0$), spin splitting will always increase with DNP; for B_N opposing B, spin splitting will decrease for mild DNP, reach zero for $|B_N| = B$ and again increase when $|B_N| > B$ (with reversed spin splitting). Comparing Figs. 2.4(d,e), we see that for $B \sim 0.5-1$ T, the odd (spin-split) plateaus are weakened by DNP, whereas for $B \sim 0.2$ T, odd plateaus are enhanced by DNP. We conclude that B_N induced by DNP is directed opposite to B and is between 0.2 and 0.5 T in magnitude.

To connect DNP effects between IQH and FQH regimes, we polarize in the one regime and read out in the other. For instance, we apply I_{DC} using the sweeping procedure at $\nu_D = 2$, followed by ramping to a value of field where $\nu_D = 3/5$ before polarization. Depolarization from skyrmions upon passing through $\nu_D = 1$ are avoided by fully depleting the QPC during the field ramp. We find that R_D initially indicates $\nu_D = 2/3$ value before sharply returning to the $\nu_D = 3/5$ value after several minutes. Reversing the order—polarizing at $\nu_D = 3/5$ and reading out at $2 < \nu_D < 3$—yields analogous results. We conclude from both procedures that the direction of induced Overhauser field opposes the applied field in both IQH and FQH regimes. We also conclude that the relevant DNP occurs in the QPC (not downstream) since depolarization by skyrmions was eliminated by depleting only the electrons in the QPC constriction.

2.5 Discussion

In the IQH regime, DNP presumably occurs by spin-up electrons at high-bias entering the QPC flipping into empty spin-down states, accompanied by a nuclear flop from spin down to spin up. Because dc bias exceeds Zeeman splitting but not cyclotron energy, the opposite mechanism, involving flip-flop spin relaxation between different Landau levels, which would would tend to align B_{N} and B, does not occur.

Evidently, a similar mechanism appears to occur in the FQH regime. Within a CF picture, even filling factors can have spin-unpolarized ground states while odd filling factors are always at least partially polarized [19]. Hence, similar to electrons, CFs can be excited from a spin-up to a spin-down state. Within this model, for example, exciting CFs from a spin-up subband of $\nu = 3/5$ ($\nu_{\mathrm{CF}} = -3$) to a spin-down subband of $\nu = 4/7$ ($\nu_{\mathrm{CF}} = -4$) will result in $B_{\mathrm{N}} < 0$. Excitations from spin-down to spin-up states may also be possible, however, since the CF Zeeman energy is comparable to the CF cyclotron energy [19].

We interpret the effect of B_{N} on plateau structure as depending on ground-state spin configurations at successive filling factors. If successive states have different degrees of spin-polarization, B_{N} will change the length of the associated plateaus. If successive states are both spin-polarized, then B_{N} will shift plateau positions. In the IQH regime, odd filling factors are spin-polarized while even filling factors are spin-unpolarized, hence B_{N} causes plateaus at even filling factors to lengthen at the expense of plateaus at odd filling factors. In the FQH regime, the more spin-polarized state will also be destabilized by B_{N}, leading to a shorter plateau. We observe the destabilization of more spin-polarized plateaus in favor of less spin-polarized plateaus

in both regimes: at $3/5 \leq \nu_{\mathrm{D}} \leq 2/3$ ($-3 \leq \nu_{\mathrm{CF}} \leq -2$) in Fig. 2.2(b) in the FQH regime and at $2 \leq \nu_{\mathrm{D}} \leq 3$ in Fig. 2.4(d) in the IQH regime. The changes in the lengths of the plateaus observed in Fig. 2.2(b) are analogous to those observed in Fig. 2.4(d), suggesting that CF's in the FQH regime are exhibiting the same behavior as electrons in the IQH regime. Within this picture, shifts in plateau position can only occur in the FQH regime, where successive states can both be spin-polarized. A change in Zeeman energy will not affect the size of the gap between spin-polarized CF Landau levels but will shift the energies of the levels equally. When the Zeeman energy is decreased, the energy of each spin-polarized level increases, causing a local depopulation of electrons in the QPC. Each energy level will then be filled at a lower magnetic field; the start of each plateau will then appear at a lower field than before DNP. We observe this shifting of the plateaus at $1/3 < \nu < 2/5$ [Fig. 2.2(a)]. Finally, while DNP is found to readily occur at $\nu_{\mathrm{D}} = 1/2$, it leaves little or no signature in R_{D} at $\nu_{\mathrm{D}} = 1/2$, by symmetry, but can be observed by moving to another filling factor after DNP, as seen in Fig. 2.3(b).

2.6 Acknowledgements

We thank J. P. Einsenstein, B. I. Halperin, I. Neder, M. S. Rudner, and K. von Klitzing for enlightening discussions. Research funded by Microsoft Corporation Project Q, IBM, NSF (DMR-0501796), and Harvard University. Device fabrication at Harvard's Center for Nanoscale Systems.

Chapter 3

Coulomb Oscillations in Antidots in the Integer and Fractional Quantum Hall Regimes

A. Kou, C. M. Marcus

Department of Physics, Harvard University, Cambridge, Massachusetts 02138, USA

L. N. Pfeiffer and K. W. West[1]

Department of Electrical Engineering, Princeton University, Princeton, New Jersey 08544, USA

[1]This chapter is adapted with permission from Phys. Rev. Lett **108**, 256803 (2012).

3.1 Introduction

We report measurements of resistance oscillations in gate-defined antidots of two sizes, comparing integer and fractional filling factors in the constrictions between the antidot and adjacent gates that extend to the sample edge. Oscillations as a function of perpendicular magnetic field and antidot gate voltage were measured in 2D sweeps, and dominant frequencies extracted from 2D Fourier spectra. For integer filling in the constrictions, magnetic field oscillation frequencies were found to be proportional to the filling factor in the constrictions, consistent with a Coulomb charging model. At $\nu = 2/3$, the magnetic field oscillation frequency was found to be consistent with a single charged edge within a generalized Coulomb charging picture, with the charge-carrying edge state located slightly closer to the antidot than the single edge found at $\nu = 1$. Gate-voltage oscillations provide a direct measurement of the tunneling quasiparticle charge. Normalizing to a tunneling charge of e at $\nu = 1$, which determines the gate voltage lever arm, we find a tunneling charge consistent with e for all measured integer filling factors, and a tunneling charge consistent with $e^* = (2/3)e$ at $\nu = 2/3$.

3.1.1 Fractional Quantum Hall Edge States

The fractional quantum Hall effect occurs when a high-mobility two-dimensional electronic gas (2DEG) is subject to a perpendicular applied magnetic field. At low temperature, electrons in the bulk of the 2DEG condense into incompressible states [1], with extended states at the sample edge carrying charge, spin, and energy. It was theoretically shown that for Laughlin states such as filling factor $\nu = 1/3$, a

single chiral edge state carries excitations with fractional charge [48]. A more complicated structure is predicted for hole-conjugate fractions such as $\nu = 2/3$, where counter-propagating edge states hybridize in the presence of edge disorder, leading to a forward-propagating charge mode and a reverse-propagating neutral mode [49–52]. Contrasts between the two counter-propagating modes at $\nu = 2/3$ and the simpler situation at $\nu = 2$, where two forward-propagating modes remain separated and independent, have been discussed theoretically [50, 52].

Ashoori *et al.* investigated the $\nu = 2/3$ edge experimentally using edge magnetoplasmon propagation and found only a single charged edge mode [53]. Recent measurements of current noise through a quantum point contact (qpc) at bulk filling $\nu = 2/3$ found finite shot noise at half transmission of the qpc, which was interpreted as indicating a single composite 2/3 edge [54]. In addition, a tunneling charge of $e^* = (2/3)e$ was observed at low temperature, decreasing to $e/3$ above 0.1 K [54]. Subsequent theory addressed these surprising results by considering the agglomeration of $e/3$ quasiparticles at low temperatures [56]. Bid *et al.* also observed signatures of a neutral mode near $\nu = 5/2$ by measuring shot noise [55].

3.1.2 Antidots

Antidots have been used to study tunneling and confinement effects in both the integer and fractional quantum Hall regimes [57–68]. An antidot is a potential hill formed by depleting a region of 2DEG. The depletion is usually achieved by applying a negative voltage to a top gate or by etching away a region of the 2DEG [67]. At zero magnetic field, the antidot just looks like a scattering site for the electrons but

as the magnetic field is increased, the electrons will start to be bound around the antidot. In a single-particle picture, electrons occupy single-particle states encircling the antidot. As the magnetic field is increased, the single-particle states move upward in order to keep the flux through the state constant. When the change in flux is equal to a flux quantum, an electron can tunnel off of the antidot resulting in oscillations. Early experiments by Hwang *et al.* [57] found resistance oscillations as a function of magnetic field and channel gate voltage for a density slightly below $\nu = 1$ in the constrictions between the antidot and sample edges. The observed field period, corresponding to one flux quantum through the antidot, was interpreted in terms of a single-particle Aharonov-Bohm phase [57].

3.1.3 Coulomb Oscillations

Subsequent experiments near $\nu = 2$ in the constrictions found a field period corresponding to $h/2e$ ($\phi_0/2$) through the antidot, motivating an alternative interpretation in terms of Coulomb charging of two isolated edge states [59]. Coulomb charging of an antidot was observed directly by Kataoka *et al.* at both $\nu = 1$ and $\nu = 2$ using a qpc charge sensor [63]. Goldman *et al.* found the field period of oscillations to depend on the filling factor through the constriction, interpreting this dependence as a signature of Coulomb charging of multiple isolated edges surrounding the antidot [68]. Recent theory by Ihnatsenka *et al.* captures many of the effects observed experimentally in antidots in the integer quantum Hall regime [70]. In the Coulomb charging picture, the single-particle states encircling the antidot interact to form compressible and incompressible strips around the antidot. As the magnetic field increases, these

compressible and incompressible strips move upward in order to keep the flux through the loop constant. But the negative charge density has changed while the positive background density has not, which means that excess charge has been created around the antidot by the magnetic field. When the excess charge is equal to e, the antidot can relax. This picture is much like the Coulomb picture developed for quantum dot interferometers in the integer and fractional quantum Hall regimes [71, 72].

Much less experimental work on antidots has been reported in the fractional regime despite numerous theoretical proposals related to this system [73–78]. A key experiment was the measurement of fractional tunneling charge, $e^* = e/3$, for an antidot with $\nu = 1/3$ in the constrictions, based on the back-gate voltage and magnetic field periods of observed resistance oscillations [60].

3.2 Devices

Antidot devices with 1 μm and 2 μm diameter antidots were fabricated on a symmetrically Si-doped GaAs/AlGaAs 30 nm quantum well structure located 230 nm below the wafer surface, with density $n = 1.6 \times 10^{15}$ m^{-2} and mobility $\mu = 1{,}200$ m^2/V·s measured in the dark. A Ti/Au (8 nm/42 nm) screening gate was first patterned using electron-beam lithography on a wet-etched mesa [purple gate in Fig. 3.1(a)]. The sample was then coated with 30 nm of HfO_2 using atomic layer deposition. A circular antidot [Ti/Au (8 nm/42 nm)] was next patterned on top of the HfO_2, positioned to extend beyond the edge of the screening gate, with connection to a remote bonding pad via a "pan handle" depletion gate that runs on top of the screening layer, so that only the 2DEG under the antidot is depleted when the gate is activated [Fig. 3.1(a,

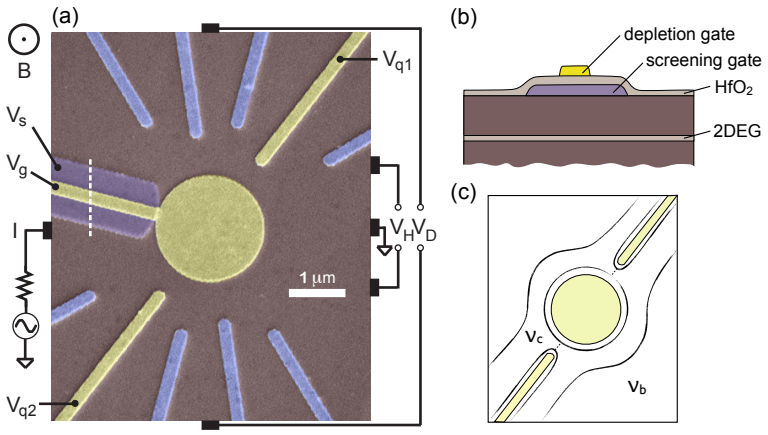

Figure 3.1: (a) False color SEM of the larger antidot device with 2 μm diameter. Diagonal voltage, $V_{\rm D}$, across the device, as well as bulk Hall voltage, V_H, are measured as shown. Depleted gates are indicated in yellow, grounded gates are indicated in blue. The qpc constriction sizes range from 500 nm to 1.5 μm. (b) Cross section of the device taken along the dashed line in (a). The antidot gate is separated from the screening gate by a 30 nm HfO_2 layer. (c) Schematic layout of the edge states through the device when $\nu_{\rm c} = \nu_{\rm c}^{-}$. The bulk filling factor, ν_b, and the constriction filling factor, ν_c, are indicated.

b)]. Effects of the screening gate were checked by measuring the resistance between two ohmic contacts on either side of the antidot and screening gates. We detected no change in the resistance when we varied the antidot gate voltage while the screening gate was grounded.

3.3 Measurements

Transport measurements were made using a current bias I of 0.3 nA at 101 Hz, with magnetic field, B, applied perpendicular to the plane of the 2DEG, in a dilution refrigerator with base temperature ∼10 mK. QPC gate voltages $(V_{\rm q1}, V_{\rm q2})$, were trimmed around −1.0 V to symmetrize the device, i.e., to give the same filling factors in the two constrictions. The antidot gate voltage, $V_{\rm g}$, was then swept around −0.9 V, yielding periodic resistance oscillations. The screening gate and all unused

qpc gates were grounded. The diagonal voltage, $V_{\rm D}$, was measured between incoming edge states on opposite sides of the device [Fig. 3.1(c)], and the diagonal resistance, $R_{\rm D} \equiv dV_{\rm D}/dI$, was used to determine the filling factor in the qpcs, $\nu_{\rm c} = h/(R_{\rm D}e^2)$. The bulk Hall resistance, $R_{\rm H} \equiv dV_{\rm H}/dI$, was simultaneously measured using contacts away from the antidot [Fig. 3.1(a)]. Figure 3.1(c) schematically shows the bulk filling factor, ν_b, along with the filling factor in the constrictions, $\nu_{\rm c}$, in the condition where $R_{\rm D}$ is slightly larger than the resistance of well-quantized plateaus. This condition, measured on the high-field side of the $\nu_{\rm c}$ plateau in $R_{\rm D}$, is denoted $\nu_{\rm c}^-$.

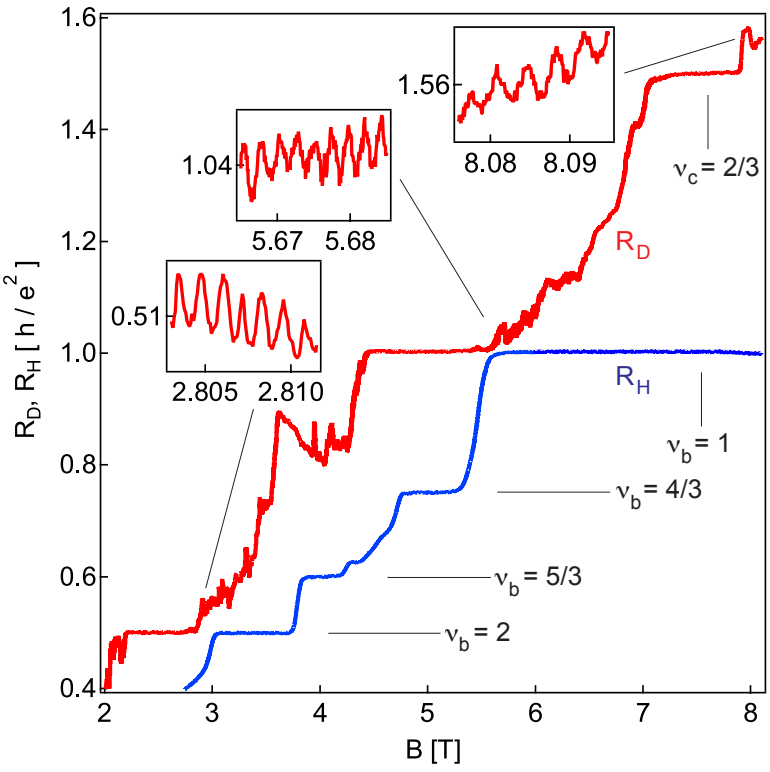

Figure 3.2: Diagonal resistance, $R_{\rm D}$ (red), and bulk Hall resistance, $R_{\rm H}$ (blue), as a function of perpendicular magnetic field, B, in the 1 μm diameter antidot with the 500 nm qpcs activated. Insets show regions of oscillations at $\nu_{\rm c} = 2^-$, $\nu_{\rm c} = 1^-$, and $\nu_{\rm c} = 2/3^-$.

3.4 Oscillations at $\nu = 2, 1,$ and $2/3$

Figure 3.2 shows $R_{\mathrm{H}}(B)$ and $R_{\mathrm{D}}(B)$ at fixed gate voltages in the 1 μm diameter antidot with the 500 nm qpcs activated. Insets show detailed views of periodic oscillations in $R_{\mathrm{D}}(B)$, with periods $\Delta B = 2.1$ mT for $\nu_{\mathrm{c}} = 1^{-}$, $\Delta B = 1.0$ mT for $\nu_{\mathrm{c}} = 2^{-}$, and $\Delta B = 2.9$ mT for $\nu_{\mathrm{c}} = 2/3^{-}$. Aperiodic fluctuations in $R_{\mathrm{D}}(B)$ were also observed on the low-field sides of the plateaus. The period of 2.1 mT at $\nu_{\mathrm{c}} = 1^{-}$ corresponds to $\phi_0 = h/e$ through an area of 2.0 $\mu\mathrm{m}^2$, larger than the lithographic area of the antidot, $A = 0.8$ $\mu\mathrm{m}^2$. We attribute the larger area to the finite depletion length of the antidot top gate, as discussed quantitatively below. The period of 1.0 mT at $\nu_{\mathrm{c}} = 2^{-}$ corresponds to $\phi_0/2$ going through a device of about the same area. Continuing this trend for integer states, oscillations observed at $\nu_{\mathrm{c}} = 3^{-}$ had a field period corresponding to $\phi_0/3$; oscillations at $\nu_{\mathrm{c}} = 4^{-}$ had a field period corresponding to $\phi_0/4$ (not shown). The observed scaling of field periods with antidot-bound edge states, i.e.

$$\Delta B = \frac{h}{NeA}, \tag{3.1}$$

where N is the number of antidot-bound edge states and A is the effective area of the antidot, is consistent with previous experiments in the integer quantum Hall regime in antidots [59, 68].

Figure 3.3 shows R_{D} with a smooth background subtracted, denoted δR_{D}, as a function of both B and V_{g} in the 2 μm diameter antidot with 500 nm qpcs activated at $\nu_{\mathrm{c}} = 1^{-}$, $\nu_{\mathrm{c}} = 2^{-}$, and $\nu_{\mathrm{c}} = 2/3^{-}$ along with corresponding two-dimensional (2D) Fourier power spectra. The 2D plots of δR_{D} reveal positively sloped stripes in all

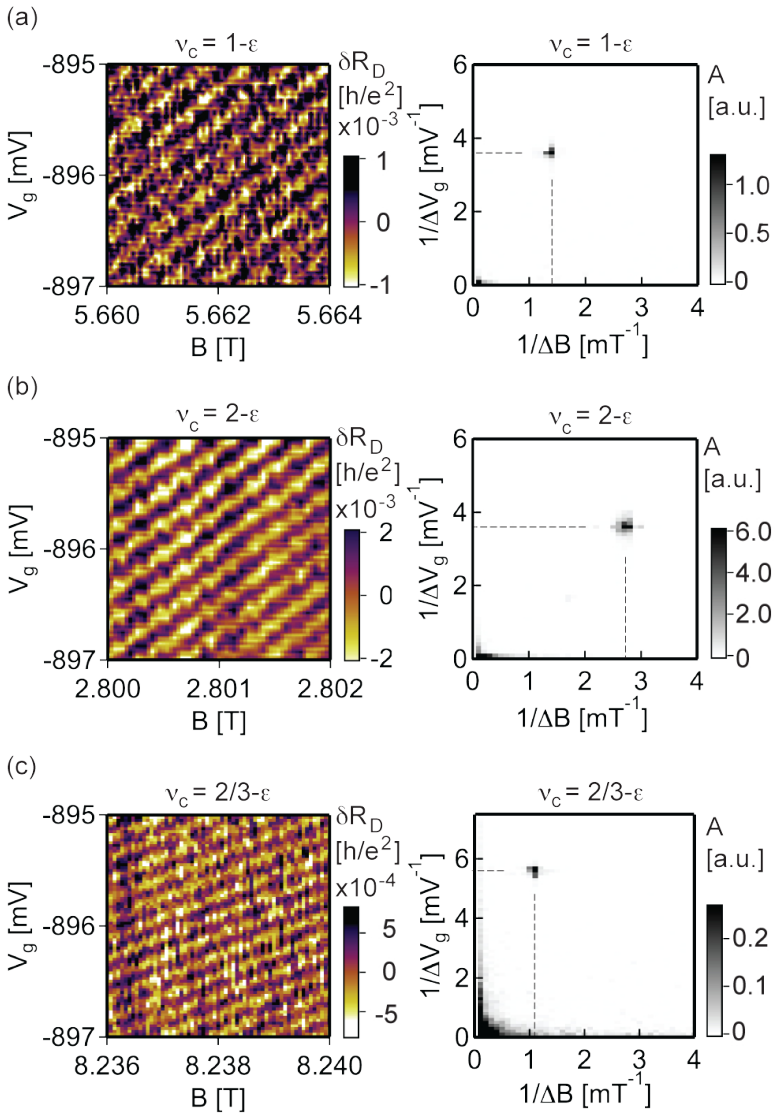

Figure 3.3: Diagonal resistance with background subtracted, $\delta R_{\rm D}$, as a function of B and $V_{\rm g}$ in 2 μm diameter antidot at (a) $\nu_{\rm c} = 1^-$, (b) $\nu_{\rm c} = 2^-$, and (c) $\nu_{\rm c} = 2/3^-$, with corresponding 2D Fourier power spectra. Dominant peaks in the power spectra are marked by dashed lines, located at (1.4 mT^{-1}, 3.6 mV^{-1}) for $\nu_{\rm c} = 1^-$, (2.7 mT^{-1}, 3.6 mV^{-1}) for $\nu_{\rm c} = 2^-$, and (1.1 mT^{-1}, 5.6 mV^{-1}) for $\nu_{\rm c} = 2/3^-$.

cases. The dominant peaks in the Fourier spectra show the expected scaling of the field period between $\nu_{\rm c} = 1^-$ and $\nu_{\rm c} = 2^-$, with peaks at 1.4 mT^{-1} at $\nu_{\rm c} = 1^-$ and 2.7 mT^{-1} at $\nu_{\rm c} = 2^-$ differing roughly by the same factor of two as discussed above. At $\nu_{\rm c} = 2/3^-$, the dominant Fourier peak is at 1.1 mT^{-1}, which is close to,

but somewhat smaller than the magnetic field frequency at $\nu_c = 1^-$. This scaling of magnetic field periods is similar to what was observed in the 1 μm device above. The position of the dominant spectral peak as a function of gate-voltage frequency, $1/\Delta V_g$, is the same for $\nu_c = 1^-$ and $\nu_c = 2^-$, in both cases 3.6 mV^{-1}, but increases to 5.6 mV^{-1} at $\nu_c = 2/3^-$.

3.5 Edges and Charges at $\nu = 2, 1,$ and $2/3$

Table 3.1: Summary of magnetic field oscillations data, for antidots with lithographic diameter D and filling factor ν_c in the constrictions connecting the antidot to the sample edges. Oscillation periods, ΔB, used to determine depletion length, d, taken to be the same for the two antidots at the same filling factor, and the number of edge channels, N.

D [μm]	ν_c	d [nm]	ΔB [mT]	N
	1	320	0.74	1
2	2	310	0.38	2
	2/3	190	0.92	1
	1	320	2.1	1
1	2	310	1.0	2
	2/3	190	2.9	1

Table 3.1 summarizes the observed oscillations as a function of magnetic field. The number of charge-carrying edges, N, at each filling factor is deduced from the magnetic field period within a Coulomb charging picture, where each edge contributes one oscillation in resistance per flux quantum. In the integer regime, this interpretation is consistent with previous experiments and data in both antidots and quantum

dots [59, 68, 71, 80], and reconciles the unphysically large effective area that would be inferred from the field period at $\nu_c = 2^-$ from a single-edge picture. We find, therefore, $N = 2$ separate charge-carrying edges bound to the antidot at $\nu_c = 2^-$. At $\nu_c = 2/3^-$, the measured period is too large to correspond to two charged edges within an analogous Coulomb picture, as the large field period would imply $d < 0$. We thus find $N = 1$ charged edge at $\nu_c = 2/3^-$.

Equation 1 was used to find a best-fit effective area enclosed by the charged edge state at each filling factor for each device. The depletion length was then found by taking an average of the best fit effective areas and constraining both devices to have the same depletion length, d, for two antidot sizes measured at the same antidot gate voltage. To calculate the depletion length from the data at $\nu_c = 2^-$, we take one flux quantum to correspond to twice the measured magnetic field period. Note that the depletion length deduced in this way is ~ 100 nm smaller at $\nu_c = 2/3^-$ than at $\nu_c = 1^-$ and $\nu_c = 2^-$. Depletion lengths calculated in the same manner at $\nu_c = 1/3^-$ are ~ 40 nm smaller than the depletion lengths found at integer filling factors [79].

Table 3.2 summarizes observed oscillations as a function of antidot gate voltage. Gate-voltage periods at $\nu_c = 1^-$ and $\nu_c = 2^-$ are the same within measurement uncertainty. The gate-voltage period at $\nu_c = 2/3^-$, is $\sim 2/3$ of this value. No features are visible in the $\nu_c = 2/3^-$ Fourier spectrum at 1/3 times the gate-voltage period at $\nu_c = 1^-$ in either device. We also do not find any change in the gate-voltage period above 100 mK, in contrast to the behavior observed in Ref. [54].

Table 3.2: Summary of gate-voltage oscillations data, for antidots with lithographic diameter D and filling factor ν_c in the constrictions. Oscillation periods, ΔV_g, and periods relative to the period at $\nu_c = 1^-$ determine the tunneling charge, e^*, as discussed in the text.

D [μm]	ν_c	ΔV_g[mV]	$\frac{\Delta V_g}{\Delta V_g^{\nu_c=1}}$
	1	0.28	$\equiv 1$
2	2	0.28	1.0
	2/3	0.18	0.64
	1	0.62	$\equiv 1$
1	2	0.62	1.0
	2/3	0.42	0.67

3.6 Discussion

Based on magnetic field and gate-voltage periods, we infer a Coulomb charging mechanism for the observed resistance oscillations. In the case of single-particle Aharonov-Bohm oscillations, one would expect a constant field period and a gate-voltage period that scales inversely with increasing applied magnetic field [70]. We do not observe this behavior in our devices. Instead, we have found that the field period scales with the number of edges in the system and the gate-voltage period is constant for integer oscillations but changes for fractional oscillations. From these observations, we conclude that Coulomb effects are the dominant mechanisms for oscillations in our system [70, 81].

Coulomb oscillations in antidots in the integer regime was considered theoretically in Ref. [70], which found that the field period scales with the number of fully trans-

mitted edges in the constrictions. We instead find oscillations on the high field side of the ν_c plateau in R_D, where the outermost edge is not fully transmitted. Similar results were reported in Ref. [59], which found a field period corresponding to $\phi_0/2$ on both sides of the $\nu = 2$ plateau. We conclude that it is number of antidot-bound edge states that determines the magnetic field period.

The picture of Coulomb oscillations gives an antidot gate-voltage period proportional to the tunneling charge,

$$\Delta V_g \sim e^*, \tag{3.2}$$

independent of the number of edges [70, 81], assuming a capacitive coupling (or lever arm) that is roughly independent of filling factor. Numerical modeling indicates that the capacitance of the antidot gate to a nearby 2DEG does not change significantly within the range of depletion lengths in Table 3.1. The insensitivity of capacitance to filling factor is also supported by the observation of equal gate-voltage periods for $\nu_c = 1^-$ and $\nu_c = 2^-$. The observed period at $\nu_c = 2/3^-$ thus strongly suggests $e^* = 2e/3$. This result is somewhat surprising in light of previous measurements of tunneling into a disorder-induced charge puddle at $\nu = 2/3$, which found $e^* = e/3$ [83]. We speculate that the smaller charging energies in the current devices, due to screening from the antidot gate, allow a quasiparticle pairing energy associated with edge reconstruction at $\nu = 2/3$ to dominate over the Coulomb energy associated with tunneling $2e/3$ rather than $e/3$. Further experiments, including on devices that allow direct charge sensing, and over a broad range of device areas, will help clarify this result.

3.7 Acknowledgements

We thank D.T. McClure, B. I. Halperin, M. Heiblum, B. Rosenow, and A. Yacoby for useful discussions, and P. Gallagher for experimental contributions. Research supported by Microsoft Project Q, the National Science Foundation (DMR-0819860), the Gordon and Betty Moore Foundation, and the Department of Energy, Office of Science. Device fabrication used Harvard's Center for Nanoscale Systems.

3.8 Epilogue

3.8.1 Theoretical Results

Theoretical results with a different interpretation of our data have very recently been published [84]. Schreier and coworkers find that an antidot in the Coulomb-dominated (CD) domain in the integer quantum Hall regime will most likely be in the Aharonov-Bohm (AB) domain in the fractional quantum Hall regime for the same device and gate voltage settings. Based on macroscopic calculations done at finite temperature, they find that the CD domain is much smaller than the AB domain in the fractional quantum Hall (FQH) regime due in large part to the reduction of charging energy by the square of the quasiparticle charge in the FQH regime. In the regime of scattering relevant to our experiments, the Coulomb domain occupies 1/35th of the total parameter space in the fractional quantum Hall regime compared with 1/3rd of the total parameter space in the integer quantum Hall regime. Within their framework, Schreier *et al.* find that the magnetic field period and gate voltage period at $\nu_c = 2/3$ are consistent with the antidot being in the AB regime. They

interpret the periods to indicate the presence of two non-interacting edges and a quasiparticle charge of $e^* = e/3$. They also propose an experiment to test the theory whereby one can tune the antidot through different regimes by changing the strength of backscattering in the constrictions. At $\nu_c = 2/3$, they find that in the regime of strong backscattering, there are four different domains determined by the ratio between the coupling between the edges of the antidot and the capacitive coupling of the antidot to the outside world. They propose that one could start in the weak backscattering regime, where the device will be in the AB regime, and tune into the strong backscattering regime by changing the qpc strength of the device. This may result in a change in the magnetic field periodicity of the device because the CD domain in the strong backscattering case is larger than the CD domain in the weak backscattering case.

3.8.2 Size Dependence of Oscillations

The size dependence of oscillations at $\nu_c = 2/3^-$ was further investigated. Oscillations at $\nu_c = 2^-, 1^-, 2/3^-$ were found in an antidot with lithographic diameter $D = 500$ nm. Within the CD picture presented in this chapter, we again find the presence of 1 edge at $\nu_c = 2/3^-$ and 2 edges at $\nu_c = 2^-$ by comparing the field periods of the oscillations at $\nu_c = 2/3^-$ and $\nu_c = 2^-$ with the field period at $\nu_c = 1^-$. We find the tunneling charge to be e at $\nu_c = 2^-$. We also find a tunneling charge of $e^* = 2e/3$ by comparing the gate period at $\nu_c = 2/3^-$ to the gate period at $\nu_c = 1^-$. The data is summarized in Tables 3.3 and 3.4.

We also investigated oscillations in an antidot with diameter D=4 μm. Oscillations

were found at $\nu_c = 1^-$ and $\nu_c = 2^-$ with the same qualitative behavior as the smaller-sized antidots but no fractional oscillations were observed. We speculate that this may be because of two reasons. First, it is possible that the temperature is comparable to the charging energy of this antidot at $\nu_c = 2/3^-$, which would make it difficult to observations. Second, if the antidot is in the AB regime in the fractional quantum Hall case, it may be difficult for the quasiparticle to maintain coherence across the circumference of the larger antidot.

Table 3.3: Magnetic Field Oscillations Data for a $D = 500\ nm$ antidot and filling factor ν_c in the constrictions connecting the antidot to the sample edges.

D [μm]	ν_c	ΔB [mT]	N
	1	5.8	1
0.5	2	3.3	2
	2/3	8.1	1

Table 3.4: Gate-Voltage Oscillations Data for a $D = 500\ nm$ antidot and filling factor ν_c in the constrictions. Oscillation periods, ΔV_g, and periods relative to the period at $\nu_c = 1^-$ determine the tunneling charge, e^*, as discussed in the text.

D [μm]	ν_c	ΔV_g[mV]	$\frac{\Delta V_g}{\Delta V_g^{\nu_c=1}}$
	1	1.4	$\equiv 1$
0.5	2	1.4	1.0
	2/3	0.91	0.63

3.8.3 Oscillations at $\nu_c = 1/3$

During the writing of this paper, we found oscillations at both $\nu_c = 2/3$ and $\nu_c = 1/3$ in GaAs with a 30 nm wide quantum well located 260 nm below the surface with density $n = 1.5 \times 10^{15}$ m^{-2} and mobility μ = 1,200 m^2/V·s measured in the dark, which will be known as the low density material. At $\nu_c = 2/3$ we find similar results to those detailed above. The magnetic field period of oscillations at $\nu_c = 2/3$ was slightly larger than the the magnetic field period of oscillations $\nu = 1$. The gate voltage period of oscillations at $\nu_c = 2/3$ was $\sim 2/3$ of the gate voltage period of oscillations $\nu = 1$

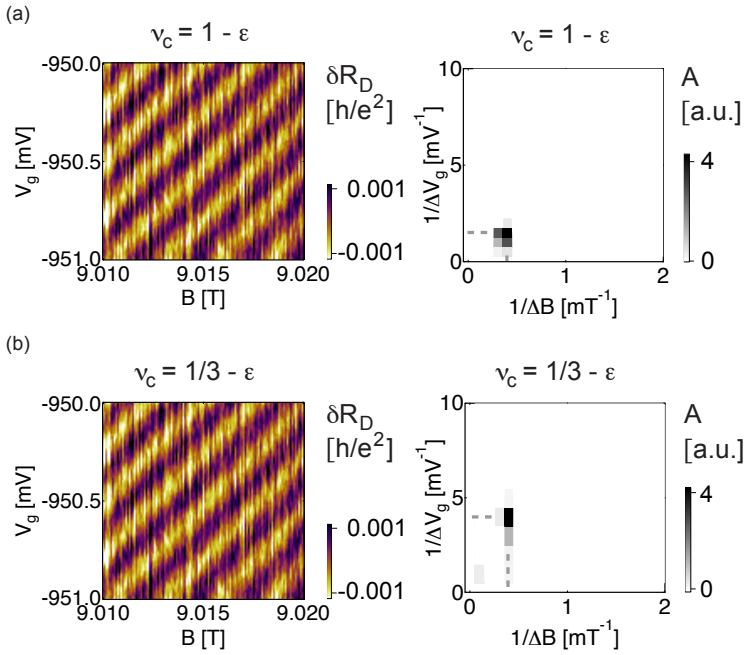

Figure 3.4: Diagonal resistance with background subtracted, δR_D, as a function of B and V_g in 1 μm diameter antidot at (a) $\nu_c = 1^-$ and (b) $\nu_c = 1/3^-$, with corresponding 2D Fourier power spectra. Dominant peaks in the power spectra are marked by dashed lines, located at (0.4 mT^{-1}, 1.3 mV^{-1}) for $\nu_c = 1^-$ and (0.36 mT^{-1}, 3.7 mV^{-1}) for $\nu_c = 1/3^-$.

We find oscillations at $\nu_c = 1/3$ in this material. Figure 3.4 shows δR_D, as a

function of both B and V_g in a 1 μm diameter antidot with 500 nm QPC's activated. Note that it was necessary to activate a different set of QPC's from the regime where we found oscillations in this device at $\nu_c = 2/3^-$ in order to find oscillations at $\nu_c = 1/3$. We find that the gate voltage period at $\nu_c = 1/3$ is 1/3 of the gate period at $\nu = 1$ suggesting that the quasiparticle charge at $\nu_c = 1/3$ is e/3, which is consistent with previous measurements of quasiparticle charge taken at $\nu = 1/3$ [60, 83, 85, 86]. We also observe that the magnetic field period at $\nu_c = 1/3$ is comparable to the magnetic field period at $\nu_c = 1$. Using the analysis detailed above, this suggests that there is 1 edge encircling the antidot at $\nu_c = 1/3$, consistent with theoretical expectations [48].

3.8.4 Dynamic Nuclear Polarization in Antidots

We found that applying a large finite bias also had effects on resistance oscillations at fractional filling factors found in an antidot device fabricated on the low density material. Applying a DC bias was observed to have different effects on oscillations at different fractions. We applied a finite DC bias of 0.5 nA using the sweeping procedure detailed in Chapter 2. Figure 3.5(a) shows R_D as a function of magnetic field near $\nu_c = 1/3$ before (red) and after (blue, black) before any bias was applied. Insets show the zoom-ins of oscillations before and after bias is applied. The arrows indicate the location where the bias was applied. Figure 3.5(b) shows the FFTs of oscillations at $\nu_c = 1/3^+$ before (red) and after (blue) applying the DC bias. There is a slight enhancement in the amplitude of the peak after applying a finite bias. Figure 3.5(c) shows the FFTs of oscillations at $\nu_c = 1/3^-$ before (red) and after (black) applying

the DC bias. In this case, we see a slight decrease in the amplitude of the peak after applying a bias.

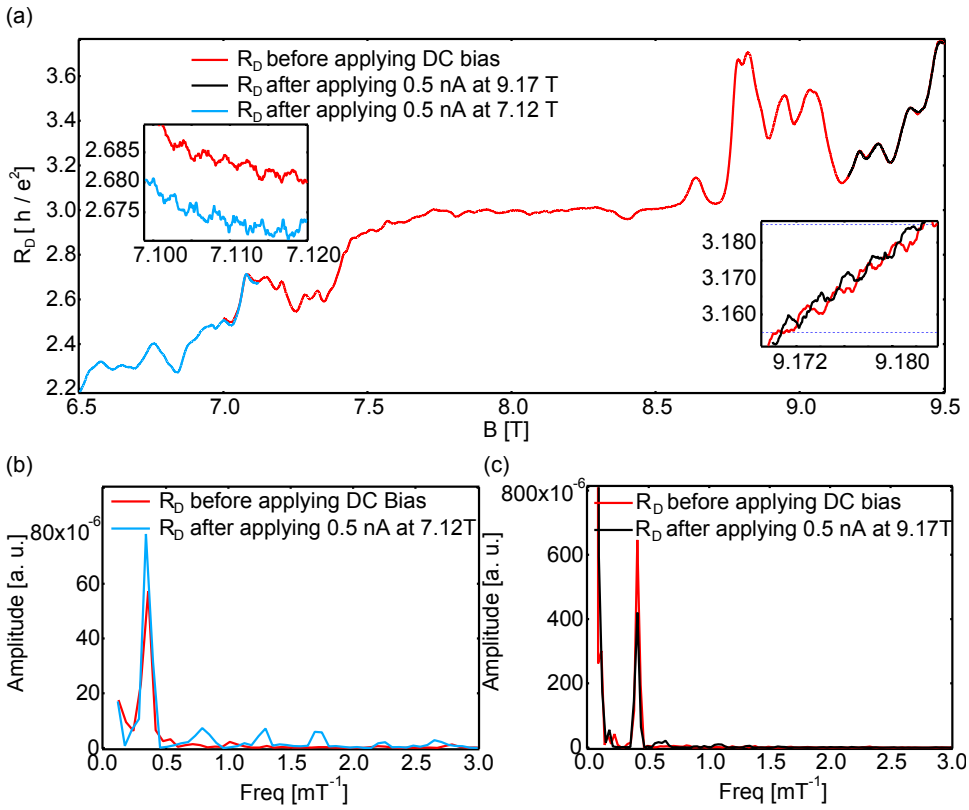

Figure 3.5: (a) R_{D} as a function of B at $\nu_{\mathrm{c}} = 1/3$. Red trace indicates R_{D} before I_{DC} has been applied. Blue trace indicates R_{D} after $I_{\mathrm{DC}} = 0.5$ nA has been applied at $B = 7.12$ T. Black trace indicates R_{D} after $I_{\mathrm{DC}} = 0.5$ nA has been applied at $B = 9.17$ T. (b) FFTs of oscillations at $\nu_{\mathrm{c}} = 1/3^{+}$ shown in inset (a) before (red) and after (blue) applying a DC bias. (c) FFTs of oscillations at $\nu_{\mathrm{c}} = 1/3^{-}$ shown in insets in (a) before (red) and after (black) applying a DC bias.

The effect of applying a DC bias, however, is much greater on the oscillations at $\nu_{\mathrm{c}} = 2/3$. Figure 3.6(a) shows R_{D} as a function of magnetic field before (red) and after (blue, black) the DC bias is applied. The device resistance was monitored as the field was swept both upward (black) and downward (blue) after applying a DC bias to eliminate the possibility of spurious effects based on magnetic field direction. Figure 3.6(b) shows the corresponding FFT's of the oscillations. The amplitude of

the oscillations observed after applying the DC bias is reduced by more than a factor of 10 compared with the amplitude of oscillations observed before any DC bias was applied.

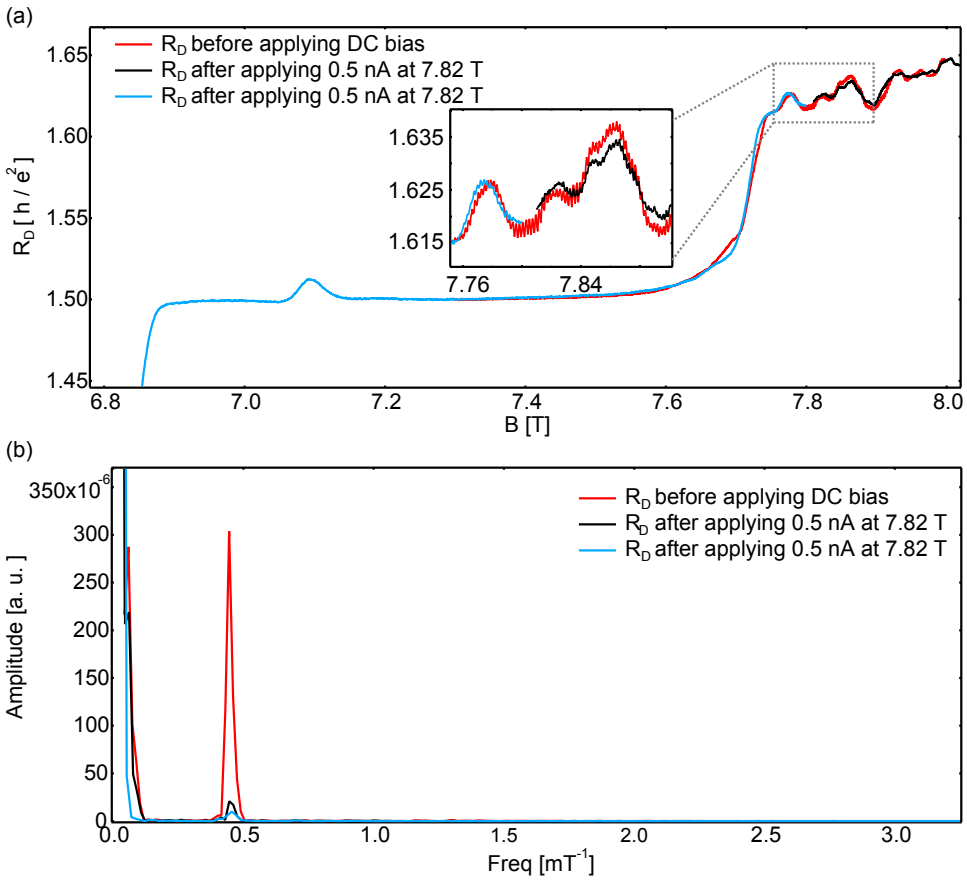

Figure 3.6: (a) R_{D} as a function of B at $\nu_{\mathrm{c}} = 2/3$. Red trace indicates R_{D} before I_{DC} has been applied. Black trace indicates R_{D} after $I_{\mathrm{DC}} = 0.5$ nA has been applied at $B = 7.8$ T. Blue trace indicates R_{D} after $I_{\mathrm{DC}} = 0.5$ nA has been applied at $B = 7.8$ T. (b) FFT of oscillations at $\nu_{\mathrm{c}} = 2/3^{-}$ shown in inset in (a) before (red) and after (blue, black) applying a DC bias. Note the reduction in amplitude of the FFT after application of DC bias.

We speculate that these effects are related to the dynamic nuclear polarization detailed in Chapter 2. It is possible that dynamic nuclear polarization does not have a large effect at $\nu_{\mathrm{c}} = 1/3^{-}$ because the quasiparticles are spin-polarized at $\nu = 1/3$, which means that any nuclei-flipping processes would be strongly suppressed since

they do not conserve angular momentum. Indeed, in the experiment described in Chapter 2, we do not observe any effects of applying a DC bias at $\nu_c = 1/3^-$. At $\nu_c = 1/3^+$, one could argue that domains of $\nu = 2/5$ could allow for spin flips but we do not see the presence of a $\nu = 2/5$ plateau. Hence, there are no possible angular-momentum conserving mechanisms to polarize nuclei.

At $\nu_c = 2/3^-$, on the other hand, there are likely to be domains of unpolarized and polarized $\nu = 2/3$ [37]. Quasiparticles, then, can polarize nuclei via the contact hyperfine interaction. There are two possible types of tunneling that are occurring: CD or AB. In both cases, tunneling will be blocked if the spin of the tunneling quasiparticle is flipped. In the CD case, if all tunneling is occurring via the spin-up edge as suggested in Ref. [87] and we flip the quasiparticle spin, it will not be able to tunnel onto the spin-up edge on the antidot. In the AB case, flipping the quasiparticle spin does not maintain coherence and, hence, will not result in oscillations.

3.8.5 Nonlinear Transport Data

We also performed measurements at low finite bias in the 1 μm antidot device on the two different materials mentioned in this section. Figure 3.7 shows R_D as a function of applied DC bias, V_{SD}, and B in the antidot device fabricated on the higher density material with the 500 nm QPC's activated. All gate voltage settings were kept constant through all of the plots shown in Fig. 3.7. Note that the energy scale at $\nu_c = 2^-$ and $\nu_c = 1^-$ are similar at about 60 μeV. The data at $\nu_c = 2^-$ looks especially reminiscent of Coulomb blockade diamonds. No periodic behavior is seen at higher biases. The energy scale at $\nu_c = 2/3^-$ is much smaller, only about 20 μeV.

Going to higher DC biases results in a decrease in the visibility of the oscillations and a large change in the resistance of the device. These effects were discussed in the previous section.

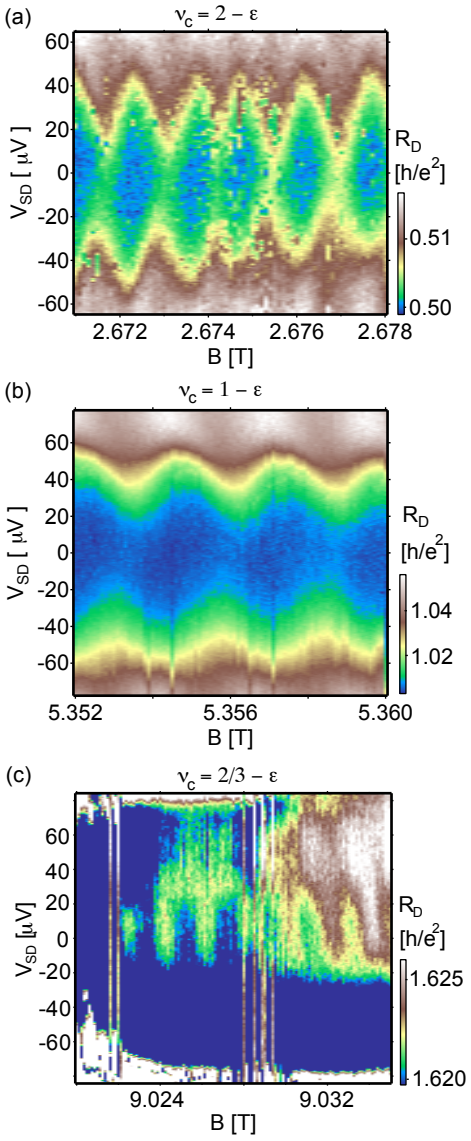

Figure 3.7: (a) R_{D} as a function of B and V_{SD} at $\nu_{\mathrm{c}} = 2^{-}$. (b) R_{D} as a function of B and V_{SD} at $\nu_{\mathrm{c}} = 1^{-}$. (c) R_{D} as a function of B and V_{SD} at $\nu_{\mathrm{c}} = 2/3^{-}$.

Figure 3.8(a) shows R_{D} as a function of applied DC bias, V_{SD}, and B in the antidot device fabricated on the low density material with the 750 nm QPC's activated. We

found that the effects of applying a DC bias were mitigated when using a larger constriction size. Going to larger biases than the range shown, however, still resulted in a large decrease in the visibility of oscillations. The energy scale of the oscillations appears to be about 20 μeV. We also note that the oscillations also seem to be periodic in the applied DC bias; this periodicity is clearly seen in Fig. 3.8(b), which shows δR_{D} as a function of applied DC bias, V_{SD}, and B. In Fabry-Perot interferometers, this periodicity in bias was shown in the integer quantum Hall regime to be indicative of AB behavior [88]. Roughly, this periodicity in bias occurs because by changing the energy of the system we change the wavevector of the interfering particle. The wavevector of the interfering particle can be related to the area of the enclosing loop so by changing the energy we change the flux through the loop [89]. We speculate that the periodicity in DC bias observed in the fractional quantum Hall regime in an antidot is indicative of AB behavior.

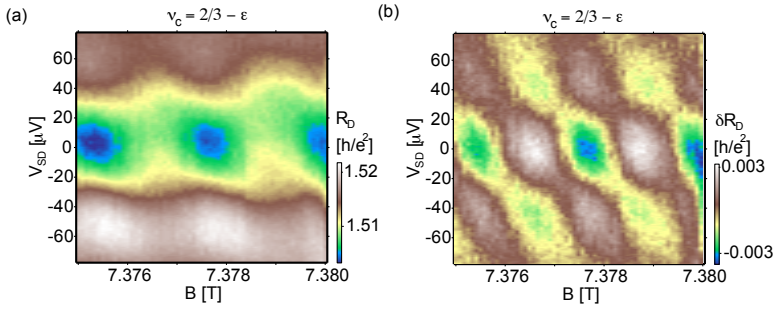

Figure 3.8: (a) R_{D} as a function of B and V_{SD} at $\nu_{\mathrm{c}} = 2/3^{-}$. (b) δR_{D} (R_{D} with a smooth background subtracted) as a function of B and V_{SD} at $\nu_{\mathrm{c}} = 2/3^{-}$.

3.8.6 Oscillations at $\nu = 4/3$

We found oscillations as a function of magnetic field and antidot gate voltage in the vicinity of $\nu_{\mathrm{c}} = 4/3$. Figure 3.9 shows R_{H} and R_{D} as a function of B at fixed gate

voltages in the 1 μm diameter antidot on the low density material with the 750 nm qpcs activated. Insets show detailed views of periodic oscillations in $R_{\rm D}$, with periods $\Delta B = 2.4$ mT for $\nu_{\rm c} = 4/3^-$, and $\Delta B = 2.4$ mT for $\nu_{\rm c} = 2/3^-$. The period of 2.4 mT at $\nu_{\rm c} = 2/3^-$ corresponds to $\phi_0 = h/e$ through an area of 1.7 μm^2, larger than the lithographic area of the antidot, $A = 0.8$ μm^2. We attribute the larger area to the finite depletion length of the antidot top gate, as discussed above.

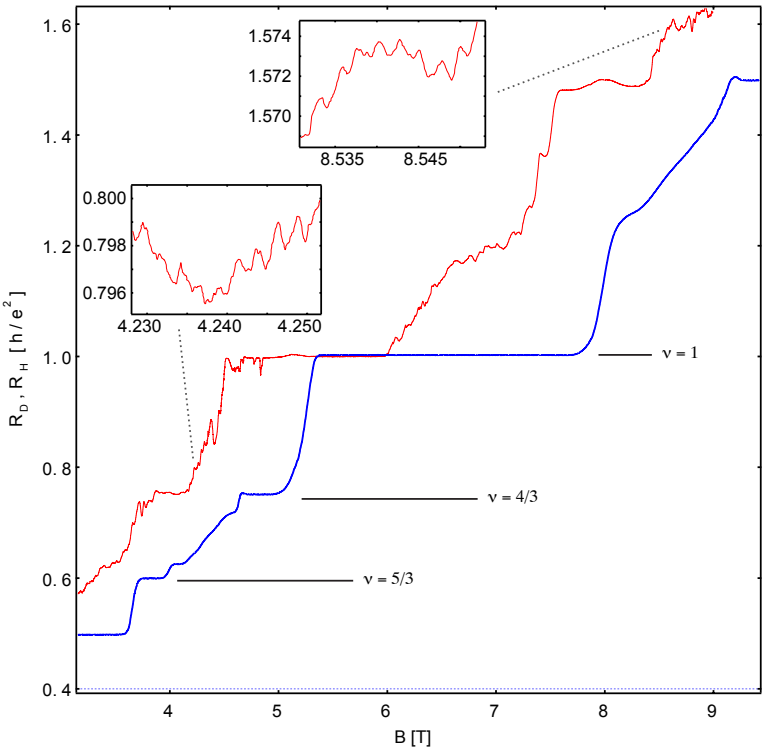

Figure 3.9: Diagonal resistance, $R_{\rm D}$ (red), and bulk Hall resistance, $R_{\rm H}$ (blue), as a function of perpendicular magnetic field, B, in the 1 μm diameter antidot with the 750 nm qpcs activated. Insets show regions of oscillations at $\nu_{\rm c} = 4/3^-$ and $\nu_{\rm c} = 2/3^-$.

Figure 3.10 shows $R_{\rm D}$ with a smooth background subtracted, denoted $\delta R_{\rm D}$, as a function of both B and $V_{\rm g}$ at $\nu_{\rm c} = 2/3^-$ and $\nu_{\rm c} = 4/3^-$ along with corresponding two-dimensional (2D) Fourier power spectra. The dominant peaks in the Fourier spectra show the same magnetic field period at $\nu_{\rm c} = 2/3^-$ and $\nu_{\rm c} = 4/3^-$, with peaks

at 0.4 mT^{-1} at both filling factors. The position of the dominant spectral peak as a function of gate-voltage frequency differs by a factor of 2: $1/\Delta V_\mathrm{g}$ is 1.25 mV^{-1} at $\nu_\mathrm{c} = 4/3^-$ but increases to 2.43 mV^{-1} at $\nu_\mathrm{c} = 2/3^-$.

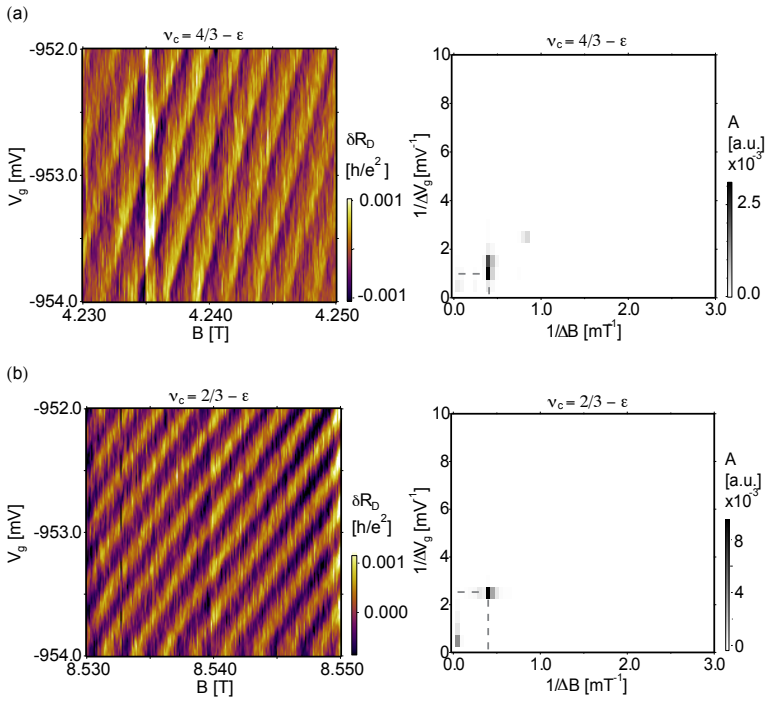

Figure 3.10: Diagonal resistance with background subtracted, δR_D, as a function of B and V_g in 1 μm diameter antidot at (a) $\nu_\mathrm{c} = 2/3^-$ and (b) $\nu_\mathrm{c} = 4/3^-$, with corresponding 2D Fourier power spectra. Dominant peaks in the power spectra are marked by dashed lines, located at (0.4 mT^{-1}, 1.25 mV^{-1}) for $\nu_\mathrm{c} = 4/3^-$ and (0.4 mT^{-1}, 2.43 mV^{-1}) for $\nu_\mathrm{c} = 2/3^-$.

If we assume that we are in the CD regime, the magnetic field period and gate period at $\nu_\mathrm{c} = 4/3^-$ are fairly surprising. From the magnetic field period, one would have to conclude that the same number of edges are present at both filling factors, which could be expected theoretically if the edges at $\nu_\mathrm{c} = 2/3^-$ have not reconstructed around the antidot [50]. We would also have to conclude that the tunneling charge at $\nu_\mathrm{c} = 4/3^-$ is twice the tunneling charge at $\nu_\mathrm{c} = 2/3^-$, which would be unexpected. It is reasonable, then, to consider the possibility that we are in the AB regime as

conjectured by Schreier *et al.* [84]. Within this theoretical framework, the expected magnetic field periods would be the same at both $\nu_c = 4/3^-$ and $\nu_c = 2/3^-$. The gate voltage period ratio between the two filling factors would be given by the ratio of the magnetic fields at which they occur. The gate voltage period ratio between $\nu_c = 4/3^-$ and $\nu_c = 2/3^-$ we observe is 2, which is consistent with the antidot being in the AB domain. Unfortunately, we could not find strong oscillations at integer filling factors in the constrictions, which would help confirm this interpretation.

Chapter 4

Fractional Quantum Hall Effect in Bilayer Graphene

A. Kou, B. E. Feldman, A. J. Levin, A. Yacoby

Department of Physics, Harvard University, Cambridge, Massachusetts 02138, USA

K. Watanabe, T. Taniguchi

National Institute for Materials Science, 1-1 Namiki, Tsukuba 305-0044, Japan

4.1 Introduction

The nature of fractional quantum Hall (FQH) states is determined by the interplay between the Coulomb interaction and the symmetries of the system. The unique combination of spin, valley, and orbital degeneracies in bilayer graphene is predicted to produce novel and tunable FQH ground states [90–96]. Here we present local electronic compressibility measurements of the FQH effect in the lowest Landau level

(LL) of bilayer graphene. We observe incompressible FQH states at filling factors $\nu = -10/3, -4/3, 2/3$, and $8/3$, with hints of additional states appearing at $\nu = -17/5, -7/5, 3/5$ and $13/5$. This sequence of states breaks particle-hole symmetry and instead obeys a $\nu \rightarrow \nu + 2$ symmetry, which highlights the importance of the orbital degeneracy for many-body states in bilayer graphene.

4.1.1 Quantum Hall Effect in Bilayer Graphene

The charge carriers in bilayer graphene obey an electron-hole symmetric dispersion at zero magnetic field. Application of a perpendicular magnetic field B breaks this dispersion into energy bands known as LLs. In addition to the standard spin and valley degeneracy found in monolayer graphene, the $N = 0$ and $N = 1$ orbital states in bilayer graphene are also degenerate and occur at zero energy [97]. This results in a sequence of single-particle quantum Hall states at $\nu = 4Me^2/h$, where M is a nonzero integer [98].

When the disorder is sufficiently low, the eightfold degeneracy of the lowest LL is lifted by electron-electron interactions, which results in quantum Hall states at all integer filling factors [99, 100]. The nature of these broken-symmetry states has been studied extensively both experimentally and theoretically, with particular attention given to the insulating $\nu = 0$ state. The filling sequence was initially predicted to first maximize spin polarization, then valley ordering, and finally orbital polarization [101]. It has been shown, however, that the ground state at $\nu = 0$ in bilayer graphene in certain samples is actually a canted antiferromagnet, which maximizes neither spin nor valley polarization [105, 106]. Multiple groups have also been able to induce

transitions between different spin and valley orders of the ground states using external electric and magnetic fields [102–105]. It is clear that the interplay between Zeeman energy, layer asymmetry, valley anisotropy terms, and SU(4)-symmetric electron-electron interactions produces a rich phase diagram in bilayer graphene not found in any other system.

4.1.2 Fractional Quantum Hall Effect in Bilayer Graphene

Knowledge of the ground state at integer filling factors is especially important for investigating the physics of partially filled LLs, where in exceptionally clean samples, the charge carriers condense into FQH states. The above-mentioned degrees of freedom as well as the strong screening of the Coulomb interaction in bilayer graphene are expected to result in an interesting sequence of FQH states in the lowest LL [91–96]. Indeed, partial breaking of the SU(4) symmetry in monolayer graphene has already resulted in sequences of FQH states with multiple missing fractions [107–111]. Phase transitions between FQH states with different polarizations have also been observed in monolayer graphene [112].

Experimental observation of FQH states, however, has proven to be difficult in bilayer graphene. Hints of a $\nu = 1/3$ state were first reported in transport by Bao and coworkers [113]. Very recently, Ki and coworkers observed robust FQH states at $\nu = -1/2$ and $\nu = -4/3$ in a current-annealed suspended bilayer sample [114]. Here, we report local compressibility measurements of a bilayer graphene device fabricated on hexagonal-Boron Nitride (h-BN), performed using a scanning single-electron transistor (SET). Our technique allows us to directly probe the thermodynamic properties

of the bulk of the sample [115, 116]. We measure the local chemical potential μ and the local inverse compressibility $d\mu/dn$ by changing the carrier density n with a proximal graphite gate located 7.5 nm from the graphene and monitoring the resulting change in SET current. An optical image of the contacted device is shown in Fig. 4.1(a).

4.2 Measurements

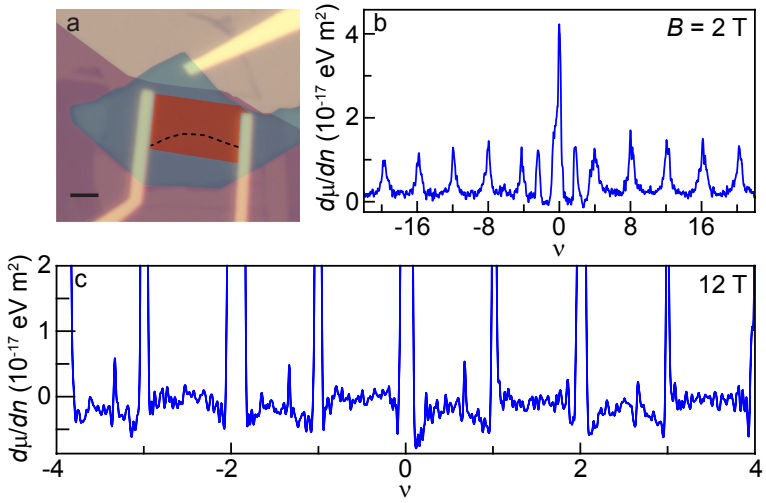

Figure 4.1: (a) Optical image of the device with colored overlays showing the graphite (blue), boron nitride (purple), and monolayer-bilayer graphene hybrid (red). The black dashed line marks the interface between monolayer and bilayer. The scale bar is 2 μm. (b) and (c) Inverse compressibility $d\mu/dn$ as a function of filling factor ν at magnetic field $B = 2$ T and 12 T, respectively.

Figure 4.1(b) shows a measurement of the inverse compressibility as a function of filling factor at $B = 2$ T. Incompressible features are present at all nonzero multiples of $\nu = 4$, indicating that we are measuring bilayer graphene. The full width at half maximum of the $\nu = 4$ peak provides a measure of the disorder in the system and is on the order of 10^{10} cm^{-2}, similar to that observed in suspended bilayers [99, 117].

Broken-symmetry states at $\nu = 0$ and ± 2 are also visible at $B = 2$ T, which further indicates the cleanliness of the sample. Most interesting, however, is the appearance of additional incompressible peaks at $B = 12$ T, shown in Fig. 4.1(c). At this field, all of the broken-symmetry states between $\nu = \pm 4$ have fully developed. In addition, we observe incompressible features at $\nu = -10/3, -4/3, 2/3$, and $8/3$, suggesting the presence of FQH states.

To invetigate the origin of the incompressible peaks, we measure the inverse compressibility as a function of filling factor and magnetic field. Figures 4.2(a) and 4.2(b) show the behavior for $-4 < \nu < 0$ and $0 < \nu < 4$, respectively. Quantum Hall states appear as vertical features when plotted in this form, while localized states, which occur at a constant density offset from their parent states, curve as the magnetic field is changed [111, 118]. We can then unambiguously identify the features at $\nu = -10/3, -4/3, 2/3$, and $8/3$ as FQH states. The FQH states closer to the charge neutrality point are more incompressible than those at higher filling factors, and they persist to fairly low magnetic fields, with the last hints disappearing around 6 T. At $B > 10$ T, we also see evidence of developing states at $\nu = -17/5, -7/5, 3/5$, and $13/5$.

Averaging the inverse compressibility over a range of magnetic fields reduces the fluctuations created by localized states and clarifies the underlying behavior. Figure 4.2(c) shows the average inverse compressibility from $B = 9.9$ to 11.9 T, which clearly shows the FQH states identified above. Figure 4.2(c) also reveals that the background inverse compressibility is markedly lower between the integer filling factors where we observe the FQH states. This correlation is consistent with previous

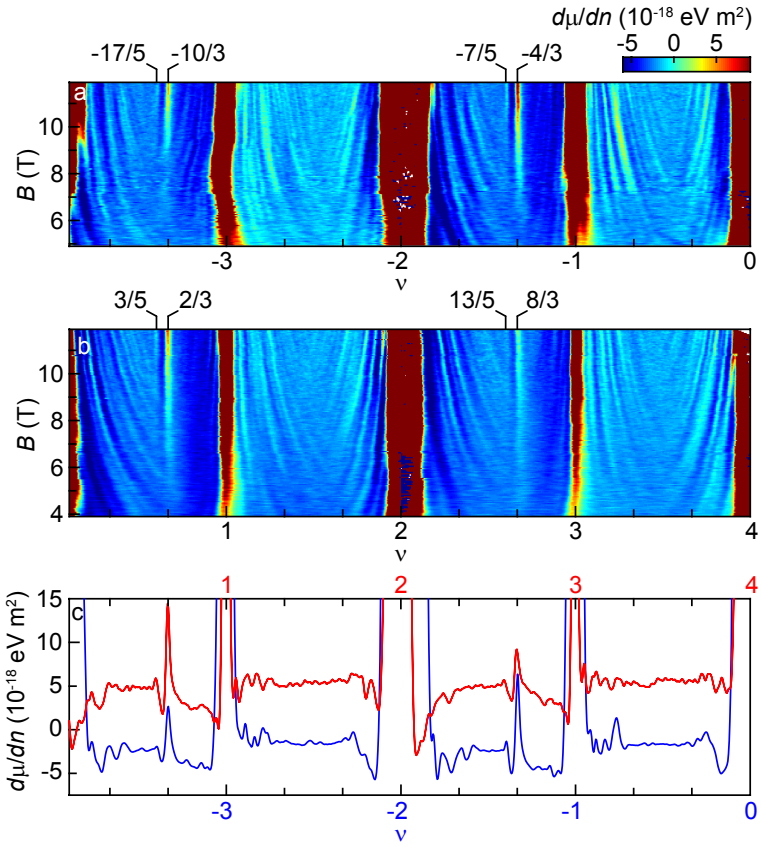

Figure 4.2: (a) and (b) Inverse compressibility as a function of filling factor and magnetic field. The color scales are the same in both panels. (c) Average inverse compressibility between $B = 9.9$ and 11.9 T as a function of filling factor. The red curve (electron side) is offset by $7\text{x}10^{-18}$ eV m^2 for clarity.

experiments where a negative background compressibility was attributed to Coulomb interactions between charge carriers [119]. We also note that the background inverse compressibility in higher LLs where no FQH states were observed was much higher than in the lowest LL.

Interestingly, the sequence of FQH states that we observe does not obey particle-hole symmetry but rather seems to follow a $\nu \rightarrow \nu + 2$ symmetry. This indicates that the orbital degeneracy uniquely present in bilayer graphene is playing an important role in determining the sequence of observed fractions. Recent theoretical work on the FQH effect in the lowest LL has predicted the presence of FQH states with a $\nu \rightarrow \nu + 2$ symmetry in bilayer graphene based on a model that incorporates the strong screening and LL mixing present in the lowest LL of bilayer graphene [96]. We do not see any fractions between $\nu = -3$ and -2 nor between $\nu = 1$ and 2 nor their $\nu + 2$ symmetric counterparts. At these filling factors, one might expect to have a filled $N = 0$ LL and be partially filling an $N = 1$ LL. The absence of states in these ranges suggests a difference between partial filling when both the $N = 0$ and $N = 1$ LLs are empty and partial filling of the $N = 1$ LL when the $N = 0$ LL is full. The increased LL mixing present when the $N = 0$ LL is full [120] may be weakening the strength of FQH states in the $N = 1$ LL.

Our observed FQH sequence also suggests possible orbital polarization of the FQH states. The FQH states we observe at $\nu = 2p + 2/3$, where $p = -1, 0$, or 1, could be singlet states of $N = 0$ and $N = 1$ orbitals, or could arise from a 2/3 state with full orbital polarization. The next strongest FQH states we observe occur at $\nu = 2p+3/5$, which must have some finite orbital polarization. It is worthwhile to note that the

strongest FQH states at multiples of $\nu = 1/5$ do not have even numerators, in contrast with recent theoretical predictions [96].

The strongest FQH states that we observe are different from those seen in previous experiments on bilayer graphene, which may point to different patterns of symmetry-breaking in the different systems. Ki and coworkers observed FQH states at $\nu = -4/3$, and $-1/2$, with hints of an additional feature at $\nu = -8/5$ [114]; the only FQH state that we also observe is $\nu = -4/3$. It is also possible that the effective interactions present in the two samples may be different due to differences in screening between a suspended bilayer and a bilayer on a substrate. The fact that different sample preparations result in different FQH states is a sign of the theoretically predicted tunability of the FQH effect in bilayer graphene [91, 93, 95]. We can contrast this with sequences of FQH states found in monolayer graphene, where both suspended samples and samples on substrates have produced the similar sequences of FQH states [107–111, 123]. It appears possible to experimentally tune not only between FQH states with different polarizations of the underlying degrees of freedom but also the relative strengths of various incompressible FQH states. Future experiments in which a perpendicular electric field and/or a parallel magnetic field are applied to the sample will provide insight into the conditions under which different FQH states are favored.

We can integrate the inverse compressibility as a function of density to obtain the energy cost of adding an electron to the system, as discussed in ref. [111]. This quantity must be divided by the quasiparticle charge associated with each state to determine the corresponding energy gap Δ_ν. The most likely quasiparticle charge for states at multiples of $\nu = 1/3$ is $e/3$, but the nature of the FQH states in bilayer

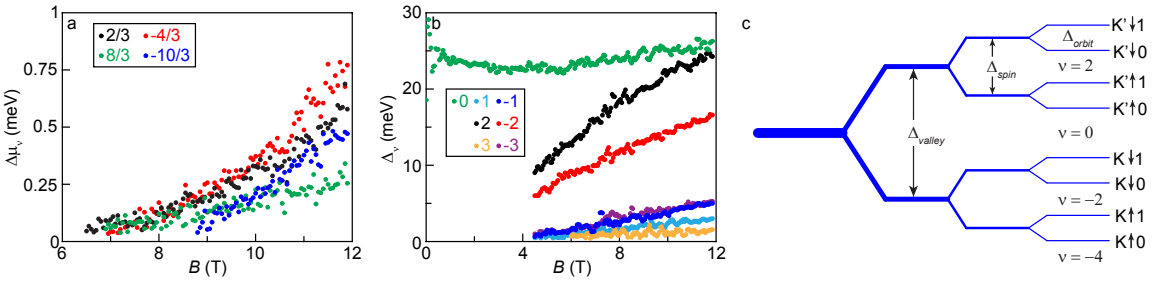

Figure 4.3: (a) Steps in chemical potential of the fractional quantum Hall (FQH) states as a function of magnetic field. (b) Energy gaps of the integer broken-symmetry states in the lowest Landau level (LL). (c) Schematic diagram showing the order of symmetry breaking in the sample.

graphene is not yet fully understood, so we plot the extracted steps in chemical potential $\Delta\mu_\nu$ in Fig. 4.3(a). For $\nu = -4/3$ and $\nu = 2/3$, $\Delta\mu_\nu$ is about 0.75 and 0.6 meV, respectively, at $B = 12$ T. Assuming a quasiparticle charge of $e/3$, the energy gap we find at $\nu = -4/3$ is comparable with, if somewhat larger than, that found in ref. [114] at similar magnetic fields. The gaps of FQH states farther away from charge neutrality are smaller; $\Delta\mu_{-10/3}$ and $\Delta\mu_{8/3}$ are only about 0.5 and 0.3 meV at $B = 12$ T. All of the extracted gaps appear to scale linearly with B, but a $\sqrt{B}$-dependence may also fit the gaps at $\nu = 8/3$ and $\nu = -10/3$. Previous measurements of broken-symmetry integer states in suspended bilayers also found a linear-B dependence of the gaps, which was attributed to LL mixing [117, 121].

The energy gaps of the integer filling factors $|\nu| < 4$ are shown in Fig. 4.3(b). All of the gaps scale approximately linearly with B, except for $\nu = 0$, which is fairly constant around 23-25 meV over almost the full range in magnetic field. Below 4 T, the gap dips slightly before increasing again at $B = 0$ T. The size of the gap and its persistence to zero field lead us to conclude that the ground state at $\nu = 0$ is layer-polarized. If we assume that the $\nu \to \nu + 2$ symmetry arises from the orbital degree of freedom, we can fully determine the sequence of symmetry-breaking in the

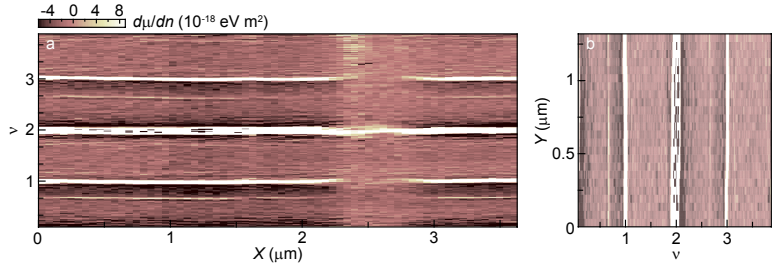

Figure 4.4: Inverse compressibility as a function of filling factor and position X (a) and Y (b). The sequence of FQH states does not vary with position.

sample: valley polarization is first maximized, then spin polarization, and finally orbital polarization, as illustrated in Fig. 4.3(c). The large valley polarization in our sample relative to other bilayer devices may be caused by interactions with the substrate. A large band gap has been observed in a monolayer graphene sample on h-BN with a proximal graphite gate, which was attributed to the breaking of sublattice symmetry by h-BN [123]. It is also possible that the difference in distance between the top layer to the graphite gate and the bottom layer to the graphite gate is creating a potential difference in the two layers [122], or that the different environments experienced by each layer play a role. Even if the $\nu = 0$ gap is caused by single-particle effects, its constancy over our entire field range is somewhat surprising because both the potential difference between the layers and the Coulomb energy are expected to contribute to the gap [124].

All of the measurements described above were performed at a single location on the sample. Local measurement allows us to find the cleanest regions and study the properties of FQH states in those areas. In addition, the local nature of our probe allows us to in effect measure multiple independent samples by measuring at different locations. Figure 4.4 shows linescans of inverse compressibility as a function of

filling factor and position. The net level of doping remains fairly constant over the entire range of the spatial scans, but there are fluctuations in the strengths of the broken-symmetry and FQH states, likely due to differences in the amount of local disorder. Despite these fluctuations, the overarching pattern of FQH states is consistent across the entire sample, and also did not change with current annealing. The electron-hole asymmetric sequence of FQH states can therefore be attributed to the intrinsic properties of bilayer graphene, rather than disorder. The observation of an unconventional sequence of FQH states in bilayer graphene indicates the importance of its underlying symmetries and opens new avenues for exploring the nature and tunability of the FQH effect.

4.3 Methods

Graphite was mechanically exfoliated onto an O_2 plasma-cleaned doped Si wafer capped with 285 nm of SiO_2. Suitable graphite pieces were found using a combination of optical microscopy and atomic force microscopy (AFM). A 7.5 nm thick piece of hexagonal-boron nitride was then transferred onto the graphite using the process detailed in ref. [123]. A hybrid monolayer-bilayer graphene flake was then transferred onto the hexagonal-boron nitride using the same method. Contacts were defined to the graphene and graphite using electron-beam lithography before thermal evaporation of Cr/Au (1 nm/85 nm) contacts, which was then lifted off in warm acetone. The sample was cleaned in a mixture of Ar/H_2 at 350 °C before each transfer step and after liftoff of contacts. The sample was further cleaned using an AFM tip. Measurements were made in a ^{3}He cryostat at approximately 450 mK. The sample was

cleaned in the cryostat using current annealing. The sample measures 8 μm from contact to contact and is 4 μm wide. All measurements presented here were made on the bilayer side of the flake.

To fabricate the scanning SET tip, a fiber puller was used to make a conical quartz tip. Al leads (16 nm) were evaporated onto either side of the quartz rod, and following an oxidation step, 7 nm of additional Al was evaporated onto the tip to create the island of the SET. The diameter of the SET is approximately 100 nm, and it was held 50-100 nm above the graphene flake during measurements. Compressibility measurements were performed using AC and DC techniques similar to those described in refs. [111,117]. The SET serves as a sensitive measure of the change in electrostatic potential $\delta\phi$, which is related to the chemical potential of the graphene flake by $\delta\mu = -e\delta\phi$ when the system is in equilibrium. In the AC scheme used to measure $d\mu/dn$, an AC voltage is applied to the graphite gate to weakly modulate the carrier density of the flake, and the corresponding changes in SET current are converted to chemical potential by normalizing the signal with that of a small AC bias applied directly to the sample. For DC measurements, a feedback system was used to maintain the SET current at a fixed value by changing the tip-sample bias. The corresponding change in sample voltage provides a direct measure of $\mu(n)$.

4.4 Acknowledgements

We thank B. I. Halperin and D. A. Abanin for useful discussions, and Javier D. Sanchez-Yamagishi for assisting in device fabrication. This work is supported by the U.S. Department of Energy, Office of Basic Energy Sciences, Division of Materials

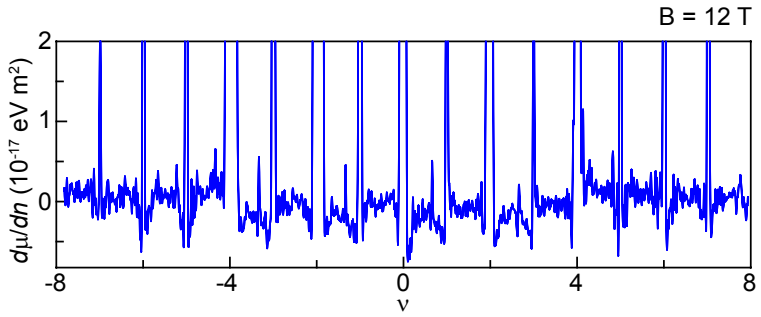

Figure 4.5: Inverse compressibility over a larger range in filling factor showing the lowest LL has more negative background compressibility than higher LLs.

Sciences and Engineering, under award no. DE-SC0001819. This work was performed in part at the Center for Nanoscale Systems at Harvard University.

4.5 Further Measurements

4.5.1 Higher Landau levels in bilayer graphene

Figure 4.5 shows the inverse compressibility as a function of filling factor for $-8 < \nu < 8$. Despite theoretical predictions of robust FQH states in the $N = 2$ LL and experimental hints in other samples [105], we do not observe any FQH states between $|\nu| = 4$ and 8. The background inverse compressibility at $4 < |\nu| < 8$ is considerably higher than at $0 < |\nu| < 4$, which is consistent with lower background compressibility corresponding to Coulomb interactions between quasiparticles, as discussed in the main text.

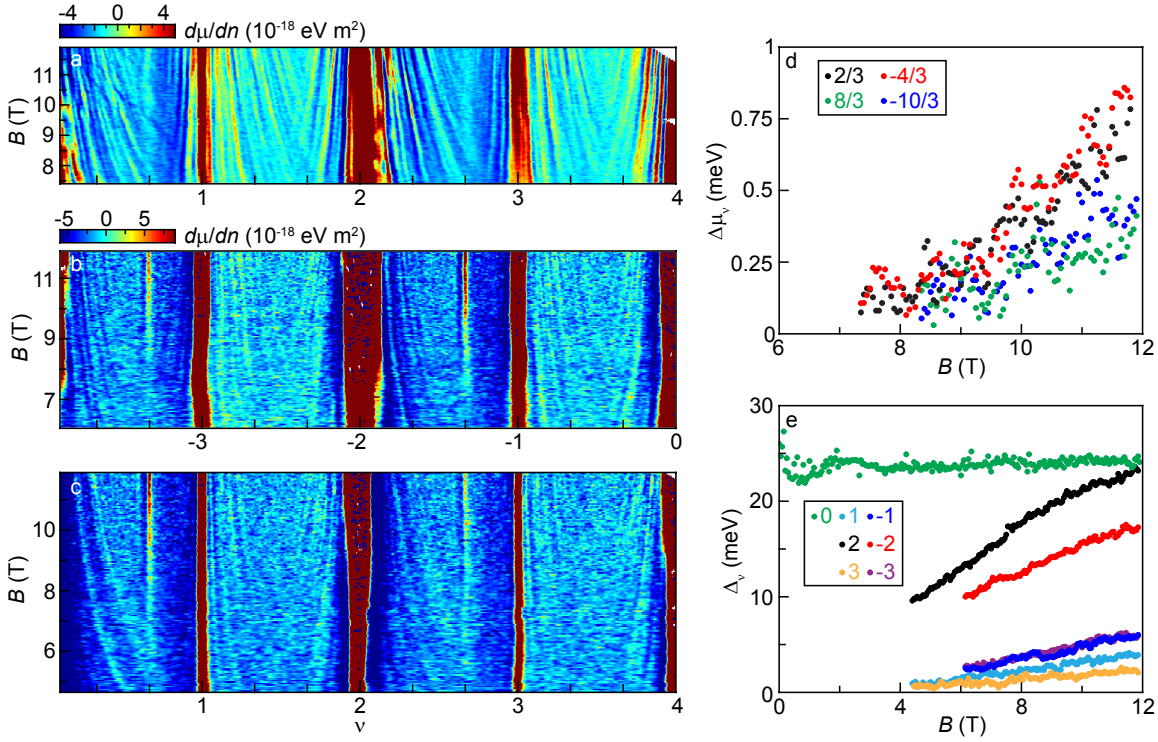

Figure 4.6: (a) Inverse compressibility as a function of filling factor and magnetic field after annealing to a source-drain voltage $V_{sd} = 4$ V. Weak incompressible peaks are visible at $\nu = 2/3$ and 8/3. (b) and (c) Inverse compressibility as a function of filling factor and magnetic field after annealing to $V_{sd} = 8$ V. The FQH states become sharper and more incompressible, and they persist to lower magnetic field. (d) Steps in chemical potential of the FQH states after annealing to 8 V. (e) Energy gaps of the integer quantum Hall states after annealing to 8 V.

4.5.2 Effects of current annealing

The data presented in the main text were taken after multiple current anneals, with a maximum source-drain voltage $V_{sd} = 10$ V. Figure 4.6 shows the progression of the behavior before and after current annealing. Prior to current annealing the sample, we observed all the integer broken-symmetry states between $\nu = \pm 4$, but no FQH states were apparent. After current annealing to 4 V, we observed hints of incompressible states at $\nu = 2/3$ and $\nu = 8/3$ [Fig 4.6(a)]. These states became more robust after annealing to 8 V [Figs. 4.6(b)-(d)] and additional FQH states appeared at $\nu = -4/3$ and $-10/3$. Throughout all current annealing steps, the sequence of incompressible FQH states did not change; current annealing appears to only increase their strength. It is worthwhile to note that the steps in chemical potential were slightly larger for $\nu = 2/3$ and $8/3$ after annealing to only 8 V than the data presented in Fig. 4.3(a).

4.5.3 Conversion of gate voltage to filling factor with large geometric capacitance

The proximity of the graphite gate resulted in a large geometric capacitance, C_G, to the sample, causing the total capacitance, C_T, to depend strongly on the compressibility of the sample. Incompressible states dramatically alter C_T because quantum capacitance dominates over geometric capacitance in this regime. Figure 4.7 shows the compressibility as a function of back-gate voltage, V_{bg}, and the very wide integer quantum Hall states clearly demonstrate the filling-factor dependent change in the total capacitance.

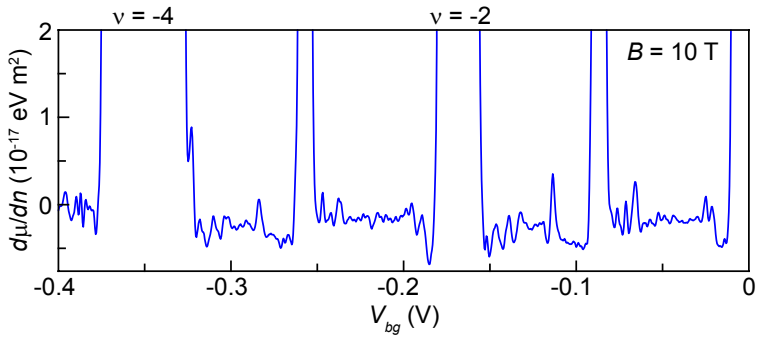

Figure 4.7: Inverse compressibility as a function of back gate voltage V_{bg}. For incompressible states, the quantum capacitance dominates over geometric capacitance, leading to very broad incompressible peaks, particularly at $\nu = -4$ and -2. The spacing between integer quantum Hall states also varies due to differences in background compressibility.

In order to assign filling factor, we use the distance between $\nu = 2/3$ and 1 to find C_T in the $\nu = 0$ to 1 range. The equation

$$\frac{1}{C_T} = \frac{1}{C_G} + \frac{1}{e^2}\frac{d\mu}{dn}, \tag{4.1}$$

where $d\mu/dn$ is the average background inverse compressibility between $\nu = 0$ and 1, allows us to determine C_G. The extracted C_G corresponds to a back-gate to density conversion ratio of 2.7x10^{16} cm^{-2}/V, which is reasonable given a h-BN thickness of 7.5-8 nm and a dielectric constant a bit less than 4.

To find C_T in a different filling factor range, we then use Equation 1, the average compressibility in this new filling factor range, and C_G, which we assume is constant. The extracted C_T then provides the conversion between the back-gate voltage and density. Throughout the manuscript, we use the same C_T for $-4 < \nu < -3, 0 < \nu < 1$, and their $\nu \rightarrow \nu + 2$ analogues. We also use a single C_T for filling factors between $\nu = -3$ and -2, $\nu = 1$ and 2, and their $\nu \rightarrow \nu + 2$ counterparts. For $|\nu| > 4$, we use the geometric capacitance.

Chapter 5

Unpublished Work: Reflectometry Measurements

5.1 Introduction

In this chapter, I present an experiment that remains unfinished. This chapter should be considered more as a glimpse into the lab notebook of an experiment in progress rather than a polished publication. It contains the seeds of what I believe to be an interesting way of observing more fractional quantum Hall phenomena. We attempt to implement radio frequency (RF) charge sensing in the quantum Hall regime. Making measurements at RF frequencies may be more sensitive and yield better visibility of observed oscillations as well as make oscillations at weaker fractions observable.

Making measurements at radio frequencies is a common way to increase the sensitivity of a measurement when the noise spectrum is dominated by 1/f noise. For ex-

ample, an aluminum-based single-electron transistor operated at 1.7 GHz was shown have an order of magnitude better charge sensitivity than comparable single electron transistors operated at DC [125]. This improvement could be achieved because the sensitivity at DC was limited by 1/f noise from background charge motion in the aluminum oxide of the SET. In GaAs/AlGaAs 2-dimensional gases (2DEG), the noise spectrum is more complicated and is an active area of research [126–129]. The noise spectrum, however, shows 1/f-like behavior up to 1 MHz [129] so RF measurements should also improve the sensitivity of measurements made on AlGaAs/GaAs 2DEGs.

Radio-frequency waves have been used to study many aspects of the quantum Hall effect. Propagation of RF waves through the integer and fractional quantum Hall effect regime were found to occur via edge magnetoplasmons [53, 130–132]. Zhitenev and coworkers used RF waves to study the edge structure in the integer quantum Hall effect and found the presence of compressible and incompressible strips [131]. The same group also used RF waves to measure the width of the edge in the integer and fractional quantum Hall effect [132]. Frequency-dependent longitudinal conductivity was used to study the Wigner crystal phase in the quantum Hall effect. Sharp resonances were interpreted as signatures of the Wigner crystal state near integer [133] and fractional quantum Hall states [134].

In this experiment, we attempt to improve our measurement sensitivity in the quantum Hall regime by measuring at a few hundred MHz. We find that RF measurements have better signal-to-noise ratios than dc transport measurements taken simultaneously at 0 magnetic field. We also find interesting behavior corresponding to changes in the bulk filling factor in the reflected signal of our resonant circuit.

5.2 Measuring signals at RF frequencies

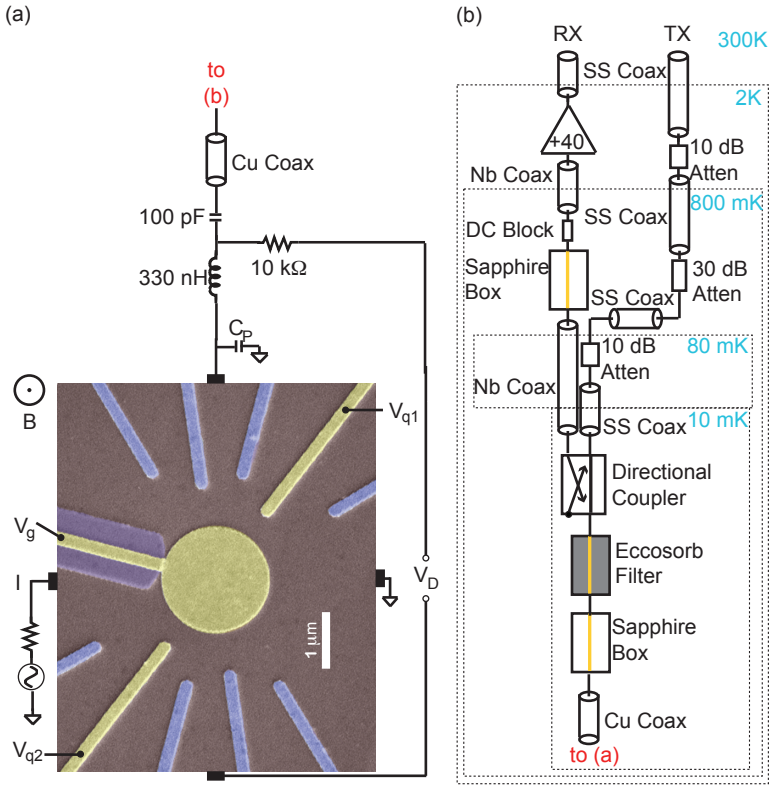

Figure 5.1: (a) Device Geometry and Reflectometry Circuit (b) Readout and Transmission Configuration in Dilution Refrigerator.

The measured device was an antidot with lithographic diameter $D = 1$ μm fabricated on a material with a 30 nm wide quantum well located 260 nm below the surface with density $n = 1.5 \times 10^{15}$ m^{-2} and mobility $\mu = 1{,}200$ m^2/V·s measured in the dark. Measurements were made using a current bias, I, with an ac component of 0.3 nA at 101 Hz. We typically measure the diagonal voltage, V_D, which is the voltage difference between incoming edge states on opposite sides of the QPC. Lock-in measurements of the diagonal resistance, $R_D \equiv dV_D/dI$, were used to determine the local filling factor within the QPC, $\nu_C \equiv h/R_D e^2$. For the RF measurement, we

monitor the reflected signal from a resonant circuit bonded to the same ohmic contact used to monitor V_D. The resonant circuit consists of the parasitic capacitance of the device to ground and a $L = 330$ nH chip inductor. The parasitic capacitance of the device to ground is $C = 0.38$ pF, which gives a resonant frequency of about 450 MHz. The other end of the chip inductor is soldered to a 50-ohm impedance matched line on the sampleholder, which is connected via coaxial lines to a cryogenic amplifier at the 3 K stage. A lithographically similar device and the resonant circuit are shown in Fig 5.1.

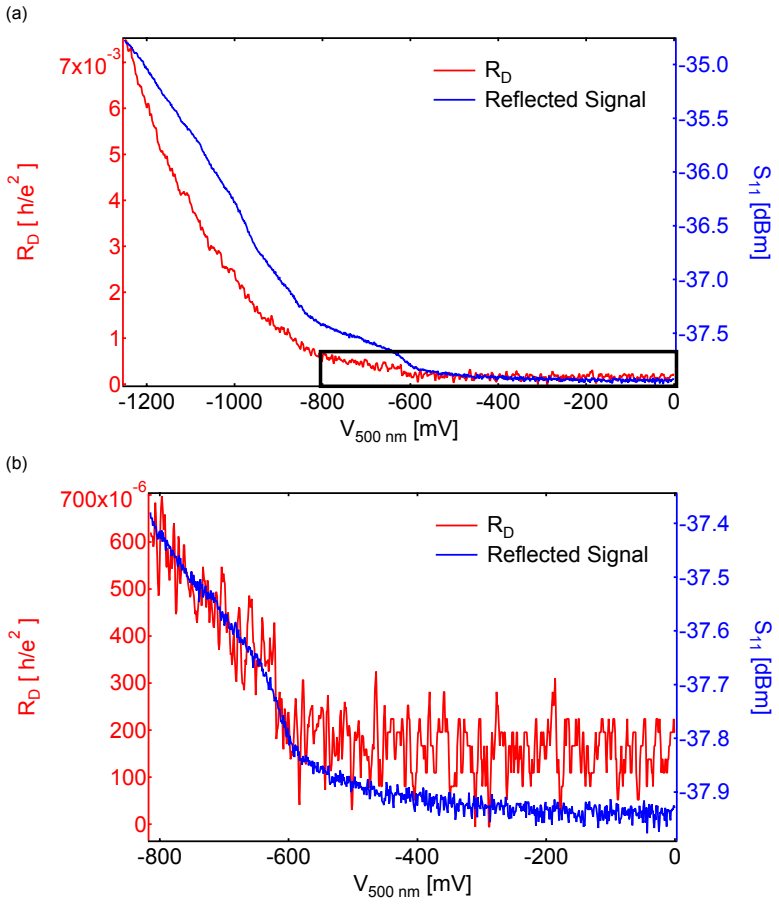

Figure 5.2: (a) R_D (red) and reflected signal (black) as a function of QPC gate voltage measured at B=0 T. Reflected signal is measured at 40 MHz. (b) Zoom-in of black boxed region in (a).

Figure 5.2 shows the reflected signal and R_D as the 500 nm constrictions were depleted at $B = 0\ T$. The 2DEG at this point contributed quite a bit of capacitance so the resonant frequency was 40 MHz. We can see that both signals respond strongly to the depletion of the constrictions. Figure 5.2(b) shows the zoom-in of the data in Fig. 5.2(a) indicated by the black box. Both signals were averaged for 300 ms. Notice that the noise in the reflected signal is quite a bit smaller than the noise from the R_D measurement.

Figure 5.3 shows the reflected signal and R_D as the magnetic field is swept upward with all gates grounded. We observe sharp increases in the the reflected signal corresponding to each integer plateau observed in R_D. These increases in reflected signal appear to be independent of frequency and persist throughout the entire measured range. We also note that at $\nu = 1$, the resonant frequency appears to shift downward before returning to its value before approaching the $\nu = 1$ plateau. This may indicate an increase in the capacitance of the system. The sharp increases in reflected signal and decrease in resonant frequency at $\nu = 1$ only occur when the quantum Hall features are visible in DC transport. The device was warmed to 10 K and neither the sharp increases nor the change in resonant frequency were observed.

Similar behavior is observed in two other materials as shown in Fig. 5.4. Figure 5.4(a) shows the reflected signal and R_D with no gates activated in a symmetrically Si-doped GaAs/AlGaAs 30 nm quantum well structure located 230 nm below the wafer surface, with density $n = 1.6 \times 10^{15}$ m^{-2} and mobility $\mu = 1{,}200$ m^2/V·s measured in the dark. We also see a decrease in the resonant frequency of the system near the beginning of $\nu = 1$ plateau. Figure 5.4(b) shows the reflected signal and R_D with

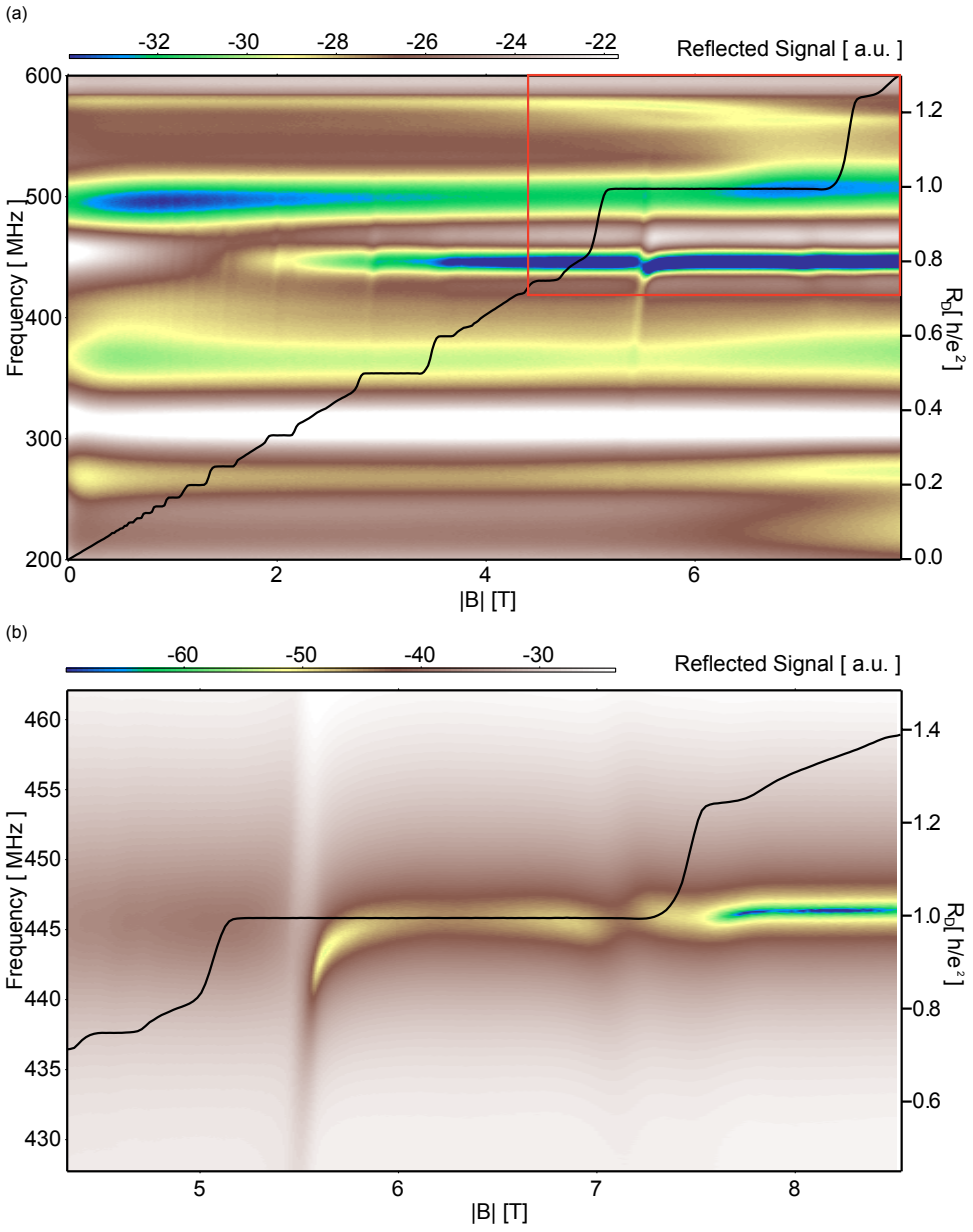

Figure 5.3: (a) Reflected Signal as a function of frequency and B. The black trace R_{D} taken simultaneously as a function of B. (b) Zoom-in of the boxed region in (a).

no gates activated in a symmetrically Si-doped GaAs/AlGaAs 30 nm quantum well structure located 200 nm below the wafer surface, with density $n = 2.6 \times 10^{15}$ m^{-2}

and mobility $\mu = 2000$ m^2/V·s measured in the dark [1]. The reflected signals from both materials show sharp increases in signal corresponding to each integer plateau observed in R_D. In this material, we see a small decrease in the resonant frequency of the system near the beginning of $\nu = 2$ plateau and also near the beginning of the $\nu = 1$ plateau. The changes in capacitance may be due to the bulk of the sample becoming very incompressible at the $\nu = 1$ states in all of the devices and the $\nu = 2$ state in the highest density material.

At high fields, however, the reflected signal became very insensitive to changes in the device resistance; we do not yet know why this was the case. Using rf-measurements, ref. [132] found that the width of the total compressible edge region of a sample at $\nu \leq 1$ was between 600 nm and 1 μm; the size of the edge depends on the details of the sample. In the case of ref. [132], their sample edge was defined by etching. Our edge region is likely even bigger because the confining potential is gate defined, and likely softer. It may be that our constrictions are too small to support the propagation of RF electrons, resulting in the path through the QPC being a lower impedance path for the RF electrons. Further experiments with etched devices or larger constrictions might shed light on this mystery.

[1]The break in Fig. 5.4(b) close to 7.5 T is an artifact from the experimental setup.

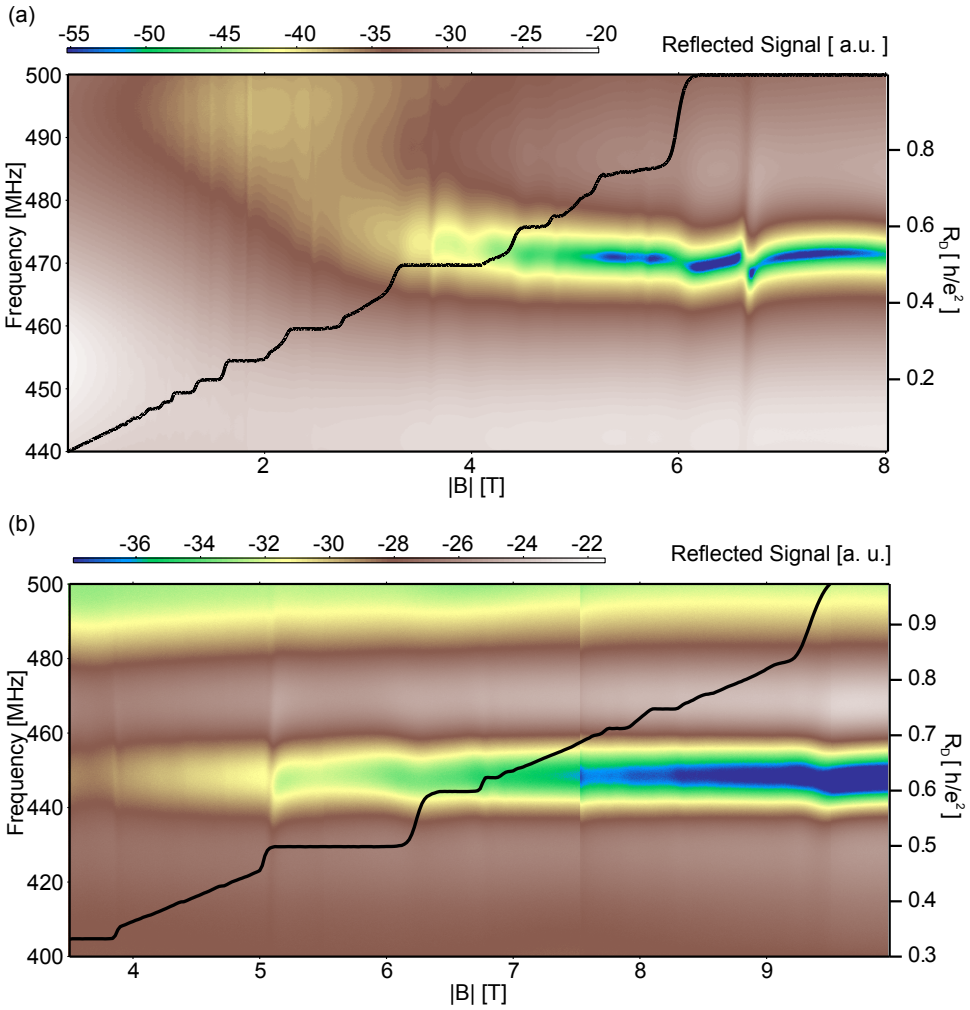

Figure 5.4: (a) Reflected Signal as a function of frequency and B in a symmetrically Si-doped GaAs/AlGaAs 30 nm quantum well structure located 230 nm below the wafer surface, with density $n = 1.6 \times 10^{15}$ m^{-2} and mobility $\mu = 1{,}200$ m^2/V·s measured in the dark. The black trace R_{D} taken simultaneously as a function of B. (b) Reflected Signal as a function of frequency and B in a symmetrically Si-doped GaAs/AlGaAs 30 nm quantum well structure located 200 nm below the wafer surface, with density $n = 2.6 \times 10^{15}$ m^{-2} and mobility $\mu = 2000$ m^2/V·s measured in the dark.

Appendix A

Electron Temperature

For a fair amount of my PhD, I wrestled with getting the electrons cold in both a wet dilution refrigerator and a dry cryogen-free dilution refrigerator. This appendix details everything I've learned and how to make the parts necessary to get your electron temperature below 20 mK.

A.1 DC Measurements

At all of the stages above the mixing chamber we used twisted pairs of 0.1 mm diameter Constantan wire, which is made of 55% copper and 45% nickel. It has a fairly constant resistivity over a wide range of temperatures ($\rho_{300K} = 52.5\mu\Omega$ cm $\rho_{4K} = 44\mu\Omega$ cm [3]) and provides good thermal isolation between the stages. Below the mixing chamber fairly thick copper wire (0.012-diameter, 99.99% from California Wire Company) was used to get from the mixing chamber to the sample. We used copper wires in order to get as much thermal conduction between the cold mixing

chamber and the sample as possible.

A.1.1 Thermalization

One of the ingredients necessary for making electrons cold is that they are well thermalized to the coldest thing possible.

Thermalizing Down to 3 K

It is fairly easy to get electrons to thermalize at 3K. For our setup, we wrapped our wiring around high-conductivity copper posts that were bolted to the plate we wanted to thermalize to using stainless steel nuts and threaded rods. Stainless steel was used because it allowed for a greater application of force to the nut to ensure that the copper post was well thermalized to the plate. We also cleaned all of the stages with acetone and isopropanol (IPA) before attaching the posts. The bottom of the posts were gently polished using Scotch-Brite to ensure good metal-to-metal contact. The DC wires were wrapped halfway down the post in one direction and then halfway down the post in the opposite direction to prevent coupling to any magnetic noise. The wires were held in place using first floss and then GE Varnish. GE Varnish works down to low temperatures and is fairly easy to remove using methanol.

Thermalizing Below 3 K

Thermalizing below 3 K becomes much more difficult. As the temperature decreases, the thermal conductivities of materials decreases and the thermal boundary resistance at the interface between materials becomes more important [136]. Never

fear though for sapphire boxes are excellent at thermalizing electrons below 3 K. The electrons travel through resistive meandering lines patterned on the sapphire. Because sapphire has good thermal conductivity at low temperatures (second only to crystalline quartz and comparable to low grade copper [136]), the electrons will be well thermalized as long as the sapphire is in good thermal contact with a cold metal. A sapphire box was used at the still, 100 mK plate, and mixing chamber plate in order to get good thermalization at each stage.

Sapphire Boxes

We use 430 μm single side polished sapphire wafers from University Wafer to make our sapphire boxes. Meanders are patterned onto the unpolished side. Clean the sapphire by sonicating for 3 minutes in acetone and then sonicating for 1 minute in IPA before blowing it dry with nitrogen. Keep the unpolished side from touching the cleanroom wipe when drying so that the surface does not get dirty. Deposit 30 nm of Chromium followed by 250 nm of Gold on the unpolished side. At some point, we tried substituting Titanium for Chromium but found that the electrons were not getting as cold. We speculated that it was because the Chromium lines were more resistive, which may actually mean that the sapphire boxes are acting as cold filters rather than thermalizers.

Clean the sapphire again without sonicating this time. If you sonicate, the metal you just deposited will flake off of the sapphire meaning you will have to etch all of the remaining metal away and redeposit everything. Bake the sapphire to 180 degrees Celsius. Spin a layer of S1813 at 5000 rpm for 45 seconds with a 5000 rpm/s

ramp rate. Make sure to cover the entire substrate with S1813 and that there are no bubbles on the sapphire. Bake at 115 degrees Celsius. Pattern the meanders onto the sapphire by exposing for 4 seconds in the AB-M Mask Aligner. Develop the pattern by dunking the sapphire for 20 s in CD-26, then 25 s in a fresh batch of CD-26, and then 15 s in de-ionized water. Move the sapphire around a bit in the beakers while you are developing.

Check your pattern in the optical microscope to make sure everything looks ok. Etch the Au using Gold etchant type TFA etch. Rinse the sapphire in de-ionized water for 15 s. Then etch the Chromium using Transene Chromium Etchant 1020. Rinse the sapphire in de-ionized water for 15 s. Remove the photoresist by leaving the sapphire in acetone for 5 minutes. You can shake the sapphire to help remove the photoresist but do not sonicate. Dip into IPA to remove acetone residue and blow dry with nitrogen. Test your lines to make sure everything is connected and the resistances are reasonable (around 50 - 100 ohms at this stage).

Anneal the sapphire in the RTP-1 in the cleanroom. We used the annealing recipe for our GaAs contacts, which heated the sapphire to 460 degrees Celsius for 75 seconds. Check the lines after annealing to make sure everything is fine; the resistances should have risen to a few hundred ohms after annealing. Clean the sapphire again without sonicating. Deposit 30 nm of Chromium and 250 nm of Gold on the polished side.

Glue the sapphire into a copper box using silver paint. We found that silver paint works better than silver epoxy; the silver epoxy would crack after a few thermal cycles in the fridge. To ensure good thermal contact and protect against any cracks in the

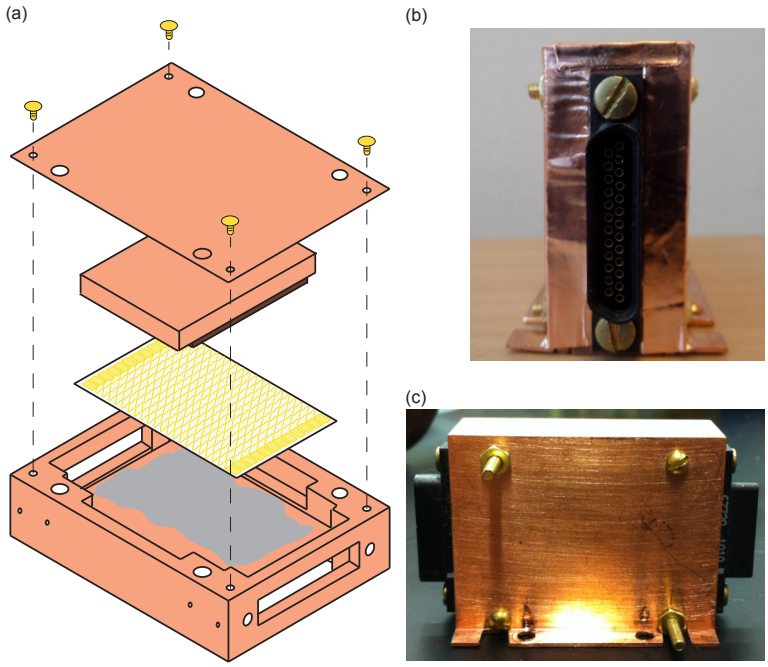

Figure A.1: (a) Exploded view of Sapphire Box Assembly (b) Side view of Sapphire Box with Connectors in U-clamp which is eventually bolted to sample plate. The copper tape protects the wires from RF leakage (c) Front view of Sapphire Box with connectors inside of U-Clamp.

silver paint, I added a press plate within the boxes. The thermal boundary resistance between the sapphire and the copper is proportional to the force used to press them together [136]. The press plate is simply a copper piece covered with Kapton tape on the side that will contact the meanders. The copper piece is made slightly thicker than the space available for it so that when the caps are screwed onto the copper boxes, a slight amount of pressure is evenly applied to the sapphire by the press plate. The sapphire box is then mounted into a U bracket which is screwed onto the stage to be thermalized to. The entire setup is shown in Fig. A.1.

Filtering

We used two filter boxes in our fridge to eliminate radiation from electronics as well as blackbody radiation from the various stages. The first filter box, known as the RF box, contained 3 stages of surface-mount pi filters for each line with cutoff frequencies of 80 MHz, 1.4 GHz, and 5 GHz. These three pi filters collectively make up one MiniCircuits VLFX-80 filter. The pi filters were soldered onto a PC board designed by Ferdinand Kuemmeth. The RF filters are enclosed in a copper box which was originally mounted to the mixing chamber plate. We had to move it to the still plate due to space constraints but did not find any change in temperature from moving it. The second filter box, known as the RC box, contained one pi filter with a cutoff frequency of 80 MHz and one stage of RC filters on each line; this box sat on the mixing chamber plate. The cutoff frequency on the gate lines was 1 kHz. The cutoff frequency on the measurement lines was 1 MHz.

A.2 Coldfingers

A.2.1 Permanent Coldfinger and Sampleholder

After thermalizing the electrons at the mixing chamber using sapphire boxes, they were connected to the sample via the copper wires mentioned above. The wires coming out of the sapphire box were shielded by tinned copper braid connected to cold metal before being fed into a hole going through the center of the coldfinger, which was designed by Patrick Gallagher. These wires then come out of the sample side of the coldfinger using a Nano-D connector from Omnetics. Hence, after thermalization and

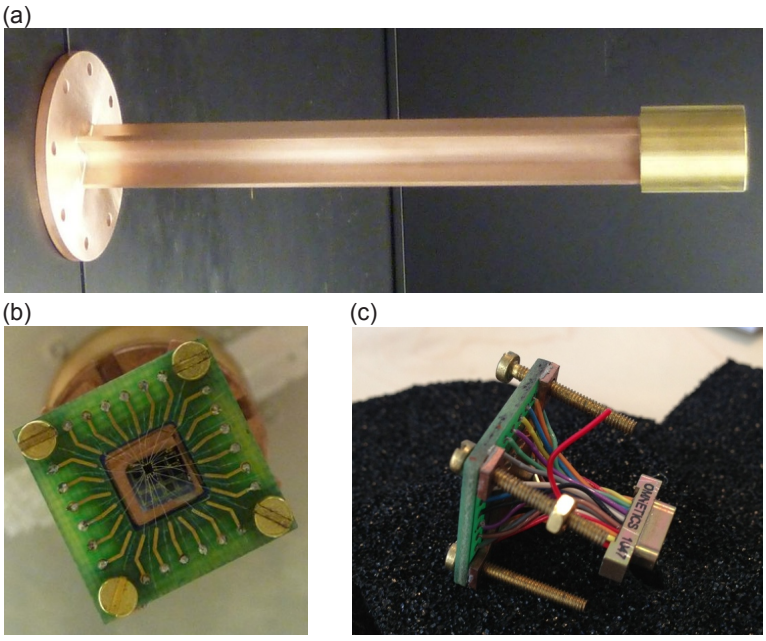

Figure A.2: (a) Coldfinger with brass can attached. (b) Top view of DC sampleholder while attached to the permanent coldfinger. (c) Side view of DC sampleholder.

filtering, the electrons are always shielded by metal from radiation. The minimization of eddy current heating was also considered in the design of the coldfinger. The cross section of the coldfinger is an X with a hole in the center. This cross-sectional shape minimizes the amount of solid copper area while maintaining structural integrity to protect against vibrations. A brass can that screwed onto the coldfinger was used to protect the sample from any radiation from the still shield and the 100 mK plate.

The sampleholder was made of a PC board glued to a copper backing piece using Stycast 2850FT. The PC board had 24 lines made of soft bondable gold. The sample rested on the copper backing piece. The copper backing piece was used to facilitate faster cooling of the GaAs lattice. The sample is held on the copper backing piece using silver paint. The entire assembly was screwed into threaded legs on the coldfinger such that the copper backing piece was in contact with the coldfinger. The front

and side of the sampleholder are shown in Fig. A.2(b) and Fig. A.2(c).

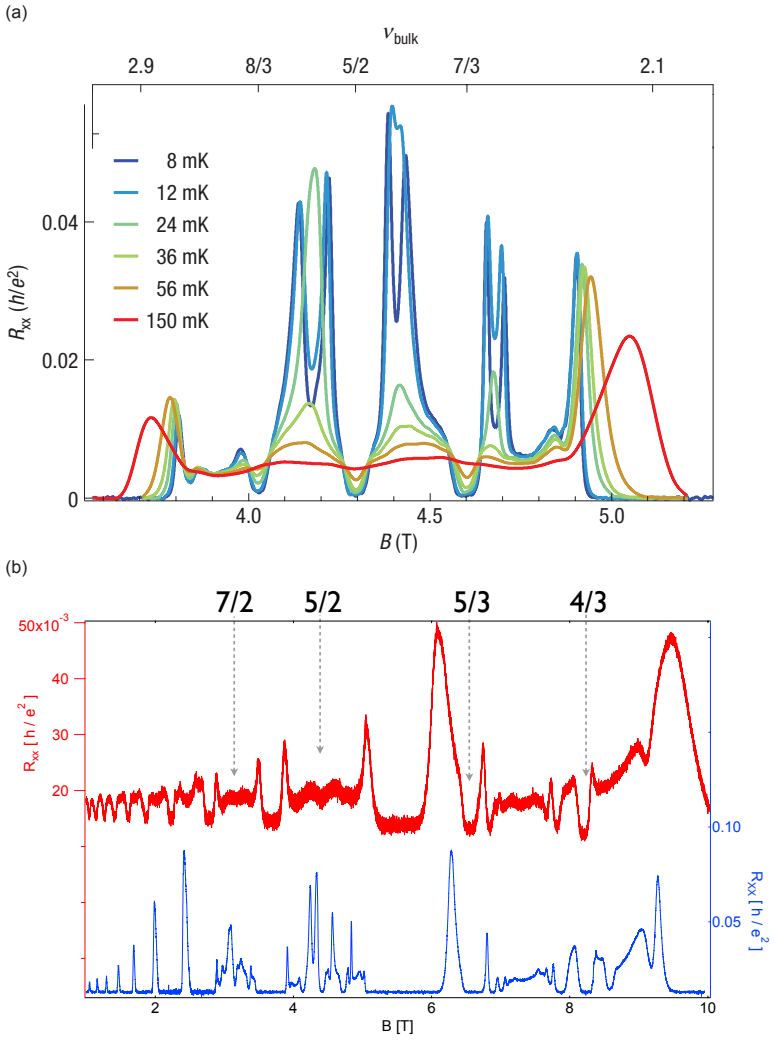

Figure A.3: (a) Longitudinal resistance as a function of magnetic field at different temperatures as measured by Jeff Miller (figure taken from [137]). (b) Longitudinal resistance as a function of magnetic field measured at base temperature before (red) and after (blue) installation of filters, sapphire boxes, custom coldfinger, and sampleholder.

Figure A.3 shows measurements of longitudinal resistance as a function of magnetic field. Figure A.3(a) was taken by Jeff Miller in a dilution refrigerator that loaded the sample into mixture [137]. The different colors indicate the different electron temperatures. We see that certain features around the $\nu = 5/2$ are very sensitive

to temperature and can be used as gauges for the electron temperature. Figure A.3(b) shows the longitudinal resistance as a function of magnetic field taken on the same material as Fig. A.3(a) before (red) and after (blue) the filters, sapphire boxes, and the permanent coldfinger were added to the Oxford cryogen-free dilution refrigerator. The red trace looks quite noisy and warm (warmer than the 56 mK trace in Jeff's data). The blue trace, on the other hand, is very quiet and is comparable to the 8 mK trace in Jeff's data.

A.2.2 Bottom-Loading Sampleholder and Coldfinger

I worked on the first bottom-loading cryogen-free dilution refrigerator ever made by Oxford Instruments. The sampleholder and coldfinger included with the system were not optimized for very low-temperature measurements so I redesigned the sampleholder and coldfinger to suit my experiment. The Oxford instruments original sampleholder and coldfinger are shown in Fig. A.4. Below I detail some considerations for designing a sampleholder and coldfinger. Figure A.5 shows my sampleholder and coldfinger.

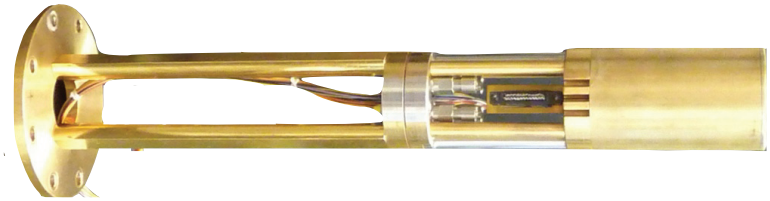

Figure A.4: Oxford original bottom-loading sampleholder and cold finger assembly.

The first thing one wants in a sampleholder designed for fast turnaround is a small

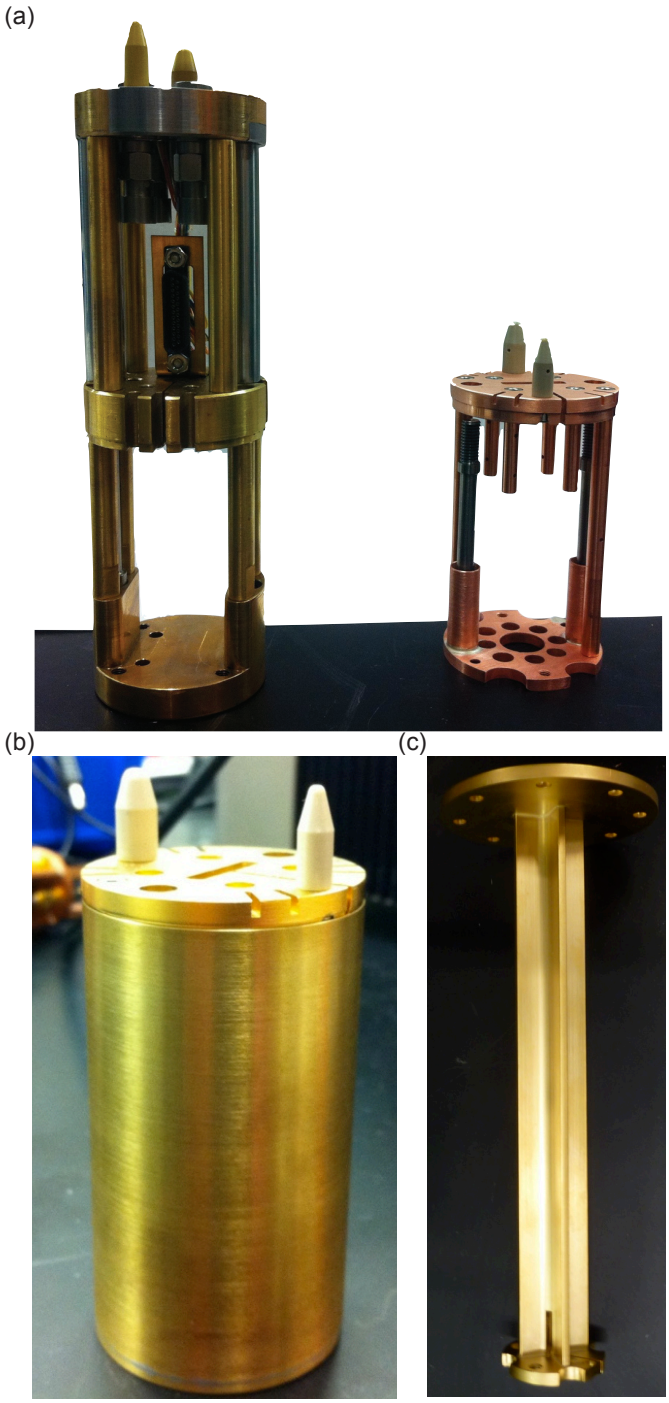

Figure A.5: (a) Oxford original sampleholder compared with Marcus Lab sampleholder with rods for holding sample attached. (b) Sampleholder with brass radiation shield attached. Top sampleholder plate has been coated with gold to protect against oxidation and help with thermalization. (c) Coldfinger with X cross-section and minimal surface area mating plate. Coldfinger has also been coated with gold to protect against oxidation.

mass. Reduction of the mass results in a reduction in cooling time of the system. This was done by making the height of the sampleholder tall enough to hold most samples but no taller. The thicknesses of the top and bottom plates were made thin but still structurally sound. The top and bottom plates were held together by two thin rods. The entire assembly was held together by non-magnetic stainless steel (Type 304 or 316) screws, which also allowed the components to be thinner since none of the joints needed to be thick enough to be braised together. This design also made the sample space larger to facilitate easier changing of samples. Figure A.6 shows the difference in cooling times of the two sampleholders. The Oxford sampleholder took 15 hours to cool to base after loading while my sampleholder took 6.5 hours to cool to base after loading.

The second thing one wants in a sampleholder is to eliminate sources of heating from the magnetic field as much as possible . Large holes were cut into the bottom plate so that there was very little surface area for eddy currents to occur. An array of slots was cut into the top of the top plate and an array of slots was cut into the bottom of the top plate also to reduce the amount of surface area for eddy currents. These slots can be seen in Fig. A.5(a). All of the components needed for thermalizing were made out of copper because it is non-magnetic. The screws were made out of non-magnetic stainless steel. It is important to make sure that the stainless steel you use is non-magnetic; non-magnetic stainless steel can become magnetic after it has been machined so always check it with a magnet. The radiation shield for the sampleholder is made out of brass, which is an alloy so it will have very little eddy current heating. The coldfinger plate that mates with the sampleholder is also made

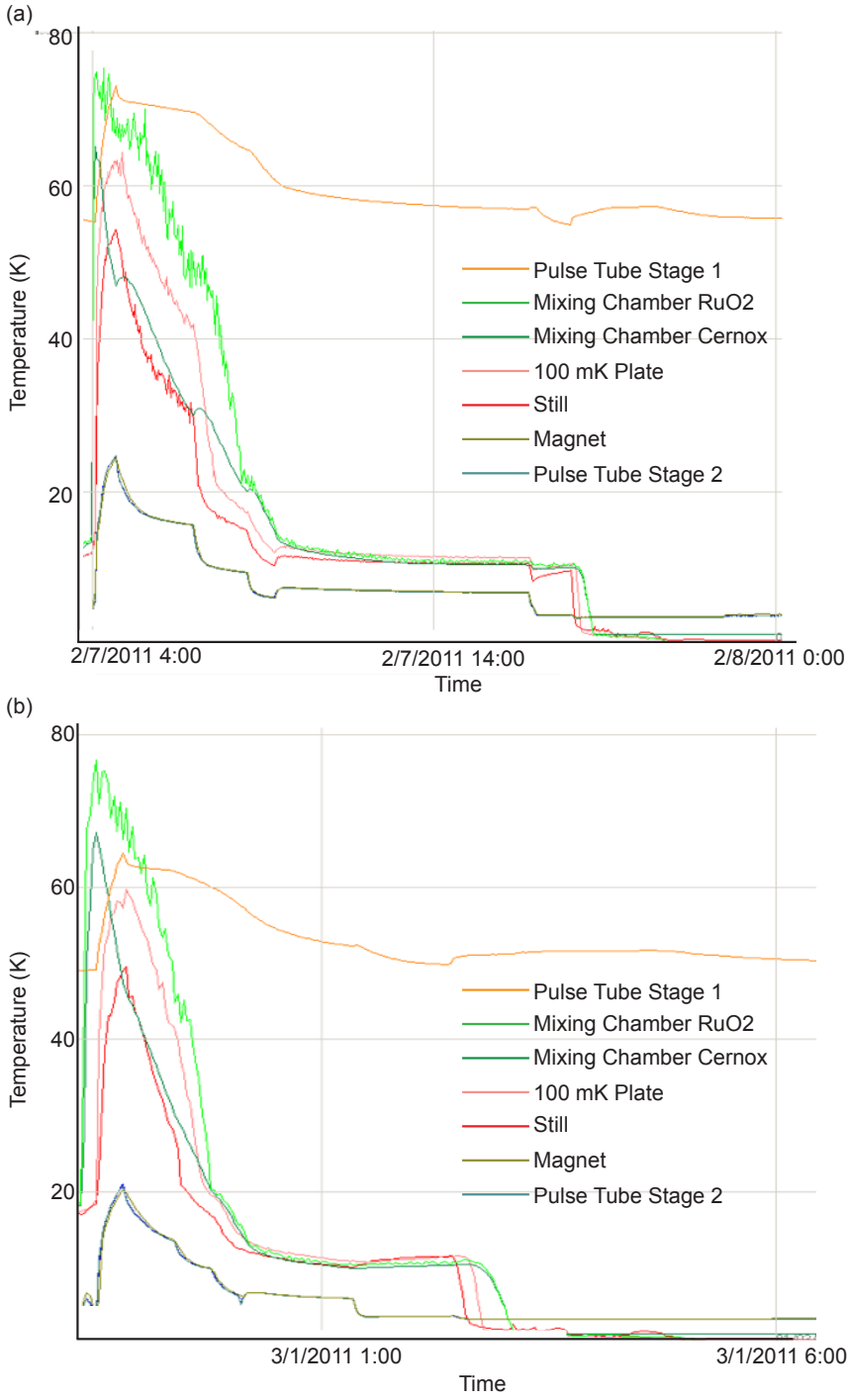

Figure A.6: (a) Dilution refrigerator plate temperatures as function of time after loading standard Oxford sampleholder. (b) Dilution refrigerator plate temperatures as function of time after loading MarcusLab redesigned sampleholder.

completely of copper for good thermalization of the sampleholder with the mixing chamber. The cross section of the coldfinger stem is an X with a hole in the center to minimize eddy current heating. Four quarter circles were cut from the outside of the mating piece on the sampleholder to reduce the solid area.

The third thing one wants in a sampleholder is shielding from radiation, which can warm your electrons. The sample wires are shielded from radiation from the mixing chamber to the sample. The brass radiation shield has indentations rather than holes where the loading mechanism meets the sampleholder in order to protect the sample from any radiation coming through those holes after the loader is removed. Once the brass can is on the sampleholder, the sample wires and sample are all shielded from any outside radiation. The coldfinger has a slot in the center for the sample wires go through to get to the connector on the bottom.

My bottom-loading sampleholder and coldfinger were installed into Willy Chang's cryogen-free dilution refrigerator. The electron temperatures achieved using the original sampleholder versus my sampleholder are shown in Fig. A.7. Note that one other adjustment was made during the loading of my sampleholder; copper press plates were installed into the sapphire boxes to achieve better thermalization.

A.3 RF Measurements

RF measurements were also taken using the cryogen-free fridge. While we still wanted to get our electrons cold, taking measurements at a couple hundred MHz meant that we also had to use coaxial lines and match impedances well. Below I detail what we use at each stage.

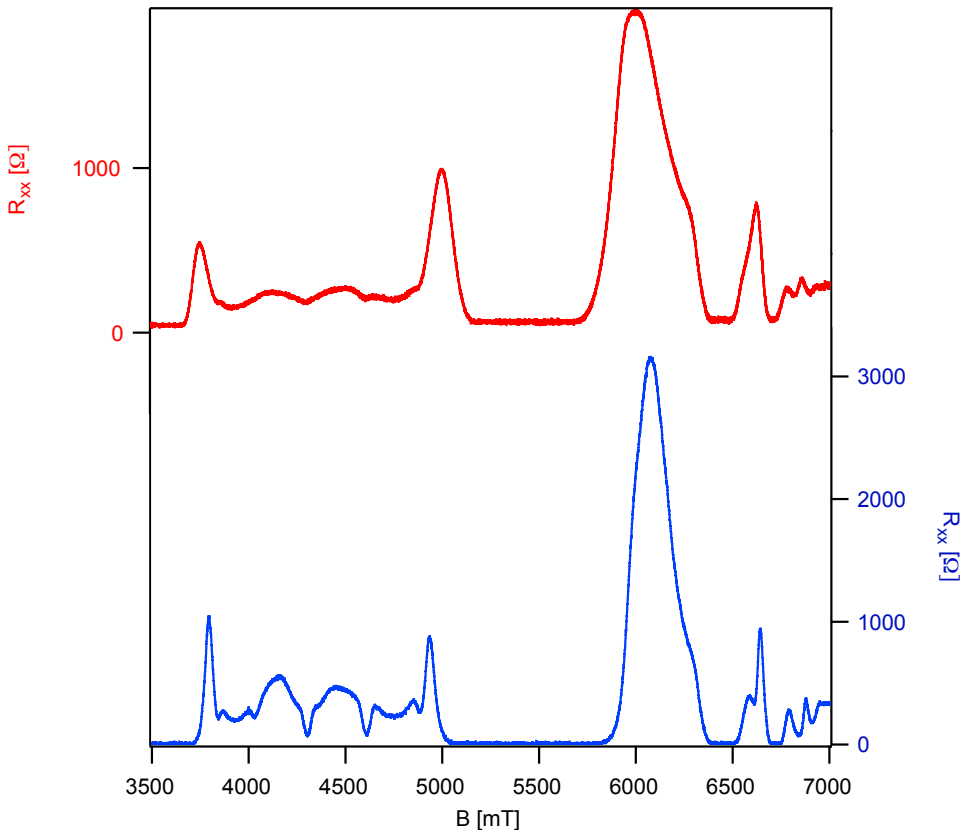

Figure A.7: Longitudinal resistance, R_{xx}, as a function of magnetic field, B, in sample mounted in Oxford Sampleholder (red) and MarcusLab Sampleholder (blue).

A.3.1 Above the Mixing Chamber

Input Line

The goal of the readout line is to thermalize the electrons as well as possible before they reach the sample. Since we can control the amount of signal going into the fridge, we attenuated the signal as much as possible in order to get cold electrons when designing this line. We used Stainless Steel (SS) coaxial lines (coax) to transmit the input signal to get from 300 K to the directional coupler on the mixing chamber plate. Ten-decibel attenuators were placed at the 3 K, Still, and 100 mK to thermalize the electrons coming into the fridge. One end of a high-conductivity copper braid connected at the other end to each stage was soldered to the outer shield of the attenuators in order to thermalize them to that stage.

Readout Line

The goal of the readout line is to get as much signal from the sample out of the fridge as possible while still keeping the electrons cold. Niobium coax was used to send the readout signal from the directional coupler on the mixing chamber plate to the still plate. Niobium coax was used because it provides good thermal isolation between plates at different temperatures but low attenuation of signal. A sapphire box and DC block were mounted on the still. The DC block was used to prevent noise from the cryogenic amplifier (cryoamp) from reaching the sample. A second strip of niobium coax connected the DC block to the cryoamp, which was mounted on the 3 K plate. A copper braid connected to the 3 K plate was pressed tightly onto the outer shield of the cryoamp in order to thermalize the cryoamp. Stainless steel coax

was used to transmit the readout signal from the cryoamp to room temperature.

RF Sapphire Box

The RF sapphire box is made in a slightly different way from the DC sapphire box mentioned above. Each box only contains one transmission line. A much larger amount of Cr/Au is deposited; we needed 1250 μm of Au for 50 nm of Cr in order to create a low impedance line. We achieved less than 1dB of insertion loss up to 5 GHz. The details of the fabrication and transmission curves are given in Ref. [138].

A.3.2 At the Mixing Chamber

The input port of the directional couple was connected to an Eccosorb filter box via an SMA male to male mating barrel. The Eccosorb filter was designed by Hugh Churchill and had a -3dB point of 1.5 GHz; the details of the material and stripline widths are given in Ref. [139]. The Eccosorb filter box was connected to the sapphire box using copper coax. Copper coax connected the sapphire box to the coldfinger.

RF Coldfinger/Sampleholder

The RF coldfinger is very similar to the DC coldfinger except there are now 4 coaxes running along the outside of the coldfinger. We used flexible coax to get from the top of the coldfinger to the sampleholder. The inner conductor of the flexible coax was silver plated copper weld and the outer conductor was tin-dipped flexible braid (available from RF coax). Once at the bottom of the coldfinger, the coax connects to a SMA-SMP connector, which then connects to the sampleholder. The sampleholder

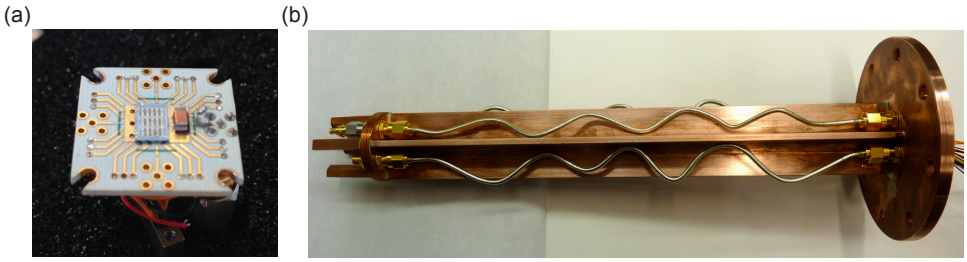

Figure A.8: (a)RF sampleholder (b) RF coldfinger

was designed on a 4-layer board made of Rogers 4350 dielectric. The sample rests on a plane of gold connected to the back of the sampleholder using 9 vias. The board was also designed to accommodate 4 RF lines. Each of the lines can also accommodate an on-board bias tee. We only used one of the lines for our experiment. The area beneath the inductor for our resonant circuit does not have a gold plane in order to reduce the parasitic capacitance from the inductor to ground. The back of the sampleholder is coated in gold (except for the area under the inductor) and is thermally connected to the coldfinger legs. The RF coldfinger and sampleholder are shown in Fig. A.8. The total insertion loss from the lines from the top of the fridge to the bottom of the coldfinger at room temperature was 5 dB at 500 MHz.

Appendix B

GaAs Fabrication

The strategy for fabricating devices is to be as precise and careful as possible but to try not to spend your entire PhD in the cleanroom.

B.1 Making Mesas

Cleaving Chips

Use the LSD-100 Scriber to cleave GaAs chips. The scriber should be at 14 kPa toolholder pressure and the setting should be on Notch. After a notch has been made in the chip, cover it with a cleanroom wipe and manually push the roller over the top edge of the chip. You should hear the chip break. Always cleave a junk chip first since the scriber sometimes does not land where the lines indicate on the computer screen.

Cleaning

Clean the cleaved chip using the 4 step clean with sonication is: 5 minutes in trichloroethylene, 5 minutes in acetone, 5 minutes in IPA, and 5 minutes in de-ionized water. Blow the chip dry with nitrogen and then bake it for 5 minutes on the hot plate at 180 degrees C.

Photoresist Spinning

Spin S1813 at 5000 rpm with a ramp rate of 5000 rpm/s for 45 seconds. Remember to clean off the chip holder with acetone before spinning as it often has photoresist resides on it. Bake for 2 minutes at 115 degrees C.

Photolithography

Clean off both sides of the mask using acetone and IPA. Use the mask aligner in the soft matter room. Remember that the brown side of the mask will be the side that comes in contact with your chip. Expose for 4 seconds.

Develop

Develop by putting the chip into CD-26 for 20 seconds, then into a fresh batch of CD-26 for 25 seconds and then de-ionized water for 15 seconds. Blow the chip dry with nitrogen.

UV Ozone Clean

Clean the chip using the Samco UV Ozone cleaner for 45 s, no heat. Make sure the flow meter reads 1 for the O_2 gas.

Etch Solution

Mix a solution of 240 milliliters of de-ionized water, 8 milliliters of hydrogen peroxide, and 1 milliliter of sulfuric acid. Always add acid to water rather than water to acid. Stir and let it sit for a few minutes. Prepare a small beaker of de-ionized water next to the etch solution to dip your chip into after etching to stop the etch.

Checking Height of Mesas

Use the Dektak profilometer to check the height of mesas before and after etching. Before you remove the resist, the settings for the profilometer should be:

Scan Length - 150 μm

Scan Time - 15 s

Stylus Force - 10 mg

Measurement Range - 655 $\mathring{A}$

Hills and Valleys

After removing the resist, the measurement range should be changed to 65 $\mathring{A}$. All of the other settings should be the same.

Etching

You should aim to etch past the first donor layer in GaAs; this will ensure that you isolate mesas from each other as well as keep you from having to evaporate an inordinate amount of gold when you make gate pads. It is best to dip a GaAs junk chip into the etch solution first to get a sense of etch rates before you dip your actual sample. The etch rate is typically 1.5 nm/s. Clean the solution off by dipping your chip in de-ionized water and blow it dry with nitrogen. Check the height to make sure you etched enough using the profilometer.

Removing Photoresist

Sonicate for 1 minute in acetone and then 1 minute in IPA. Blow dry with nitrogen.

B.2 Making Ohmics

Cleaning

Do a 4-step clean with sonication.

Spinning Electron-Beam Resist

Prebake the sample at 180 degrees C for whatever amount of time it takes you to pour out the electron-beam resist you need and set up the spinner. Test the spinner by spinning your chip dry. Use a 4000 rpm/s ramp rate for all of the following steps. Spin a layer of C6 at 4000 rpm for 45s. Bake for 5 minutes at 180 degrees C. Spin another layer of C6 at 4000 rpm for 45 s. Bake for 7 minutes at 180 degrees C. Spin

a layer of A4 at 4000 rpm for 45 s. Bake for 10 min at 180 degrees C.

Elionix

I refer you to Jimmy and Hugh's excellent Elionix guide for directions on usage and only give doses here. For ohmics, we use aperture 4, which gets us a beam current of 25 to 30 nA. The dose is 1200 uC/dot, 20,000 dots, and a 600 μm write field. You may need to write the alignment marks twice for them to come out nicely.

Develop Electron-Beam Resist

Dip chip in 1 part Methyl Iso-Butyl Ketone to 3 parts IPA for 90 seconds at room temperature. Clean the developer off by dipping chip in IPA for 30 seconds at room temperature. Blow dry with nitrogen.

UV Ozone Clean

No heat, 80 seconds, Flow at 1.

Oxide Clean

Dip chip in Ammonium Hydroxide for 3 seconds followed by 15 seconds in de-ionized water. Immediately put chip in evaporator.

Ohmic Evaporations

We have two recipes for making ohmics. Both of which work equally well. Be sure to use your own metals for both the electron-beam evaporator and the thermal

evaporator or you might lose a good chunk of your life wondering why your ohmics don't work.

Electron-Beam Evaporator Ohmics

Platinum (Pt) 50 $\mathring{A}$

Gold (Au) 2000 $\mathring{A}$

Germanium (Ge) 1000 $\mathring{A}$

Pt 730 $\mathring{A}$

Au 1000 $\mathring{A}$

Ge 500 $\mathring{A}$

Pt 550 $\mathring{A}$

Thermal Evaporator Ohmics

Nickel (Ni) 60 $\mathring{A}$

Ge 1350 $\mathring{A}$

Au 2700 $\mathring{A}$

Ni 400 $\mathring{A}$

Au 250 $\mathring{A}$

Liftoff

Leave chip in acetone for an hour or so. If you need to sonicate, use a plastic beaker. Wash off acetone residue with a dip in IPA and blow dry with nitrogen.

Annealing

Anneal the electron-beam evaporator ohmics to 530 degrees C using the rapid thermal annealer (RTP-1) in the cleanroom. Anneal the thermal evaporator ohmics

to 460 degrees C using RTP-1.

B.3 Making Gates

Cleaning

Sonicate chip in trichloroethylene for 5 minutes, acetone for 3 minutes, and IPA for 1 minute. Blow dry with nitrogen. This will now be known as the 3-step clean.

Spinning Electron-Beam Resist

Prebake as detailed above. Spin a layer of MMA EL-6 at 4000 rpm for 45 s. Bake for 5 min at 180 degrees C. Spin a layer of C2 at 4000 rpm for 45 s. Bake for 20 minutes at 180 degrees Celsius.

Elionix

For small features, use aperture 1 at 100 pA. The dose will be found from your dose test; it is usually somewhere between 2500 and 3000 uC/dot. Use 60,000 dots and a 75 μm write field. Remember to burn spots! I like to change the z height rather than the focus when burning spots. Eventually they should be perfectly round circles.

For large features, use aperture 1 at 1 nA. The dose will be 2700 uC/dot. Use 60,000 dots and a 300 μm write field. You might get stitching errors in this step of writing so it is prudent to make a separate patch pattern to cover the areas in between chips.

Develop

Cool MIBK:IPA 1:3 in ice for 15 minutes. Develop for 90 seconds in MIBK:IPA. Wash off in IPA for 15 seconds at room temperature. Blow dry with nitrogen.

UV Ozone

No heat, 60 seconds, Flow at 1.

Thermal Evaporation

Evaporate 80 $\mathring{A}$ of Titanium (Ti) followed by 420 $\mathring{A}$ of Au.

Liftoff

As described above.

B.4 Making Gate Pads

Cleaning

3-step clean, no sonication.

Electron-Beam Resist Spinning, Elionix, Developing, UV Ozone Clean

Same recipes as for making ohmics.

Thermal Evaporation

Evaporate 150 $\mathring{A}$ of Ti followed by (the height of your mesa + 10 %) of Au.

Liftoff

As described above.

B.5 Specific to Antidot Devices

For the antidot devices, we have to get really good alignment between the antidot gate and the screening gate as well as put a layer of HfO_2 in between the two gates.

Making HfO_2 layer

For patterning the HfO_2 layer, follow the instructions for making gate pads given above until the thermal evaporation step. This step will be replaced by atomic layer deposition of HfO_2.

Atomic Layer Deposition We use a precursor of tetrakis(ethylmethylamino)hafnium and water to make HfO_2. The chamber has to be kept at 130 degrees C to prevent hard baking of the electron-beam resist. Run the HfO2_130C recipe in the cleanroom ALD machine. You should need about 400 cycles for 30 nm. The color on GaAs should be light brown after deposition.

Liftoff Liftoff in warm acetone (60 degrees C) for 1 hour. You can sonicate in a plastic beaker if necessary. Wash off acetone residue in room temperature IPA and blow dry with nitrogen.

Making Antidots

Follow the same recipe as given above for gates and gate pads but remember this note about alignment: If you need to get very good alignment for different sets of

gates such as is necessary for the screening gate and antidot gate in the antidot devices, write alignment marks no more than 100 μm away from your gate during the writing for the first set of gates. When you write the second set of gates, align to this set of alignment marks rather than the ones written during ohmic writing. Use a small viewing window ($>$ 2000x magnification on the Elionix EL-7000) so you don't expose large areas of your chip during alignment. You can also burn spots on your alignment mark in order to help in finding it during the registration step later.

Good luck!

Appendix C

Graphene Fabrication

Note: most of this fabrication was taught to me by Javier Sanchez-Yamagishi. The following just contains some additional directions specific to fabricating at Harvard.

C.1 Preparing Substrates

The wafers that we use are supplied by Nova Wafers. They have 285 nm of dry thermal oxide grown on the silicon.

Cleaving

I usually cleave the silicon chips into 25 mm by 25 mm chips by hand using a tungsten-carbide scriber from VWR (Part Number 52868-004) but you can also use the LSD-100 scriber in G12.

Cleaning

Clean the wafer by sonicating it in acetone for 5 minutes and then in IPA for 5 minutes. Blow the chip dry with nitrogen.

Making Alignment Marks

Pattern and deposit alignment marks onto the chip using the standard recipe for alignment marks given in the graphene fabrication powerpoint on the Yacoby lab server. The files for the alignment marks are EbeamAlignment3.dxf and TransferMarks.dxf. EbeamAlignment3 are the standard marks used for small chips. TransferMarks writes a matrix of letters and numbers so it is easy for you to know where you are located on a big chip.

C.2 Depositing Graphite

Cleaning

Sonicate the substrate with alignment marks in acetone for 5 minutes and then in IPA for 1 minute. Blow dry with nitrogen. Then clean off any residues on the substrate using an O2 plasma etch for 45 s in the RIE-8. Carefully wipe off the thermal paste on the back of the chip using a small amount of IPA on a q-tip. Put the chip on top of a glass cover and not on a cleanroom wipe since this will introduce tiny hairs onto the substrate.

Exfoliating Graphite

Exfoliate a film of graphite off of the larger piece using a piece of Ultron Systems Blue Tape 1011-R. Make sure not to touch the sticky part of the tape with any part of anything except graphite. I usually make a double deposition by putting a piece of blue tape on both sides of the large piece of graphite. This ensures that the whole Si/SiO_2 chip will be covered and we will also eventually use these for transfer stacks which are also roughly the size of two graphite squares.

Remove the tape from the graphite and then stick them to each other as shown in Fig. C.1. This first tape will now be the master tape from which all future graphite pieces will be exfoliated from. Peel the tapes slowly away from each other and attach a new piece of tape to the tape with more graphite. Since we are making graphite pieces, we do not want things to be too thin so repeat this process just 2 or 3 times before depositing onto the Si/SiO_2 chip. Save any of the other tapes that have large areas of graphite for eventual graphene deposition by putting a new piece of blue tape onto them.

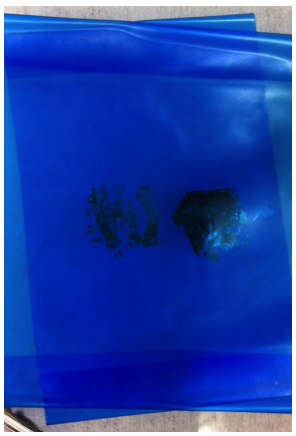

Figure C.1: Graphene tape with 2 squares of graphite.

We are now ready to deposit onto the substrate. DO NOT HEAT THE CHIP WHEN DEPOSITING WITH BLUE TAPE! This will melt the glue on the tape and leave all kinds of unpleasant residue on your chip and most importantly on your graphite. Push the tape down firmly with your finger and then peel off.

Optical Mapping

Search for graphite using an optical microscope. You generally want graphite that is between 10 and 30 nm. On the substrates we use, good graphite looks purplish blue to bright blue. Some examples are shown in Fig. C.2.

Heat Cleaning

An SOP for the heat cleaning process written by Benjamin Feldman and me resides on the Yacoby lab server in the Common/Fabrication Procedures/Graphene folder. The chip with graphite is heat cleaned using a tube furnace. Be sure that you are using the graphene tube when heat cleaning; it is usually in the tube furnace but double check the cardboard holder for the tubes. A 50/50 mixture of Ar/H_2 flows through the tube while the substrate is heated to 350 degrees C for 3-7 hours depending on how busy the furnace is or whether you are cleaning overnight. Three hours is usually enough to remove any residues from the sample but if the tube has been in use for a while it can take longer. Heating the substrate can weaken the SiO_2 so I try not to anneal for longer than 7 hours at each step. If you are not using the silicon as a back gate, you may want to consider using resistive silicon as the substrate. Remember to clean the tube by heating it to 1000 degrees Celsius after you remove your sample. The usual tube cleaning time is 1 hour.

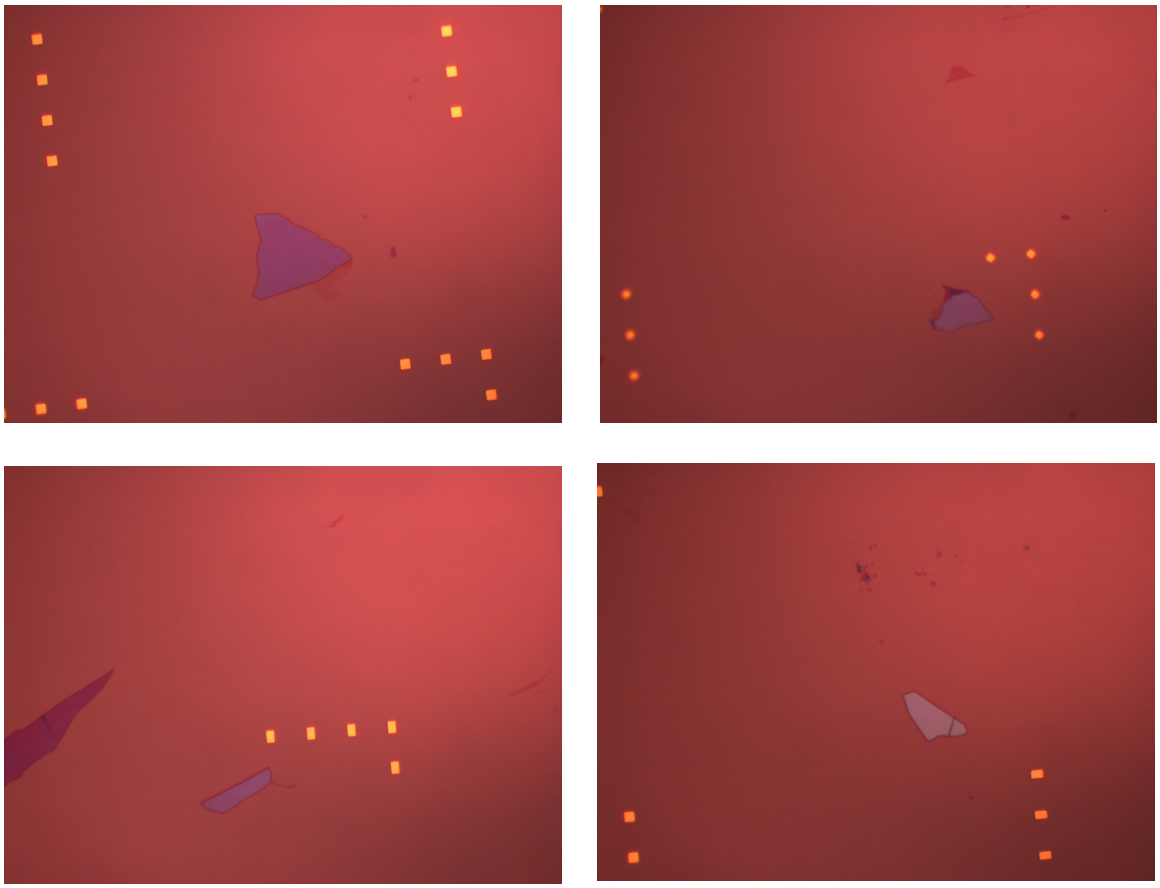

Figure C.2: Optical Images of Graphite at 100x Magnification. Images show samples in order of ascending thickness from left to right.

AFMing the Graphite

Now we have to find the best pieces of graphite of the ones we found during optical mapping. We use the Veeco NanoMan in the cleanroom because it has a good enough noise floor (∼0.2-0.3 nm) and moves the sample rather than the AFM head, which allows for a much greater range in XY position than the Asylum AFMs in G12. Also, it uses vacuum to hold the sample rather than using crystal bond which can leave residue on your sample during the removal process. The tips we use are AC160TS tips from Asylum Research. Usually one has on the order of 20 good graphite pieces on the chip so it's important to be able to screen them efficiently so you don't spend your entire PhD on the AFM. The strategy for finding good graphite pieces quickly is to start out with a coarse scan using a scan window of 20um and if no residue or large steps can be seen using this scan window to then focus on a small window of about the sample size you wish to make. For all of your zoom-ins use a height scale of 5 nm and a phase scale of 20 degrees. I like to use the Scan-Triple window and look at the Height, Phase, and Amplitude Error. Phase and Amplitude Error can show more information since Height data can be swamped by any tall features on the substrate. Do not use a tip velocity faster than 40.1 um/s. If no large steps or residue are seen at this window size then the sample can be considered good and you can move on to the next piece. Examples of good and bad pieces of graphite are shown in Fig. C.3.

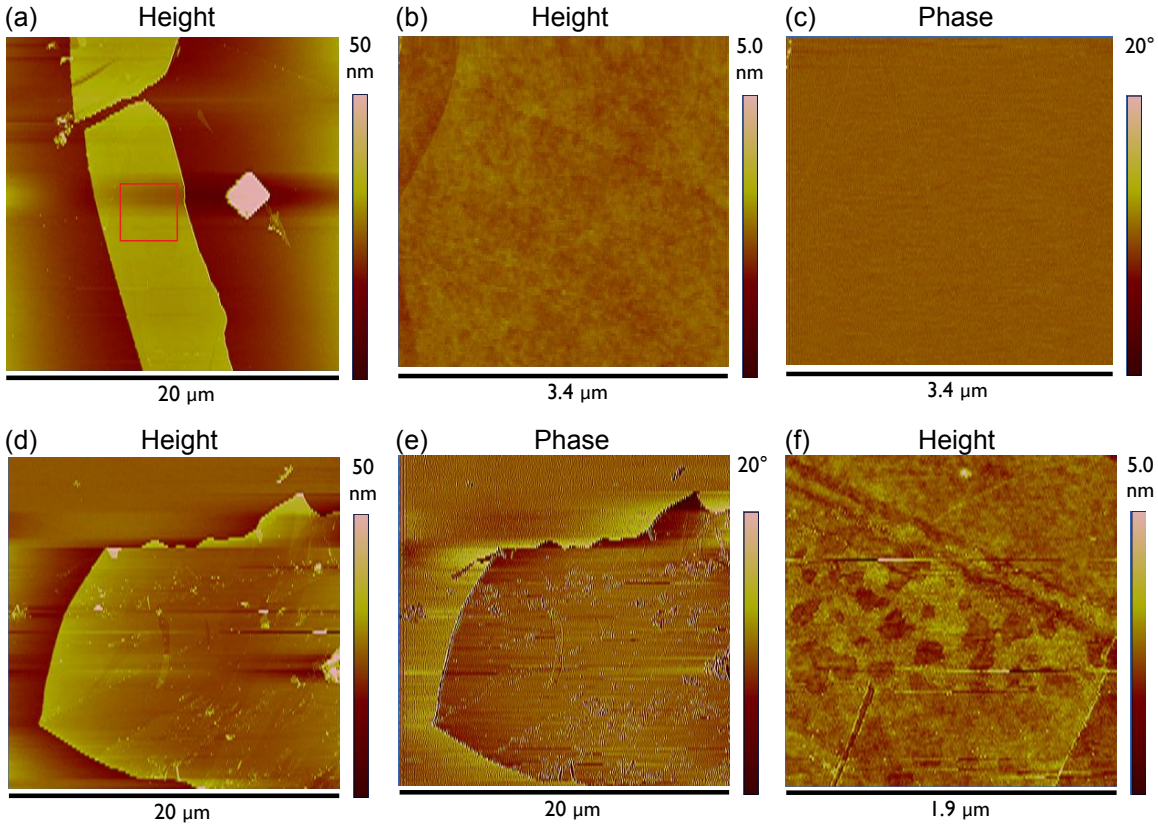

Figure C.3: AFM Images of Graphite. (a) AFM image showing the height of a clean piece of graphite. The height (b) and phase (c) of the red square indicated on the graphite are shown. (d) AFM image showing the height of a dirty piece of graphene. The corresponding phase is shown in (e). A zoom-in of a dirty region on another piece of graphite is shown in (f).

C.3 Preparing Transfer Stacks

Javier has prepared a really good guide for making transfer stacks (also resides in the same folder as the Heat Cleaning SOP on the Yacoby lab server) so I won't repeat all of the details here but simply give some tips that might help making them go a bit smoother. The goal of making these stacks is to make the entire stack as smooth and flat as possible.

Making PDMS

If you are planning on making transfer stacks soon, the first thing to do is prepare PDMS since it takes 24 hours to cure. PDMS also does not go bad so it does not hurt to always have some PDMS on hand. After measuring out (10 grams of Part A and 1 gram of Part B) and mixing the PDMS mixture using the plastic end of a q-tip for 2 minutes, put the lid on the Yacoby lab sonicator in the sample prep room and sonicate on top of the lid for 13 minutes (more than this is ok, less is not). This will get rid of the bubbles in the mixture and will give you smooth PDMS to work with later. Remember to periodically check that the petri dish holding the PDMS mixture is laying flat on the sonicator so you don't get ridiculously thick PDMS on one side and ridiculously thin PDMS on the other. When you are done sonicating, leave the petri dish with the mixture on the windowsill and in 24 hours you will have PDMS.

All of the next steps should be done in the cleanroom.

Making Glass Slides

Cut a few glass slides in half using the tungsten-carbide scriber mentioned previously. Sonicate these halves in IPA for 5 minutes to get rid of any glass dust or cleanroom wipe hairs. When you blow them dry with nitrogen make sure that at least one side never touches a cleanroom wipe.

Sticking PDMS to Glass Slides

Cut out a piece of PDMS and place it on the glass slide using the rolling wavefront method so you don't get bubbles between the PDMS and the glass slide. Do not roll

too hard or your PDMS will get lines through it. The glass slide should extend about 3 mm out on each side of the PDMS. Place these PDMS/glass slide stacks into the Samco UV Ozone cleaner for 15 minutes (no heat) in order to facilitate tape sticking to them.

Sticking Tape to PDMS/Glass Slide Stack

We now want to put tape on these stacks. Remove the entire outer layer of tape and then VERY quickly unroll a 5 inch piece of tape in one motion so that there are no lines in the tape. Again using the rolling wavefront method, stick the tape onto the PDMS/glass slide stack without trapping any air bubbles.

Spinning MMA onto Tape/PDMS/Glass Slide Stack

Prebake the stack to 120 degrees C for 4 minutes. Spin one layer of MMA EL-6 at 1200 rpm for 70 seconds onto the stacks. Bake for 10 minutes at 120 degrees C. Cool for 30 seconds. Spin and bake another layer of MMA in the same way.

Exfoliating Samples onto the Transfer Stack

Depending on which stack you are making at the moment, either exfoliate some graphene using the tape saved during the graphite deposition step or make a boron nitride tape by stamping little flakes of hexagonal-boron nitride (hBN) on a piece of blue tape.

You can make a hBN stamp using the following steps. First cut out a 2mm by 10 mm piece of PDMS and lay it flat on a cleanroom wipe. Next cut out a 4 mm by 15 mm piece of blue tape. Put the unsticky side of the blue tape onto the piece of

PDMS. The PDMS should have adhered to the blue tape and the sticky side of the blue tape should be facing upward. Use a clean pair of tweezers to take 5 or 6 hBN flakes from the sample box and drop them onto the blue tape; probably it would be best to designate a pair of tweezers the hBN tweezers. Pick up the stamp by the two shorter edges and stamp the hBN onto a larger piece of blue tape until you get a fairly dense region of hBN that is about the size of the PDMS on the glass slide. Put a clean piece of blue tape onto this master tape and exfoliate hBN by peeling the tape off. Save the first hBN tape by putting a clean piece of blue tape onto it. This large piece of blue tape will be your master hBN tape and can be reused.

When you are satisfied with a tape, it is time to transfer the hBN or graphene onto the MMA-tape-PDMS-glass slide stacks. Put the blue tape onto the transfer stacks making sure not to get blue tape onto the top edge where the MMA and tape run over the PDMS edge. If the tape gets stuck there, you will pretty much guarantee that the MMA will be ripped off of the stack and the stack will not be useable. Gently rub the blue tape with teflon tweezers using just the weight of the tweezers for a few seconds and then very slowly peel the tape off of the stack. The peeling of tape off of the stack can take a few minutes. Be patient and you will be rewarded with a transfer stack with some good pieces of hBN or graphene on it.

C.4 Creating Transfer Squares

Mapping Boron Nitride or Graphene

Using an optical microscope with a micrometer, take 10x, 20x, and 50x pictures of promising samples and note their positions in the files somehow. Remember to turn on the 3200 K setting on both the hardware and the software if you are using Pablo's microscope at MIT. Find the upper right corner of your transfer stack and reinitialize the micrometer by pressing the up and down buttons on the stage. Turn on the software. Your exposure time for the 10x and 20x magnifications should be around 20 ms and the exposure time for the 50x magnification should be about 50 ms. Good hBN samples, which are not layered and between 5 and 15 nm in thickness, look translucent white in Pablo's microscope at MIT. Good graphene samples can barely be seen under 50x magnification. Any piece of graphene that is easy to see is usually more than a few layers thick and not interesting. You can decrease the aperture to try to help you determine whether a sample is graphene. Try to find samples that are more than 2 mm apart since the square you cut out will be about this size. Good hBN samples are shown in Fig. C.4. Good graphene samples are shown in Fig. C.5.

Marking Sample Locations on Transfer Stacks

Next flip the entire stack over so the glass side part is on top and support it so that the side with your sample does not hit anything. Pablo's group has made glass slide squares expressly for this purpose. Using the positions you've noted, locate the samples using the microscope on the 20x setting. After you have found the sample, go back to the 10x setting and center your sample in the viewing window. Use a

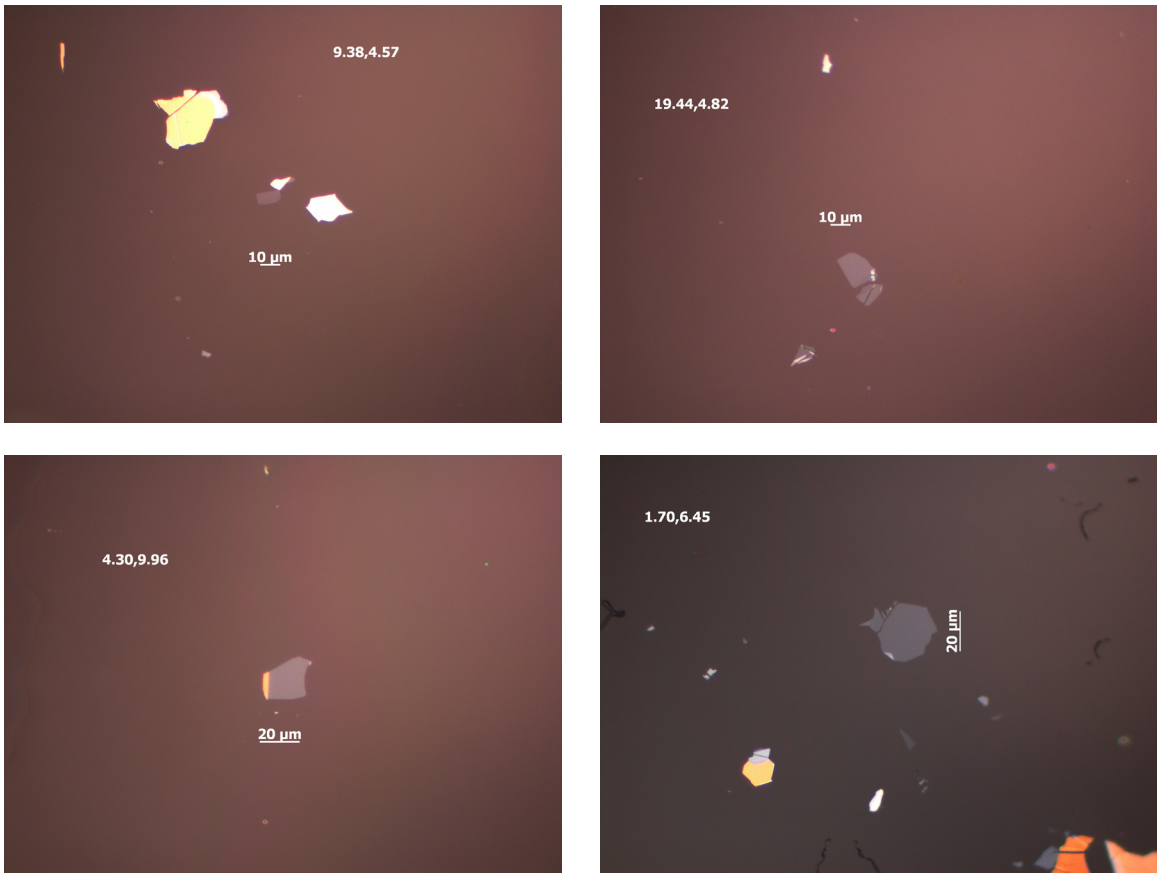

Figure C.4: Optical Images of hBN at 50x Magnification. Images show samples which are about 10 nm in thickness.

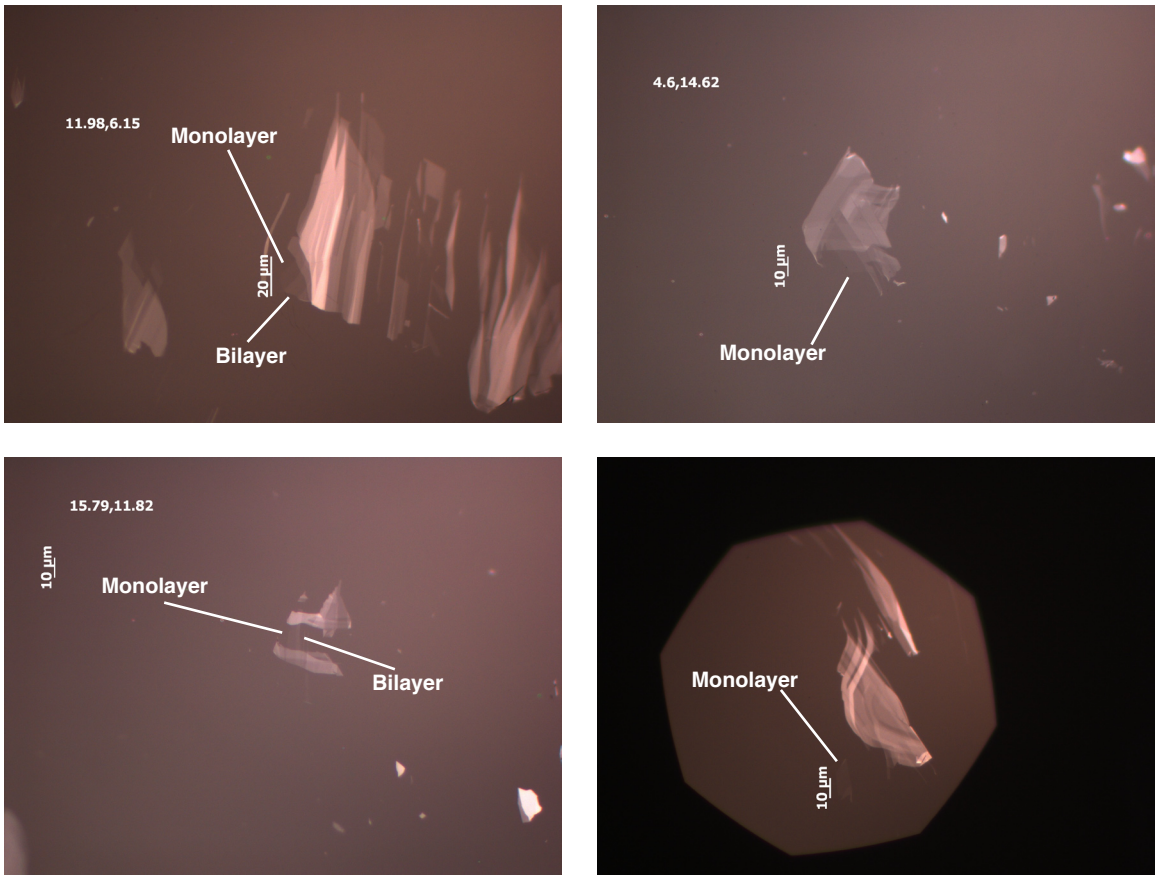

Figure C.5: Optical Images of Graphene at 50x Magnification. Number of layers are indicated in the images. The bottom right image shows a decreased aperture.

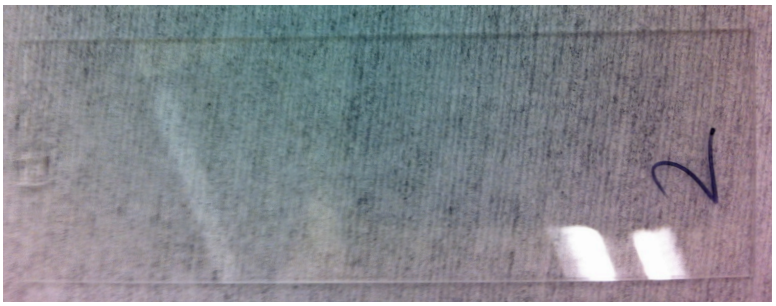

Figure C.6: Transfer slide with identifier on the slide and transfer square located in the center of the left edge.

marker to place dots on the glass slide where the beam of light from the microscope is reflected off of the glass slide. Double check that your mark is in the correct place after you have made it by looking in the microscope; there should be a black spot where your sample used to be. Repeat this for all of your samples.

Cutting Out Sample Squares

Remove the stack from the microscope. Flip the stack over so the MMA layer is on top and use an X-acto knife to cut squares of about 2 mm around the dots you wrote. Make sure the lines that form the edges of the square intersect so that the square is definitely isolated from the rest of the PDMS. Cut all of the squares before removing any of them. When you are finished cutting, use flathead tweezers to take the squares off of the glass side and put it on a clean glass side that has been labeled with some identifier so you know which square corresponds to which flake as shown in Fig. C.6. Be very careful not to bend the square when you are removing it because this will damage the MMA as well as your sample. Also make sure that the square has adhered well to the clean glass slide by poking it on each side. You definitely do not want the square to delaminate during the transfer process.

C.5 Transferring Samples from the Squares to the Substrate

Place your sample onto the transfer microscope stage and turn on the vacuum to make sure it stays in place. Plug in the temperature controller. Adjust the stage so that the sample you would like to transfer to is centered in the field of view using the thicker part of the silver knobs below the stage. Lock the stage by rotating the thinner part of the silver knobs below the stage clockwise. Mount the glass side (sample facing down) into the XYZ manipulator. Make sure the back of the glass slide is flush against the back of XYZ manipulator. Make sure that the z height of your sample is high enough so that it will not hit the substrate on the microscope stage. Rotate the XYZ manipulator so that the transfer stack is above the sample on the substrate that you would like to transfer to. Adjust the angle using the two black knobs on the holder so that the top edge of the transfer stack is parallel to the substrate.

Adjust the focus of the microscope (gently!) halfway in between focusing on the sample on the transfer stack and focusing on the sample on the substrate. Lower the sample on the transfer stack until it comes into focus. Continue adjusting the focus to halfway in between and lowering until the sample on the transfer stack and the sample on the substrate are in contact; you can tell they are in contact because the focus will be the same for both. You may need to adjust the x and y position of the sample on the transfer stack slightly while you change its z height.

Sometimes graphene samples can be difficult to see in the microscope. If you can't

see the sample you are transferring, try to center the sample as best as you can in the field of view and then tape a transparency onto the screen of the transfer computer. Use a marker to outline the shapes of things that you can see. Bring up the 20x and 50x images of your sample on a laptop. Tape the transparency onto the laptop screen and adjust the size and rotation of the 20x and 50x images so that they match the shapes drawn on the transparency. Once the image and transparency are well aligned, use a marker to outline the sample you wish to transfer onto the transparency. Tape the transparency back onto the transfer computer screen with all of the outlines well aligned to the image from the transfer microscope. The outline that you've drawn of the sample should now give you a good idea of where the sample is located.

As you lower the transfer square after coming into contact, interference fringes will start to appear. These interference fringes will eventually evolve into a solid area around your sample as you lower a bit more. At this point, you should heat the sample to 130 degrees C by pushing the silver button on the temperature controller to the right and rotating the right black knob clockwise. If the temperature controller is being flaky, push the silver button to the left once and it should fix itself. Once the sample reaches 130 degrees C, slowly raise the transfer stack until it is no longer in contact with the substrate. You can tell it is no longer in contact because the color of the sample will change from yellow to purple. Decrease the temperature by pushing the silver button to the right and rotating the right black knob counterclockwise until the set point is 0. Fully raise the transfer stack once the temperature of the substrate reaches 100 degrees C. Rotate the glass slide and PDMS toward you and remove the glass slide and PDMS from the manipulator.

You should now see the sample from the transfer stack on substrate along with some MMA residue in the transfer microscope.

C.6 Cleaning the Transferred Sample

Immerse the substrate in acetone for 4 minutes, then 4 minutes again in fresh acetone, before putting it in IPA for 1 minute. DO NOT SONICATE. Blow dry with nitrogen. Look in the optical microscope to make sure no residue remains optically. You might see the outline of your square in MMA but that is ok; there should be no visible MMA on your sample. Heat clean the sample for 3-7 hours as detailed above. Use the Veeco AFM to check for residues or bubbles from the transfer. Choose samples which have NO residue and few bubbles. For checking samples in this case, again start out with a large scan window of about 20 um. You may see bubbles at this magnification but that is ok as long as you have a bubble-free region that is about the size of the device you wish to make. Bubbles will also tend to migrate during the heat cleaning step so do not be alarmed if the bubble configuration changes during the sample process. Zoom in to about a 500 nm region that looks clean to double check that there is no residue on your sample. Again use a height scale of 5 nm and a phase scale of 20 degrees. The most important thing is that there are no residues on your sample. ABSOLUTELY DO NOT TRANSFER ONTO ANY SAMPLE THAT HAS RESIDUES! Once you transfer something on top of it, there is no way to remove the residue since it is trapped under a layer so make sure that your sample is clean before moving on. This may involve another heat cleaning step or you might have to start over. Figures C.7(a-c) show AFM images of a good transfer. Figures C.7(d-f)

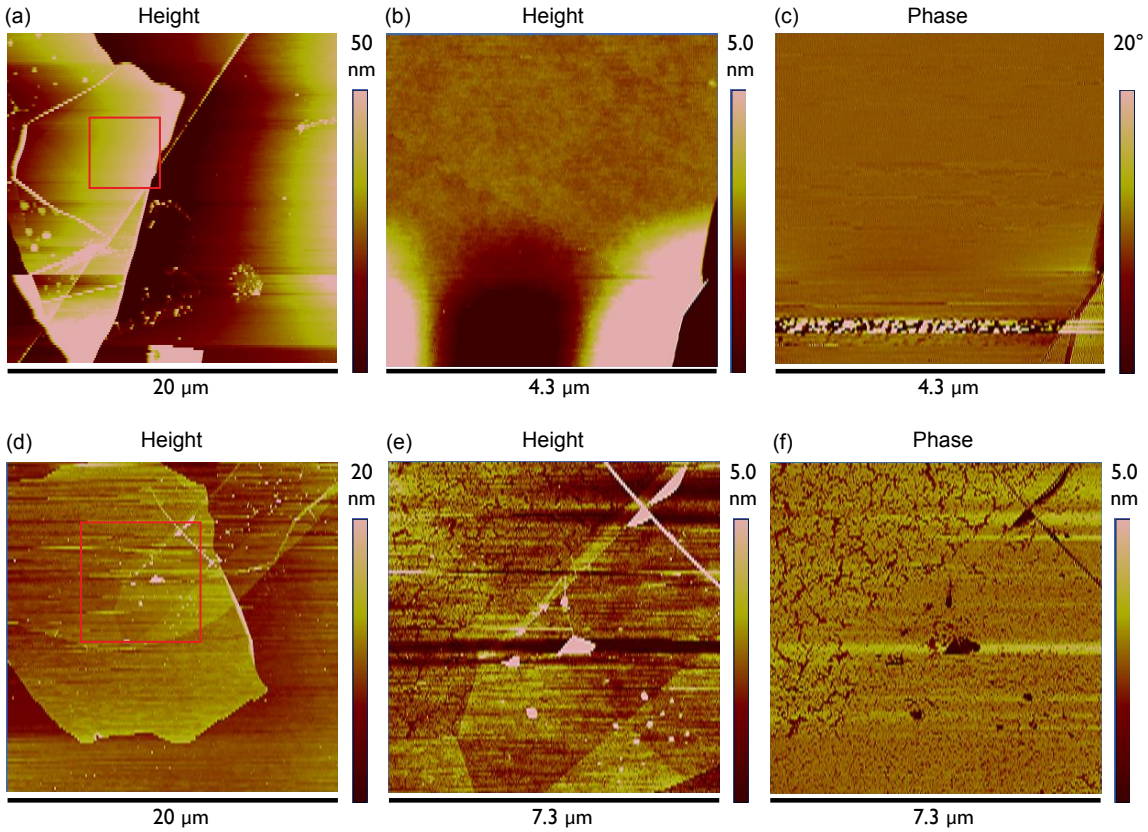

Figure C.7: AFM Images of Transfers. (a) AFM image showing the height of a clean transfer of hBN on graphite. Note that while there are bubbles in some region there is a large region with no bubbles. The height (b) and phase (c) of the red square indicated on the sample in (a) are shown. The flatness of the phase image is indicative of the cleanliness of the sample. (d) AFM image showing the height of a dirty transfer of graphene on hBN. The height (e) and phase (f) of the red square indicated on the sample in (d) are shown. Note the abundance of crack-like structures in the phase image. This indicates that there is a layer of PMMA on both the graphene and hBN.

show AFM images of a bad transfer.

Repeat this transferring process until you have achieved the device you wish to make.

C.7 Making Contacts

Make contacts to the sample using the standard e-beam recipe for graphene contacts but only deposit 1 nanometer of Chromium and 3 x the height of your sample of Au. Note that this is different from the standard graphene contact recipe since different thermal expansions of Chromium and graphene can cause rips in the graphene during heat cleaning. Heat clean one last time to remove any PMMA residue.

C.8 Etching Graphene

You can also etch the graphene into whatever shape you wish. Spin a layer of A4 at 4000 rpm and expose and develop using the standard e-beam/development recipe for graphene contacts. Etch the sample in RIE-8 for 35 seconds with a 15 sccm flow of O_2.

C.9 Tip Cleaning Samples

For graphene samples that you really like but still have some residue on them you can tip clean using an AFM. The tips we use for tip cleaning are DNP-S10 from Bruker and we use the B tip, which has a resonant frequency between 16 and 28 kHz. The tips are made of Silicon Nitride and very soft so that they don't destroy the graphene. Put the Veeco AFM into contact mode and the deflection setpoint to about 2 Volts larger than the actual deflection. Engage the tip on a flat surface near your sample; a piece of hBN or graphite nearby is usually good. If the tip does not engage, withdraw and re-engage with the deflection setpoint higher by 0.2 V.

Continue withdrawing and re-engaging with a higher setpoint until it engages. Once it is engaged, withdraw from this surface and move to your sample and engage with the same deflection setpoint.

You should use a large scan window to find where you are engaged on your sample before zooming into the location that you wish to tip clean. I like to use Scan-Triple again and monitor the Height, Deflection, and Friction. Often, the Deflection and Friction images will give you more information than the Height image. When it is first engaged you should see a sample with PMMA residue which eventually gets pushed by the AFM tip to the edges of the scan window. As you are cleaning, decrease the setpoint by 0.1V every few minutes to account for the drift in the Harvard Veeco AFM. If you wish to be very safe, you can decrease the deflection setpoint until it almost disengages; you can tell that this is about to happen because the forward and backward traces will not match well. If you do end up disengaging, quickly increase the deflection set point by 0.2V to re-engage the sample.

The largest scan window that can be cleaned efficiently is 4 um. The number of lines/scan should be 512 and the frequency should by 4 or 5 Hz. You can tile 4 um windows together if you need to clean a particularly large piece. Just be sure to keep track of which direction the tip is going in so that you don't push residue onto an area that will be measured.

I like to clean from top to bottom so I start with a scan window at the bottom of my device. The software will scan the tip downward and then back upward. Press the Frame Down icon once the tip finishes the downward scan so that it restarts the tip at the top of the scan. This will ensure that you are not pushing dirt back up onto

your sample. You may have to scan the window multiple times in order to remove all of the residue. Then move about half a scan range upward using the Offset button and press Frame Down again to clean this new region of your sample by scanning the tip and pressing Frame Down whenever it reaches the bottom of the scan. Once this region is clean, offset the scan range downward by half a scan so that you are now pushing the residue you just cleaned from the new region off of your sample. After the new residue has been pushed off, move by a full scan range upward to clean more of your device. Repeat cleaning and moving downward to get the residue off of your sample. Continue moving upward, cleaning, and moving downward until you have cleaned your entire device.

Various stages of tip cleaning are shown in Fig. C.8.

Good luck!

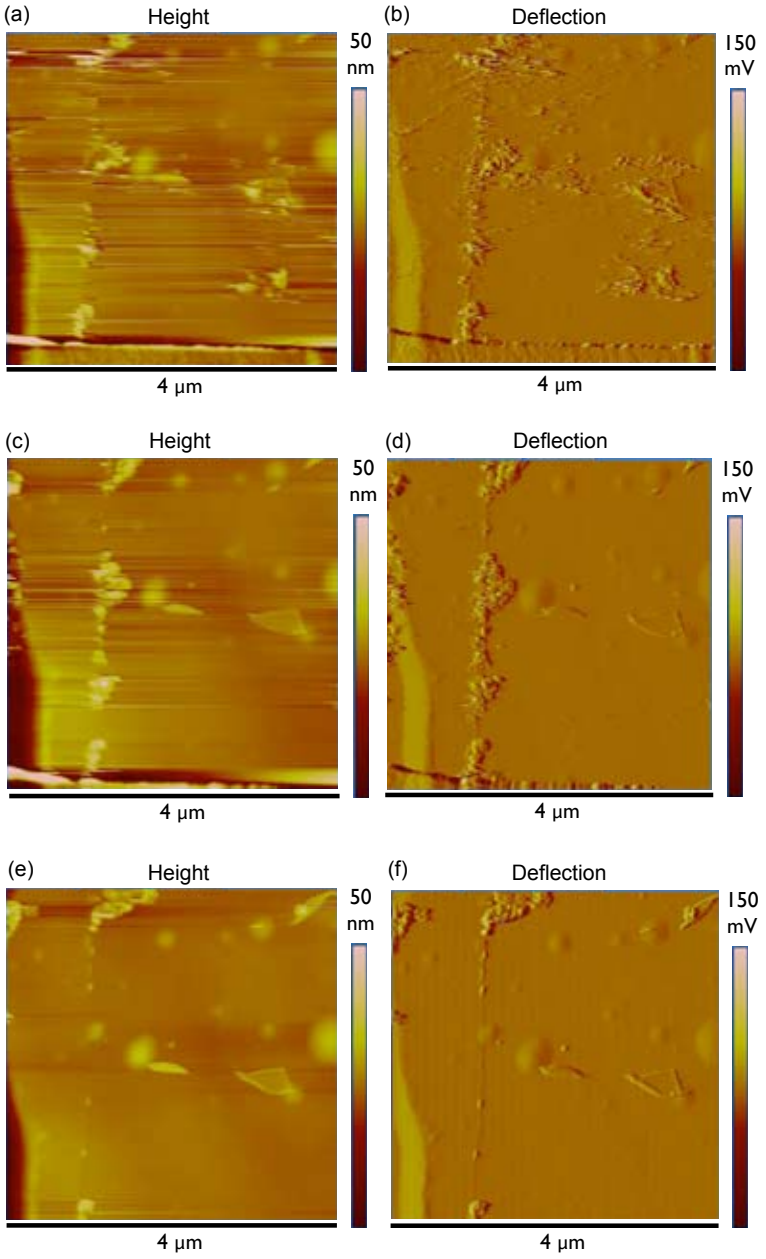

Figure C.8: Contact AFM Images of Devices. (a) AFM image showing the height and deflection (b) of a sample with PMMA residue on the surface. (c) AFM image showing the height and deflection (d) of the same sample after tip cleaning for 5 scans. (e) AFM image showing the height and deflection (f) of the same sample after tip cleaning for 15 scans.

Bibliography

[1] R. B. Laughlin, *Anomalous Quantum Hall Effect: An Incompressible Quantum Fluid with Fractionally Charged Excitations*, Phys. Rev. Lett. **50,** 1395 (1983).

[2] S. M. Girvin, *The Quantum Hall Effect: Novel Excitations and Broken Symmetries*, in *Topological aspects of low dimensional systems,* edited by A. Comtet, T. Jolicoeur, S. Ouvry, and F. David (Springer-Verlag, Berlin, 1999).

[3] J. H. Davies, *The Physics of Low-Dimensional Semiconductors,* (Cambridge University Press, Cambridge, 2006).

[4] L. N. Pfeiffer, Private communication.

[5] M. Shayegan, *Electrons in a Flatland*, in *Topological aspects of low dimensional systems,* edited by A. Comtet, T. Jolicoeur, S. Ouvry, and F. David (Springer-Verlag, Berlin, 1999).

[6] F. C. Zhang and S. Das Sarma, *Excitation gap in the fractional quantum Hall effect: Finite layer thickness corrections*, Phys. Rev. B **33**, 2903 (1986).

[7] A. K. Geim and K. S. Novosolev, *The rise of graphene*, Nature Materials **6,** 183 (2007).

[8] A. H. Castro Neto, F. Guinea, N. M. R. Peres, K. S. Novosolev, and A. K. Geim, *The electronic properties of graphene*, Rev. Mod. Phys. **81,** 109 (2009).

[9] A. J. Leggett, *Lecture 5: Graphene: Electronic band structure and Dirac fermions*, Selected Topics in Condensed Matter, Institute for Quantum Computing (2010).

[10] K. S. Novosolev, Z. Jiang, Y. Zhang, S. V. Morozov, H. L. Stormer, U. Zeitler, J. C. Maan, G. S. Boebinger, P. Kim, and A. K. Geim, *Room-Temperature Quantum Hall Effect in Graphene*, Science **315,** 1379 (2007).

[11] B. I. Halperin, *Quantized Hall conductance, current-carrying edge states, and the existence of extended states in a two-dimensional disordered potential*, Phys. Rev. B **25,** 2185 (1982).

[12] A. J. Leggett, *Lecture 7: The Integral Quantum Hall Effect*, Selected Topics in Condensed Matter, Institute for Quantum Computing (2010).

[13] H. L. Stormer,D. C. Tsui, and A. C. Gossard, *The fractional quantum Hall effect*, Rev. Mod. Phys. **71,** S298 (1999).

[14] R. B. Laughlin, *Quantized Hall conductivity in two dimensions*, Phys. Rev. B **23,** 5362 (1981).

[15] R. B. Laughlin, *Elementary Theory: The Incompressible Quantum Fluid*, in *The Quantum Hall Effect,* edited by R. E. Prange, and S. M. Girvin (Springer-Verlag, Berlin, 1990).

[16] J. M. Leinaas and J. Myrrheim, *On the theory of identical particles*, Il Nuovo Cimento **37B**, 1 (1977).

[17] D. P. Arovas, *Topics in Fractional Statistics*, in *Geometric Phases in Physics,* edited by A. Shapere and F. Wilczek (World Scientific, Singapore, 1989).

[18] C. Nayak, S. H. Simon, A. Stern, M. Freedman, and S. Das Sarma, *Non-Abelian anyone and topological quantum computation*, Rev. Mod. Phys. **80,** 1083 (2008).

[19] J. K. Jain, *Composite Fermions* (Cambridge University Press, Cambridge, 2007).

[20] W. Kang, H. L. Stormer,L. N. Pfeiffer, K. W. Baldwin, and K. W. West, *How real are composite fermions?*, Phys. Rev. Lett. **71,** 3850 (1993).

[21] V. J. Goldman, B. Su, and J. K. Jain, *Detection of composite fermions by magnetic focusing*, Phys. Rev. Lett. **72,** 2065 (1994).

[22] I. Kukushkin, K. von Klitzing, and K. Eberl, *Spin Polarization of Composite Fermions: Measurements of the Fermi Energy*, Phys. Rev. Lett. **82,** 3665 (1999).

[23] N. Freytag, M. Horvatic, C. Berthier, M. Shayegan, and L. P. Levy, *NMR Investigation of How Free Composite Fermions are at* $\nu = 1/2$, Phys. Rev. Lett. **89,** 246804 (2002).

[24] J. P. Eisenstein, H. L. Stormer, and L. N. Pfeiffer, *Evidence for a spin transition in the* $\nu = 2/3$ *fractional quantum Hall effect*, Phys. Rev. B **41,** 7910 (1990).

[25] W. Kang, J. B. Young, S. T. Hannahs, E. Palm, K. L. Campman, and A. C. Gossard, *Evidence for a spin transition in the* $\nu = 2/5$ *fractional quantum Hall Effect*, Phys. Rev. B **56,** R12776 (1997).

[26] N. R. Cooper and V. Tripathi, *Theory of NMR in semiconductor quantum point contact devices*, Phys. Rev. B **77**, 245324 (2008).

[27] R. Tycko, S. E. Barrett, G. Dabbagh, L. N. Pfeiffer, and K. W. West, *Electronic states in gallium arsenide quantum wells probed by optically pumped NMR*, Science **268**, 1460 (1995).

[28] K. R. Wald, L. P. Kouwenhoven, P. L. McEuen, N. C. van der Vaart, and C. T. Foxon, *Local Dynamic Nuclear Polarization Using Quantum Point Contacts*, Phys. Rev. Lett. **73,** 1011 (1994).

[29] D. C. Dixon, K. R. Wald, P. L. McEuen, and M. R. Melloch, *Dynamic nuclear polarization at the edge of a two-dimensional electron gas*, Phys. Rev. B **56,** 4743 (1997).

[30] Y. Q. Li and J. H. Smet, *NuclearElectron Spin Interactions in the Quantum Hall Regime*, in *Spin Physics in Semiconductors,* edited by M. I. Dyakonov (Springer-Verlag, Berlin, 2008).

[31] S. Kronmüller, W. Dietsche, K. v. Klitzing, G. Denninger, W. Wegscheider, and M. Bichler, *New Type of Electron Nuclear-Spin Interaction from Resistively Detected NMR in the Fractional Quantum Hall Effect Regime*, Phys. Rev. Lett. **82,** 4070 (1999).

[32] J. H. Smet, R. A. Deutschmann, W. Wegscheider, G. Abstreiter, and K. v. Klitzing, *Ising Ferromagnetism and Domain Morphology in the Fractional Quantum Hall Regime*, Phys. Rev. Lett. **86,** 2412 (2001).

[33] J. H. Smet, R. A. Deutschmann, F. Ertl, W. Wegscheider, G. Abstreiter, and K. v Klitzing, *Gate-voltage control of spin interactions between electrons and nuclei in a semiconductor*, Nature **415,** 281 (2002).

[34] T. Machida, S. Ishizuka, T. Yamazaki, S. Komiyama, K. Muraki, and Y. Hirayama, *Spin polarization of fractional quantum Hall edge channels studied by dynamic nuclear polarization*, Phys. Rev. B **65,** 233304 (2002).

[35] T. Machida and S. Komiyama, *Hysteretic Feature of Quantum-Hall-Effect Breakdown Caused by Dynamic Nuclear Polarization*, J. Phys. Soc. Jpn. **72,** 199 (2003).

[36] O. Stern, N. Freytag, A. Fay, W. Dietsche, J. H. Smet, K. v. Klitzing, D. Schuh, and W. Wegscheider, *NMR study of the electron spin polarization in the fractional quantum Hall effect of a single quantum well: Spectroscopic evidence for domain formation*, Phys. Rev. B **70,** 075318 (2004).

[37] G. Yusa,K. Muraki, K. Takashina, K. Hashimoto, and Y. Hirayama, *Controlled multiple quantum coherences of nuclear spins in a nanometre-scale device*, Nature **434,** 1001 (2005).

[38] M. Kawamura, H. Takahashi, S. Masabuchi, Y. Hashimoto, S. Katsumoto, K. Hamaya, and T. Machida, *Dynamic nuclear polarization and Knight shift measurements in a breakdown regime of integer quantum Hall effect*, Appl. Phys. Lett. **90,** 022102 (2007).

[39] L. A. Tracy, J. P. Eisenstein, L. N. Pfeiffer, and K. W. West, *Spin Transition in the Half-Filled Landau Level*, Phys. Rev. Lett. **98,** 086801 (2007).

[40] M. Kawamura, H. Takahashi, S. Masabuchi, Y. Hashimoto, S. Katsumoto, K. Hamaya, and T. Machida, *Dynamic nuclear polarization and Knight shift measurements in a breakdown regime of integer quantum Hall effect*, Physica E **40,** 1389 (2008).

[41] Y. Q. Li, V. Umansky, K. v. Klitzing, and J. H. Smet, *Nature of the Spin Transition in the Half-Filled Landau Level*, Phys. Rev. Lett. **102,** 046803 (2009).

[42] M. Kawamura, M. Ono, Y. Hashimoto, S. Katsumoto, K. Hamaya, and T. Machida, *Dynamic nuclear polarization induced by breakdown of fractional quantum Hall effect*, Phys. Rev. B **79,** 193304 (2009).

[43] C. R. Dean, bibinfoauthorB. A. Piot, G. Gervais, L. N. Pfeiffer, and K. W. West, *Current-induced nuclear-spin activation in a two-dimensional electron gas*, Phys. Rev. B **80,** 153301 (2009).

[44] Y. Ren, W. Yu, S. M. Frolov, J. A. Folk, and W. Wegscheider, *Nuclear polarization in quantum point contacts in an in-plane magnetic field*, Phys. Rev. B **81,** 125330 (2010).

[45] P. Khandelwal, A. E. Dementyev, N. N. Kuzma, S. E. Barrett, L. N. Pfeiffer, and K. W. West, *Spectroscopic Evidence for the Localization of Skyrmions near* $\nu = 1$ *as* $T \to 0$, Phys. Rev. Lett. **86,** 5353 (2001).

[46] R. Côté, A. H. MacDonald, L. Brey, H. A. Fertig, S. M. Girvin, and H. T. C Stoof, *Collective Excitations, NMR, and Phase Transitions in Skyrme Crystals*, Phys. Rev. Lett. **78,** 4825 (1997).

[47] K. Hashimoto, K. Muraki, T. Saku, and Y. Hirayama, *Electrically Controlled Nuclear Spin Polarization and Relaxation by Quantum-Hall States*, Phys. Rev. Lett. **88,** 176601 (2002).

[48] X. G. Wen, *Electrodynamical properties of gapless edge excitations in the fractional quantum Hall states*, Phys. Rev. Lett. **64,** 2206 (1990).

[49] M. D. Johnson and A. H. MacDonald, *Composite edges in the* $\nu = 2/3$ *fractional quantum Hall effect*, Phys. Rev. Lett. **67,** 2060 (1991).

[50] C. L. Kane and M. P. A. Fisher, *Impurity scattering and transport of fractional quantum Hall edge states*, Phys. Rev. B **51,** 13449 (1994).

[51] C. L. Kane, M. P. A. Fisher, and J. Polchinski, *Randomness at the edge: Theory of quantum Hall transport at filling* $\nu = 2/3$, Phys. Rev. Lett. **72,** 4129 (1994).

[52] J. E. Moore and F. D. M. Haldane, *Edge excitations of the* $\nu = 2/3$ *spin-singlet quantum Hall state*, Phys. Rev. B **55,** 7818 (1997).

[53] R. C. Ashoori, H. L. Stormer, L. N. Pfeiffer, K. W. Baldwin, and K. West, *Edge magnetoplasmons in the time domain*, Phys. Rev. B **45,** 3894 (1992).

[54] A. Bid, N. Ofek, M. Heiblum, V. Umansky, and D. Mahalu, *Shot Noise and Charge at the 2/3 Composite Fractional Quantum Hall State*, Phys. Rev. Lett. **103,** 236802 (2009).

[55] A. Bid, N. Ofek, H. Inoue, M. Heiblum, C. L. Kane, V. Umansky, and D. Mahalu, *Observation of neutral modes in the fractional quantum Hall regime*, Nature **466,** 585 (2010).

[56] D. Ferraro,A. Braggio, N. Magnoli, and M. Sassetti, *Charge tunneling in fractional edge channels*, Phys. Rev. B **82,** 085323 (2010).

[57] S. W. Hwang, J. A. Simmons, D. C. Tsui, and M. Shayegan, *Quantum interference in two independently tunable parallel point contacts*, Phys. Rev. B **44,** 13497 (1991).

[58] P. J. Simpson, D. R. Mace, C. J. B. Ford, I. Zailer, M. Pepper, D. A. Ritchie, J. E. F. Frost, M. P. Grimshaw, and G. A. C. Jones, *Aharonov-Bohm effect and one-dimensional ballistic transport through two independent parallel channels*, Appl. Phys. Lett. **63,** 3191 (1993).

[59] C. J. B. Ford, P. J. Simpson, I. Zailer, D. R. Mace, M. Yosefin, M. Pepper, D. A. Ritchie, J. E. F. Frost, M. P. Grimshaw, and G. A. C. Jones, *Charging and double-frequency Aharonov-Bohm effects in an open system*, Phys. Rev. B **49,** 17456 (1994).

[60] V. J. Goldman and B. Su, *Resonant Tunneling in the Quantum Hall Regime: Measurement of Fractional Charge*, Science **267,** 1010 (1995).

[61] J. D. F. Franklin, I. Zailer, C. J. B. Ford, P. J. Simpson, J. E. F. Frost, D. A. Ritchie, M. Y. Simmons, and M. Pepper, *The Aharonov-Bohm effect in the fractional quantum Hall regime*, Surf. Sci. **361/362,** 17 (1996).

[62] I. J. Maasilta and V. J. Goldman, *Line shape of resonant tunneling between fractional quantum Hall edges*, Phys. Rev. B **55,** 4081 (1997).

[63] M. Kataoka, C. J. B. Ford, G. Faini, D. Mailly, M. Y. Simmons, D. R. Mace, C.-T. Liang, and D. A. Ritchie, *Detection of Coulomb Charging around an Antidot in the Quantum Hall Regime*, Phys. Rev. Lett. **83,** 160 (1999).

[64] V. J. Goldman, I. Karakurt, J. Liu, and A. Zaslavsky, *Invariance of charge of Laughlin quasiparticles*, Phys. Rev. B **64,** 085319 (2001).

[65] M. Kataoka, C. J. B. Ford, M. Y. Simmons, and D. A. Ritchie, *Kondo Effect in a Quantum Antidot*, Phys. Rev. Lett. **89,** 226803 (2002).

[66] A. A. Bykov, D. V. Nomokonov, A. K. Bakarov, O. Estibals, and J. C. Portal, *Coulomb Oscillations of Conductance in an Open Ring Interferometer in a Strong Magnetic Field*, JETP Lett. **78,** 642 (2003).

[67] H.-S. Sim, M. Kataoka, C. J. B. Ford, *Electron interactions in an antidote in the integer quantum Hall regime*, Phys. Rep. **456,** 127 (2008).

[68] V. J. Goldman, J. Liu, and A. Zaslavsky, *Electron tunneling spectroscopy of a quantum antidot in the integer quantum Hall regime*, Phys. Rev. B **77,** 115328 (2008).

[69] H. S. Sim, M. Kataoka, H. Yi, N. Y. Hwang, M.-S. Choi, and S.-R. E. Yang, *Coulomb Blockade and Kondo Effect in a Quantum Hall Antidot*, Phys. Rev. Lett. **91,** 266801 (2003).

[70] S. Ihnatsenka, I. V. Zozoulenko, and G. Kirczenow, *Electron-electron interactions in antidot-based Aharonov-Bohm interferometers*, Phys. Rev. B **80,** 115303 (2009).

[71] Y. Zhang, D. T. McClure, E. M. Levenson-Falk, C. M. Marcus, L. N. Pfeiffer, and K. W. West, *Distinct signatures for Coulomb blockade and Aharonov-Bohm interference in electronic Fabry-Perot interferometers*, Phys. Rev. B **79,** 241304(R) (2009).

[72] B. I. Halperin, A. Stern, I. Neder, and B. Rosenow, *Theory of the Fabry-Perot Quantum Hall Interferometer*, Phys. Rev. B **83,** 155440 (2011).

[73] J. K. Jain and S. A. Kivelson, *Quantum Hall effect in quasi one-dimensional systems: Resistance fluctuations and breakdown*, Phys. Rev. Lett. **60,** 1542 (1988).

[74] S. A. Kivelson and V. L. Pokrovsky, *Methods to measure the charge of the quasiparticles in the fractional quantum Hall effect*, Phys. Rev. B **40,** 1373 (1989).

[75] M. R. Geller, D. Loss, and G. Kirczenow, *Mesoscopic Effects in the Fractional Quantum Hall Regime: Chiral Luttinger Liquid versus Fermi Liquid*, Phys. Rev. Lett. **77,** 5110 (1996).

[76] S. Das Sarma, M. Freedman, and C. Nayak, *Topologically Protected Qubits from a Possible Non-Abelian Fractional Quantum Hall State*, Phys. Rev. Lett. **94,** 166802 (2005).

[77] D. V. Averin and J. A. Nesteroff, *Coulomb Blockade of Anyons in Quantum Antidots*, Phys. Rev. Lett. **99,** 096801 (2007).

[78] R. Ilan, B. Rosenow, and A. Stern, *Signatures of Non-Abelian Statistics in Non-linear Coulomb Blockade Transport*, Phys. Rev. Lett. **106,** 136801 (2011).

[79] A. Kou *et al.*, unpublished.

[80] N. Ofek, A. Bid, M. Heiblum, A. Stern, V. Umansky, and D. Mahalu, *Role of interactions in an electronic Fabry-Perot interferometer operating in the quantum Hall effect regime*, Proc. Natl. Acad. Sci. USA **107,** 5276 (2010).

[81] P. A. Lee, *Comment on "Resistance fluctuations in narrow AlGaAs/GaAs heterostructures: Direct evidence of fractional charge in the fractional quantum Hall effect"*, Phys. Rev. Lett. **65,** 2206 (1990).

[82] W. R. Lee and H. S. Sim, *Capacitive interaction model for Aharonov-Bohm effects of a quantum Hall antidot*, Phys. Rev. B **83,** 035308 (2011).

[83] J. Martin, S. Ilani, B. Verdene, J. Smet, V. Umansky, D. Mahalu, D. Schuh, G. Abstreiter, and A. Yacoby, *Localization of Fractionally Charged Quasi-Particles*, Science **305,** 980 (2004).

[84] S. Levy-Schreier, Thesis, Weizmann Institute of Science (2013).

[85] L. Saminadayar, D. C. Glattli, Y. Jin, and B. Etienne, *Observation of the e/3 Fractionally Charged Laughlin Quasiparticle*, Phys. Rev. Lett. **79,** 2526 (1997).

[86] R. de-Picciotto, M. Reznikov, M. Heiblum, V. Umansky, G. Bunin, and D. Mahalu, *Direct observation of fractional charge*, Nature **389,** 162 (1997).

[87] M. Kataoka, C. J. B. Ford, M. Y. Simmons, and D. A. Ritchie, *Selective spin-resolved edge-current injection into a quantum antidot*, Phys. Rev. B **68,** 153305 (2003).

[88] D. T. McClure, Y. Zhang, B. Rosenow, E. M. Levenson-Falk, C. M. Marcus, L. N. Pfeiffer, and K. W. West, *Edge-State Velocity and Coherence in a Quantum Hall Fabry-Perot Inteferometer*, Phys. Rev. Lett. **103,** 206806 (2009).

[89] C. de C. Chamon, D. E. Freed, S. A. Kivelson, S. L. Sondhi, and X. G. Wangt, *Two point-contact interferometer for quantum Hall systems*, Phys. Rev. B **55,** 2331 (1997).

[90] N. Shibata and K. Nomura, *Fractional Quantum Hall Effects in Graphene and Its Bilayer*, J. Phys. Soc. Jpn. **78,** 104708 (2009).

[91] V. M. Apalkov and T. Chakraborty, *Controllable Driven Phase Transitions in Fractional Quantum Hall Effect in Bilayer Graphene*, Phys. Rev. Lett. **105,** 036801 (2010).

[92] Z. Papić, R. Thomale, and D. A. Abanin, *Tunable Electron Interactions and Fractional Quantum Hall States in Graphene*, Phys. Rev. Lett. **107,** 176602 (2011).

[93] Z. Papić, D. A. Abanin, Y. Barlas, and R. N. Bhatt, *Tunable interactions and phase transitions in Dirac materials in a magnetic field*, Phys. Rev. B **84,** 241306(R) (2011).

[94] V. M. Apalkov and T. Chakraborty, *Stable Pfaffian State in Bilayer Graphene*, Phys. Rev. Lett. **107,** 186803 (2011).

[95] K. Snizhko, V. Cheianov, and S. H. Simon, *Importance of interband transitions for the fractional quantum Hall effect in bilayer graphene*, Phys. Rev. B **85,** 201415(R) (2012).

[96] Z. Papić and D. A. Abanin, *Topological Phases in the Zeroth Landau Level of Bilayer Graphene*, arxiv:1307.2909 (2013).

[97] E. McCann and V. I Fal'ko, *Landau-Level Degeneracy and Quantum Hall Effect in a Graphite Bilayer*, Phys. Rev. Lett. **96,** 086805 (2006).

[98] K. S. Novosolev, E. McCann, S. V. Morozov, V. I. Fal'ko, M. I. Katsnelson, A. K. Geim, F. Schedin, and D. Jiang, *Unconventional quantum Hall effect and Berry's phase of 2π in bilayer graphene*, Nat. Phys. **2,** 177 (2006).

[99] B. E. Feldman, J. Martin, and A. Yacoby, *Broken-symmetry states and divergent resistance in suspended bilayer graphene*, Nat. Phys. **5,** 889 (2009).

[100] Y. Zhao, P. Cadden-Zimansky, Z. Jiang, and P. Kim, *Symmetry Breaking in the Zero-Energy Landau Level in Bilayer Graphene*, Phys. Rev. Lett. **104,** 066801 (2010).

[101] Y. Barlas, R. Coté, K. Nomura, and A. H. MacDonald, *Intra-Landau-Level Cyclotron Resonance in Bilayer Graphene*, Phys. Rev. Lett. **101,** 097601 (2008).

[102] R. T. Weitz, M. T. Allen, B. E. Feldman, J. Martin, and A. Yacoby, *Broken-Symmetry States in Double Gated Suspended Bilayer Graphene*, Science **330,** 812 (2010).

[103] S. Kim, K. Lee, and E. Tutuc, *Spin-Polarized to Valley-Polarized Transition in Graphene Bilayers at $\nu = 0$ in High Magnetic Fields*, Phys. Rev. Lett. **107,** 016803 (2011).

[104] J. Velasco, Jr., L. Jing, W. Bao, Y. Lee, P. Kratz, V. Aji, M. Bockrath, C. N. Lau, C. Varma, R. Stillwell, D. Smirnov, F. Zhang, J. Jung, and A. H. MacDonald, *Transport spectroscopy of symmetry-broken insulating states in bilayer graphene*, Nat. Nano. **7,** 156 (2012).

[105] P. Maher, C. R. Dean, A. F. Young, T. Taniguchi, K. Watanabe, K. L. Shepard, J. Hone, and P. Kim, *Evidence for a spin phase transition at charge neutrality in bilayer graphene*, Nat. Phys. **9,** 154 (2013).

[106] M. A. Kharitonov, *Canted antiferromagnetic phase of the $\nu = 0$ quantum Hall state in bilayer graphene*, Phys. Rev. Lett. **109,** 046803 (2012).

[107] X. Du, I. Skachko, F. Luican, and E. Y. Andrei, *Fractional quantum Hall effect and insulating phase of Dirac electrons in graphene*, Nature **462,** 192195 (2009).

[108] K. I. Bolotin, F. Ghahari, M. D. Shulman, H. L. Stormer, and P. Kim, *Measurements of the $\nu = 1/3$ fractional quantum Hall Energy Gap in Suspended Graphene*, Phys. Rev. Lett. **106,** 046801 (2011).

[109] C. R. Dean, A. F. Young, P. Cadden-Zimansky, L. Wang, K. Watanabe, T. Taniguchi, P. Kim, J. Hone, and K. L. Shepard, *Multicomponent fractional quantum Hall effect in graphene*, Nat. Phys. **7,** 693 (2011).

[110] D. S. Lee, V. Skakalova, R. T. Weitz, K. von Klitzing, and J. H. Smet, *Transconductance Fluctuations as a Probe for Interaction Inducted Quantum Hall States in Bilayer Graphene*, Phys. Rev. Lett. **109,** 056602 (2012).

[111] B. E. Feldman, B. Krauss, J. H. Smet, and A. Yacoby, *Unconventional Sequence of Fractional Quantum Hall States in Suspended Graphene*, Science **337,** 1196 (2012).

[112] B. E. Feldman,A. J. Levin, B. Krauss, D. A. Abanin, B. I. Halperin, J. H. Smet, and A. Yacoby, *Fractional Quantum Hall Phase Transitions and Four-flux Composite Fermions in Graphene*, arxiv:1303.0838 (2013).

[113] W. Bao, Z. Zhao, H. Zhang, G. Liu, P. Kratz, L. Jing, J. Velasco, Jr., D. Smirnov, and C. N. Lau, *Magnetoconductance oscillations and evidence for fractional quantum Hall states in suspended bilayer and trilayer graphene*, Phys. Rev. Lett. **105,** 246601 (2010).

[114] D-K. Ki,V. I. Fal'ko, and A. F. Morpurgo, *Even-Denominator fractional quantum Hall state in multi-terminal suspended bilayer graphene devices*, arxiv:1305.4761 (2013).

[115] M. J. Yoo, T. A. Fulton, H. F. Hess, R. L. Willett, L. N. Dunkleberger, R. J. Chichester, L. N. Pfeiffer, and K. W. West, *Scanning Single-Electron Transistor Microscopy: Imaging Individual Charges*, Science **276,** 579 (1997).

[116] A. Yacoby, H. F. Hess, T. A. Fulton, L. N. Pfeiffer, and K. W. West, *Electrical imaging of the quantum Hall states*, Solid State Comm. **111,** 1 (1999).

[117] J. Martin, B. E. Feldman, R. T. Weitz, M. T. Allen, and A. Yacoby, *Local compressibility measurements of correlated states in bilayer graphene*, Phys. Rev. Lett. **105,** 256806 (2010).

[118] S. Ilani, E. Teitelbaum, J. H. Smet, D. Mahalu, V. Umansky, and A. Yacoby, *The microscopic nature of localization in the quantum Hall effect*, Nature **427** 328 (204).

[119] J. P. Eisenstein, L. N. Pfeiffer, and K. W. West, *Negative compressibility of the interacting 2-dimensional electron and quasi-particle gases*, Phys. Rev. Lett. **68,** 674 (1992).

[120] M. R. Peterson and C. Nayak, *More realistic Hamiltonians for the fractional quantum Hall regime in GaAs and graphene*, Phys. Rev. B **87,** 245129 (2013).

[121] R Nandkishore and L. Levitov, *Dynamical Screening and Excitonic Instability in Bilayer Graphene*, Phys. Rev. Lett. **104,** 156803 (2010).

[122] E. McCann, *Asymmetry gap in the electronic band structure of bilayer graphene*, Phys. Rev. B **74,** 161403(R) (2006).

[123] B. Hunt, J. D. Sanchez-Yamagishi, A. F. Young, M. Yankowitz, B. J. LeRoy, K. Watanabe, T. Taniguchi, P. Moon, M. Koshino, P. Jarillo-Herrero, and R. C. Ashoori, *Massive Dirac fermions and Hofstadter butterfly in a van der Waals heterostructure*, Science **340,** 1427 (2013).

[124] C. Töke and V. I. Fal'ko, *Intra-Landau-level magnetoexcitons and the transition between quantum Hall states in bilayer graphene*, Phys. Rev. B **83,** 115455 (2011).

[125] R. J. Schoelkopf, P. Wahlgren, A. A. Kozhevnikov, P. Delsing, and D. E. Prober, *The Radio-Frequency Single-Electron Transistor (RF-SET): A Fast and Ultrasensitive Electrometer*, Science **280,** 1238 (1998).

[126] M. Pioro-Ladriere, J. H. Davies, A. R. Long, A. S. Sachrajda, L. Gaudreau, P. Zawadzki, J. Lapointe, J. Gupta, Z. Wasilewski, and S. Studenikin, *The origin of switching noise in GaAs/AlGaAs lateral gated devices*, Phys. Rev. B **72,** 115331 (2005).

[127] C. Buizert, F. H. L. Koppens, M. Pioro-Ladriere, H.-P. Tranitz, I. T. Vink, S. Tarucha, W. Wegscheider, and L. M. K. Vandersypen, *InSitu Reduction of Charge Noise in GaAs/AlGaAs Schottky-Gated Devices*, Phys. Rev. Lett. **101,** 226603 (2008).

[128] K Hitachi, T. Ota, and K. Muraki, *Intrinsic and extrinsic origins of low-frequency noise in GaAs/AlGaAs Schottky-gated nanostructures*, Appl. Phys. Lett. **102,** 192104 (2013).

[129] O. E. Dial, M. D. Shulman, S. P. Harvey, H. Bluhm, V. Umansky, and A. Yacoby, *Charge Noise Spectroscopy Using Coherent Exchange Oscillations in a Singlet-Triplet Qubit*, Phys. Rev. Lett. **110,** 146804 (2013).

[130] M. Wassermeier, J. Oshinowo, J. P. Kotthaus, A. H. MacDonald, C. T. Foxon, and J. J. Harris, *Edge magnetoplasmons in the fractional-quantum-Hall-effect regime*, Phys. Rev. B **41,** 10287 (1990).

[131] N. B. Zhitenev, R. J. Haug, K. v. Klitzing, and K. Eberl, *Time-resolved measurements of transport in edge channels*, Phys. Rev. Lett. **71,** 2292 (1993).

[132] G. Ernst, N. B. Zhitenev, R. J. Haugl, and K. v. Klitzing, *Dynamic Excitations of Fractional Quantum Edge Channels*, Phys. Rev. Lett. **79,** 3748 (1997).

[133] Y. Chen, R. M. Lewis, L. W. Engel, D. C. Tsui, P. D. Ye, L. N. Pfeiffer, and K. W. West, *Microwave Resonance of the 2D Wigner Crystal around Integer Landau Fillings*, Phys. Rev. Lett. **91,** 016801 (2003).

[134] H. Zhu, Y. Zhu, P. Jiang, L. W. Engel, D. C. Tsui, L. N. Pfeiffer, and K. W. West, *Observation of a Pinning Mode in a Wigner Solid with $\nu = 1/3$ Fractional Quantum Hall Excitations*, Phys. Rev. Lett. **105,** 126803 (2010).

[135] C. Barthel, *Control and fast Measurement of Spin Qubits*, Thesis, Harvard University (2010).

[136] F. Pobell, *Matter and Methods at Low Temperature* (Springer-Verlag, Berlin, 2007).

[137] J. B. Miller, I. P. Radu, D. M. Zumbuhl, E. M. Levenson-Falk, M. A. Kastner, C. M Marcus, L. N. Pfeiffer, and K. W. West, *Fractional quantum Hall effect in a quantum point contact at filling fraction 5/2*, Nature Physics **3,** 561 (2007).

[138] H. O. H. Churchill, *Quantum Dots in Gated Nanowires and Nanotubes*, Thesis, Harvard University (2012).

[139] D. F. Santavicca and D. E. Prober, *Impedance-matched low-pass stripline filters*, Meas. Sci. Technol. **19,** 087001 (2008).